

Universidade de São Paulo
Instituto de Física

Magnetismo geometricamente frustrado no pirocloro
 $\text{Er}_2\text{Ti}_{2-x}\text{Sn}_x\text{O}_7$ e nas fluoritas desordenadas $R_2\text{Zr}_2\text{O}_7$
($R = \text{Dy, Ho, Tb}$)

Jonathan Gustavo Acosta Ramón

Orientador: Prof. Dr. Rafael Sá de Freitas

Tese de doutorado apresentada ao Instituto de Física da
Universidade de São Paulo, como requisito parcial para
a obtenção do título de Doutor em Ciências.

Banca Examinadora:

Prof. Dr. Rafael Sá de Freitas - Orientador (IF-USP)

Prof. Dr. Stephen Rowley (University of Cambridge)

Prof. Dr. Ludovic Jaubert (University of Bordeaux)

Prof. Dr. Eric de Castro e Andrade (IFSC-USP)

Prof. Dr. Fernando Assis García (IF-USP)



São Paulo

2020

FICHA CATALOGRÁFICA
Preparada pelo Serviço de Biblioteca e Informação
do Instituto de Física da Universidade de São Paulo

Acosta Ramón, Jonathan Gustavo

Magnetismo geometricamente frustrado no pirocloro $\text{Er}_2\text{Ti}_{2-x}\text{Sn}_x\text{O}_7$ e nas fluoritas desordenadas $\text{R}_2\text{Zr}_2\text{O}_7$ (R = Dy, Ho, Tb). São Paulo, 2020.

Tese (Doutorado) – Universidade de São Paulo. Instituto de Física, Depto. de Física dos Materiais e Mecânica.

Orientador: Prof. Dr. Rafael Sá de Freitas

Área de Concentração: Fenômenos Magnéticos

Unitermos: 1. Fenômenos magnéticos; 2. Frustração geométrica; 3. Pirocloro; 4. Desordem.

USP/IF/SBI-079/2020

University of São Paulo
Physics Institute

Geometrically frustrated magnetism in the pyrochlore
 $\text{Er}_2\text{Ti}_{2-x}\text{Sn}_x\text{O}_7$ and in the disordered fluorites
 $R_2\text{Zr}_2\text{O}_7$ ($R = \text{Dy}, \text{Ho}, \text{Tb}$)

Jonathan Gustavo Acosta Ramón

Supervisor: Prof. Dr. Rafael Sá de Freitas

Thesis submitted to the Physics Institute of the University of São Paulo in partial fulfillment of the requirements for the degree of Doctor of Science.

Examining Committee:

Prof. Dr. Rafael Sá de Freitas - Supervisor (IF-USP)

Prof. Dr. Stephen Rowley (University of Cambridge)

Prof. Dr. Ludovic Jaubert (University of Bordeaux)

Prof. Dr. Eric de Castro e Andrade (IFSC-USP)

Prof. Dr. Fernando Assis García (IF-USP)

São Paulo

2020

Para mis abuelos

Acknowledgements

First, I would like to thank my supervisor, Rafael Sá de Freitas, for his guidance into the area of frustrated magnetism and for his support throughout my studies. I am also grateful to Jason Gardner and Chin–Wei Wang for performing neutron experiments at ANSTO and analysing the data, and also for help me answer my questions about neutron scattering. I would like to thank Prof. José Antonio Souza and postdoctoral researcher Vinicius Gomes for allow and help me to perform experiments at the facilities of the UFABC. I want to thank Prof. Flavio Vicci and Marina Leite from the IQUSP, and Prof. Jorge Lago from País Vasco University for preparing some of the samples studied in my thesis.

Thanks to Lina, Pedro, Henrique and Luciano from the work group of Rafael for helping me at different points of my thesis.

Thanks to my family for supporting me and to my closest friends in Lima and São Paulo.

To Department of Mechanics and Materials Physics of the IFUSP for their facilities and laboratories.

This study was financed in part by the Coordenação de Aperfeiçoamento de Pessoal de Nível Superior – Brasil (CAPES) – Finance Code 001.

Resumo

Nos magnetos geometricamente frustrados, a competição entre interações magnéticas, em conjunto com a geometria da rede, inibem o estabelecimento de uma ordem de longo alcance. O arranjo tetraédrico dos íons magnéticos R nos pirocloros $R_2M_2O_7$ tem apresentado interessantes estados magnéticos, e muitos deles tem sido discutidos vastamente na literatura. Entretanto, as propriedades físicas dos íons R nos magnetos frustrados são fortemente modificadas na presença de desordem estrutural. Recentemente, a inclusão de desordem tem providenciado novas perspectivas no estudo dos pirocloros XY , nos gelos de spin e nos líquidos de spin. Neste trabalho, nós estudamos a diluição da subrede não magnética de M (Ti/Sn) nos pirocloros $Er_2Ti_{2-x}Sn_xO_7$ ($x = 0 - 2$), e as fluoritas desordenadas $R_2Zr_2O_7$ ($R = Dy, Ho$ e Tb), que possuem seus íons R e Zr localizados aleatoriamente na mesma subrede. Os compostos de érbio apresentam uma anisotropia planar de spin, nós estudamos a evolução do momento magnético, começando no estado ψ_2 , até a configuração Palmer–Chalker para diferentes valores x do $Er_2Ti_{2-x}Sn_xO_7$, usando dados de calor específico. Experimentos de susceptibilidade magnética ac e de calor específico foram realizados nas fluoritas desordenadas $R_2Zr_2O_7$; interações antiferromagnéticas e valores de momento magnéticos parecidos foram determinados no $Dy_2Zr_2O_7$ e $Ho_2Zr_2O_7$, divergindo das interações ferromagnéticas nos gelos de spin $Dy_2Ti_2O_7$ e $Ho_2Ti_2O_7$. A contribuição magnética ao calor específico apresenta um máximo associado a correlações em 2 K nas fluoritas desordenadas e uma ausência da entropia residual, de maneira oposta aos pirocloros gelos de spin. A desordem estrutural nas fluoritas exclui a possibilidade de correlações do tipo gelo de spin; esses compostos exibem flutuações de spin, junto com uma considerável quantidade de susceptibilidade, sem apresentar um estado canônico de vidro de spin. Espalhamento de nêutrons no $Dy_2Zr_2O_7$ confirmam a ausência de ordem de longo alcance e a existência de correlações magnéticas que se mantêm dinâmicas em 40 mK; essas correlações se estendem por 6.6 Å e na presença de campo magnético de 4 T, elas crescem até 23.6 Å. $Tb_2Zr_2O_7$ não apresenta ordem de longo alcance e temos flutuações de spin abaixo de 100 mK. Medidas dinâmicas apresentam um máximo com dependência na frequência aplicada. A mudança da posição do máximo foi ajustada usando diferentes modelos, mostrando uma transição para um estado canônico de vidro de spin em 2.2 K.

Palavras-chave: Magnetos Geometricamente Frustrados, Pirocloros, Fluoritas Desordenadas.

Abstract

In the geometrically frustrated magnets, competing magnetic interactions together with the lattice structure inhibit the system of establishing long range order. The tetrahedral arrangement of the magnetic R ions in the pyrochlores $R_2M_2O_7$ manifests the development of intriguing magnetic states which have been investigated vastly in the literature. However, the physical properties of the R ions in frustrated magnets are strongly affected when structural disorder is introduced. Recently, research probing disorder has provided interesting insights in XY pyrochlores, spin ices and spin liquids. In this work, we study the dilution of the nonmagnetic sublattice of M (Ti/Sn) in the pyrochlores $\text{Er}_2\text{Ti}_{2-x}\text{Sn}_x\text{O}_7$ ($x = 0 - 2$), and the defect-fluorites $R_2\text{Zr}_2\text{O}_7$ ($R = \text{Dy}, \text{Ho}$ and Tb), in which the R moments randomly reside on a sublattice together with the nonmagnetic Zr ions. The erbium compounds possess a strong local planar anisotropy, and with the dilution of the M sublattice, we study the evolution of the magnetic moment for all the x compositions starting from the ψ_2 state to the Palmer–Chalker configuration through a specific-heat analysis. In-field experiments suppress the long-range order transition and the H–T phase diagram exhibits two different trends for small and high x values. ac magnetic susceptibility and specific heat studies have been performed in the disordered fluorites $R_2\text{Zr}_2\text{O}_7$; antiferromagnetic correlations and similar magnetic moment were determined in $\text{Dy}_2\text{Zr}_2\text{O}_7$ and $\text{Ho}_2\text{Zr}_2\text{O}_7$, different from the ferromagnetic interactions in spin ices $\text{Dy}_2\text{Ti}_2\text{O}_7$ and $\text{Ho}_2\text{Ti}_2\text{O}_7$. Magnetic specific heat revealed a correlation broad peak around 2 K for the disordered fluorites as well as no Pauling’s residual entropy was observed, contrary to the pyrochlore spin ices. Disorder in both fluorites preclude the development of spin-ice correlations and exhibit fluctuating spins; with a significant amount of susceptibility, which do not freeze into a canonical spin glass. Neutron scattering studies in $\text{Dy}_2\text{Zr}_2\text{O}_7$ confirm no long-range order and antiferromagnetic correlations which remain dynamic down to 40 mK. These correlations extend over the length of 6.6 Å and with an external field of 4 T expand to 23.6 Å. $\text{Tb}_2\text{Zr}_2\text{O}_7$ presents no long-range order and exhibits spin fluctuations down to 100 mK. Dynamic measurements display a frequency-dependent maximum and different models to its shift temperature reveal a canonical spin-glass transition around 2.2 K.

Keywords: Geometrically Frustrated Magnetism, Pyrochlores, Disordered Fluorites.

Contents

Acknowledgements	ii
Resumo	iii
Abstract	iv
List of Figures	viii
List of Tables	xv
Chapter 1 Introduction	1
Chapter 2 Magnetism and Frustration	4
2.1 Magnetic moment	4
2.2 Magnetic interactions	5
2.2.1 Magnetic dipolar interactions	6
2.2.2 The Heisenberg and Ising models	6
2.2.3 Crystal-field interaction	7
2.3 Specific heat	8
2.4 Magnetic models	10
2.4.1 The Weiss model of a ferromagnet–antiferromagnet	10
2.4.2 Magnetic susceptibility	11
2.5 Geometrically frustrated magnetism	12
2.6 Geometrically frustrated lattices	14
2.7 Magnetic ground states in pyrochlores	16
2.7.1 $\text{Er}_2\text{Ti}_2\text{O}_7$ and $\text{Er}_2\text{Sn}_2\text{O}_7$	16
2.7.2 $\text{Dy}_2\text{Ti}_2\text{O}_7$ and $\text{Ho}_2\text{Ti}_2\text{O}_7$	18
2.7.3 $\text{Tb}_2\text{Ti}_2\text{O}_7$	20

2.7.4	Spin Glasses	22
Chapter 3	Experimental Methods	24
3.1	Sample preparation	24
3.1.1	Solid-state reaction	24
3.1.2	Sol-gel method	25
3.2	X-ray diffraction	26
3.3	Neutron diffraction	28
3.4	Rietveld refinement	31
3.5	Magnetic measurements	33
3.5.1	Adiabatic demagnetization refrigerator	33
3.5.2	Home-made ac susceptometer	34
3.5.3	Superconducting quantum interference device	36
3.6	Thermal measurements	38
3.6.1	Physical Property Measurement System	38
Chapter 4	Er₂Ti_{2-x}Sn_xO₇	43
4.1	Structural analysis	43
4.2	Specific heat	44
4.2.1	Zero field specific heat	44
4.2.2	In field specific heat	53
4.3	Discussion	59
Chapter 5	Dy₂Zr₂O₇	60
5.1	Structural analysis	60
5.2	DC magnetization	62
5.3	AC magnetic susceptibility	63
5.4	Specific heat	66
5.5	Neutron diffraction	69
5.6	Discussion	73
Chapter 6	Ho₂Zr₂O₇	74
6.1	Structural analysis	74
6.2	DC magnetization	76

6.3	AC magnetic susceptibility	77
6.4	Specific heat	80
6.5	Discussion	84
Chapter 7 $\text{Tb}_2\text{Zr}_2\text{O}_7$		85
7.1	Structural analysis	85
7.2	DC magnetization	87
7.3	AC magnetic susceptibility	88
7.4	Specific heat	92
7.5	Discussion	97
Chapter 8 Conclusion		99
8.1	Future work	100
Bibliography		101
Chapter A Nuclear specific heat		108

List of Figures

2.1	Spins on a linear arrangement illustrating its ground state corresponding to antiferromagnetic interactions.	7
2.2	CEF levels for the rare-earth ions R in the pyrochlores $R_2\text{Ti}_2\text{O}_7$. The computed and experimental levels are presented as solid and dashed lines, respectively. Solid thin and thick lines denote single and doublet states. Figure taken from [23].	8
2.3	Inverse of magnetic susceptibility versus temperature graphs for $\theta_{\text{CW}} = 0$ (paramagnet), $\theta_{\text{CW}} = \Theta > 0$ (ferromagnet) and $\theta_{\text{CW}} = \Theta < 0$ (antiferromagnet). Figure taken from [22].	12
2.4	Spins with antiferromagnetic exchange arranged on a triangle or tetrahedron are geometrically frustrated.	13
2.5	Geometrically frustrated lattices: edge-sharing triangular (a), and corner-sharing triangular or Kagomé, (b). Figure taken from [28].	13
2.6	Characteristic behaviour of $\chi^{-1}(T)$ for an antiferromagnet, a ferromagnet and a geometrically frustrated magnet (blue line).	14
2.7	<i>Left:</i> The R (blue) and M (red) sites of the pyrochlore lattice $R_2M_2O_7$. <i>Right:</i> The R site is surrounded by eight oxygen anions (yellow). Spin (red arrow) with XY anisotropy are confined in the plane perpendicular to their local [111] axis. Figures taken from [29].	15
2.8	Fluorite structure showing the mixing of the R and M cations. Figure from [30].	16
2.9	Specific heat versus temperature of $\text{Er}_2\text{Ti}_2\text{O}_7$ for different external fields. The transition peak vanishes for fields above 1.7 T. Figure taken from [31].	17
2.10	<i>Left:</i> Antiferromagnetic ψ_2 phase of $\text{Er}_2\text{Ti}_2\text{O}_7$. <i>Right:</i> The Palmer–Chalker state for $\text{Er}_2\text{Sn}_2\text{O}_7$. Figure taken from [29].	18

2.11	Ising spins decorating the vertices of a tetrahedron with the ice rule, oriented along their local easy-axis $\langle 111 \rangle$, and the analogy with the arrangement of protons (red circles) about oxygen (blue circles) in water ice. Figure adapted from [37].	18
2.12	Dy ₂ Ti ₂ O ₇ : (a) Specific heat and (b) entropy as a function of the temperature reported by [7]. The residual entropy of Dy ₂ Ti ₂ O ₇ , 1.86 J.K ⁻¹ .mol ⁻¹ , is in agreement with Pauling's entropy, $\frac{R}{2} \ln(\frac{3}{2}) = 1.68$ J.K ⁻¹ .mol ⁻¹ [7]. (a) and (b) also show a comparison with Monte Carlo simulations (MC data) of [8]. This figure was taken from [7].	20
2.13	ac susceptibility versus temperature at different frequencies. Figure from [38].	21
2.14	Specific heat versus temperature for different samples of Tb ₂ Ti ₂ O ₇ . Figure from [52] which displays data from [21], [53] and [54].	22
2.15	Neutron scattering of Y ₂ Mo ₂ O ₇ at 1.8 K. Inset: the four sublattices correspond to different colors in the vertices of the tetrahedra. Figure from [56].	23
3.1	<i>Right</i> : Dried gel of Ho ₂ Zr ₂ O ₇ after magnetic stirring at 80°C. <i>Left</i> : White powder of Ho ₂ Zr ₂ O ₇ after heat treatment of 950°C. Photo credits to P. Oliviera.	26
3.2	Bragg diffraction representation showing the incoming x-ray scattering from the atoms within the crystallographic planes. The path length difference is $2d \sin\theta$	27
3.3	Schematic image of the Bragg-Brentano diffractometer. The detector in the 2θ position measures the diffraction peaks of the incident angle θ . Figure modified from [65].	28
3.4	Schematic diagram of a diffractometer. Figure modified from [67].	31
3.5	<i>Left</i> : Magnetic refrigerator. Figure taken from [74]. <i>Right</i> : Cross-section of the liquid-helium magnet cryostat with the magnetic refrigerator inserted in its operating position.	34
3.6	Schematic diagram of the susceptometer inside the pumped ⁴ He cryostat. Figure adapted from [75].	35
3.7	Setup configuration of the primary and secondary pickup coils.	36
3.8	Diagram of the SQUID showing the Josephson junctions; denoted with X, and the superconducting ring. Φ is the magnetic flux, I is the current through the loop and U is the measured voltage.	37

3.9	Diagram of the detection setup of the SQUID. The pickup coils, the sample, and the detection loop are shown as well. Figure adapted from [77].	37
3.10	Inner components of the calorimeter puck of the PPMS. Figure adapted from [81].	38
3.11	Schematic of the dilution refrigerator. Figure adapted from [83].	41
3.12	Schematic of the ACMS insert. Figure adapted from [84].	42
4.1	X-ray powder diffraction pattern for the $x = 0$ composition. Peak positions of the pyrochlore structure are marked with small vertical lines. The line at the bottom shows the difference between the data and the refinement model. .	44
4.2	Temperature dependence of the total specific heat of $\text{Er}_2\text{Ti}_{2-x}\text{Sn}_x\text{O}_7$ ($x = 0 - 2$). The red points shows the estimated lattice contribution C_p	45
4.3	Height peak of specific heat C_{peak} and transition temperature T_N versus the x content.	45
4.4	Temperature dependence of the magnetic specific heat of $\text{Er}_2\text{Ti}_{2-x}\text{Sn}_x\text{O}_7$ ($x = 0 - 2$).	47
4.5	(a) The low-temperature magnetic specific heat of the series $\text{Er}_2\text{Ti}_{2-x}\text{Sn}_x\text{O}_7$ ($x = 0 - 2$). (b) The solid lines result from fitting the data to the sum $C_N + C_e$, as explained in the text.	49
4.6	(a) Variation in the magnetic moment μ_x with the x content in $\text{Er}_2\text{Ti}_{2-x}\text{Sn}_x\text{O}_7$ obtained from specific heat (SH), which occurs for values of μ_z zero (white area) and non-zero (green area). The values of the magnetic moments reported in [13] and obtained from magnetic neutron diffraction (ND) are included. (b) μ_{xy} and μ_z versus the x content.	50
4.7	Variation in the energy gap Δ and magnon velocity v with the x content in $\text{Er}_2\text{Ti}_{2-x}\text{Sn}_x\text{O}_7$	51
4.8	(a) Temperature dependence of the electronic specific heat C_e of the $\text{Er}_2\text{Ti}_{2-x}\text{Sn}_x\text{O}_7$ series. (b) The recovered electronic entropy ΔS_e as a function of the temperature. The dashed line $R \ln(2)$ denotes the expected value for a doublet ground state.	52
4.9	Specific heat of $\text{Er}_2\text{Ti}_{2-x}\text{Sn}_x\text{O}_7$ ($x = 0, 0.5, 1.0, 1.5, 1.7$ and 1.8) for different applied magnetic fields. T_N marks the temperature of the ordering transition at zero field.	54

4.10	Temperature dependence of the specific heat of $\text{Er}_2\text{Sn}_2\text{O}_7$ for different magnetic fields. T_N marks the temperature of the ordering transition at zero field.	55
4.11	The phase diagram of the $\text{Er}_2\text{Ti}_{2-x}\text{Sn}_x\text{O}_7$ series ($x = 0 - 2$) derived from specific-heat measurements in different magnetic fields. The open symbols show experimental data from Dalmas de Réotier <i>et al.</i> [31]. The lines connecting the symbols are guides to the eye.	56
4.12	Temperature dependence of C/T of $\text{Er}_2\text{Ti}_{2-x}\text{Sn}_x\text{O}_7$ ($x = 0, 0.5, 1, 1.5, 1.7$ and 1.8) measured in different applied magnetic fields. Red solid lines show fits of C to the equation 2.17.	57
4.13	Temperature dependence of C/T of $\text{Er}_2\text{Sn}_2\text{O}_7$ ($x = 2$) in different applied magnetic fields.	58
4.14	Gap values $\Delta\varepsilon$ determined from fitting the in-field data to equation 2.17. The open symbols show experimental data from Sosin <i>et al.</i> [91].	59
5.1	XPD pattern for $\text{Dy}_2\text{Zr}_2\text{O}_7$ (a), NPD pattern for $^{162}\text{Dy}_2\text{Zr}_2\text{O}_7$ (b), and their respective calculated profiles. Peak positions of the fluorite structure are marked with small vertical lines. The solid blue lines show the difference between the data and the refinement model.	61
5.2	(a) Inverse susceptibility versus temperature and Curie-Weiss fit to the lowest temperature. The inset shows the data measured in an extended temperature range. (b) Saturation magnetization as a function of the applied field shows a saturation moment at a value of approximately $5 \mu_B/\text{Dy}$ (dashed line).	63
5.3	Real part of the ac magnetic susceptibility χ'_{ac} versus temperature for different frequencies in zero magnetic field for $\text{Dy}_2\text{Zr}_2\text{O}_7$ and $\text{Dy}_2\text{Ti}_2\text{O}_7$	64
5.4	Frequency of the measurement (f) versus the inverse of the temperature of the maximum in χ'_{ac} ($1/T'$) with a fit to the Arrhenius law.	65
5.5	Characteristic spin-relaxation time τ as a function of temperature in $\text{Dy}_2\text{Zr}_2\text{O}_7$ and $\text{Dy}_2\text{Ti}_2\text{O}_7$ (digitalized from Snyder <i>et al.</i> [97]).	66
5.6	Temperature dependence of the total specific heat for $\text{Dy}_2\text{Zr}_2\text{O}_7$, $\text{Dy}_2\text{Ti}_2\text{O}_7$, and $^{162}\text{Dy}_2\text{Zr}_2\text{O}_7$ at zero field. The lattice terms (C_{p1} and C_{p2}) and the nuclear specific heat (C_N) are displayed.	67

5.7	(a) Electronic specific heat $C_e(T)$ at zero field. Solid lines are the two-level Schottky fits using equation (2.17). (b) Recovered electronic entropy ΔS_e versus temperature. The dashed lines denote the expected values of entropy for a two-level system ($R \ln 2$) and spin ices.	68
5.8	(a) Magnetic neutron diffraction for $^{162}\text{Dy}_2\text{Zr}_2\text{O}_7$ measured at 40 mK. (b) Neutron powder diffraction pattern at 10 K displays structural Bragg peaks.	69
5.9	Magnetic neutron diffraction for $^{162}\text{Dy}_2\text{Zr}_2\text{O}_7$ at 40 mK. The powder-averaged dipolar spin-ice model and the Gardner-Berlinsky model are plotted.	70
5.10	(a) Magnetic neutron diffraction for $^{162}\text{Dy}_2\text{Zr}_2\text{O}_7$ at 40 mK in different applied fields. (b) The broad diffraction peak at 1.15 \AA^{-1} for field values up to 1.2 T. The dataset in both panels are offset for clarity.	71
5.11	(a) Magnetic diffraction at 0 and 1 T plotted with their respective Gaussian fits. (b) Field dependence of the correlation length determined from the Gaussian width of the broad maxima see around 1.2 \AA^{-1}	72
6.1	X-ray powder diffraction patterns of $\text{Ho}_2\text{Zr}_2\text{O}_7$ synthesized at different temperatures. Vertical lines denote the peaks of the fluorite structure.	75
6.2	X-ray diffraction pattern and calculated profile data for $\text{Ho}_2\text{Zr}_2\text{O}_7$. The difference between the experimental and calculated data is showed in blue. Peak positions of the fluorite structure are marked with small vertical lines.	76
6.3	(a) Temperature dependence of the inverse susceptibility and Curie-Weiss fits for $\text{Ho}_2\text{Zr}_2\text{O}_7$ and $\text{Ho}_2\text{Ti}_2\text{O}_7$. (b) Saturation magnetization versus the applied magnetic field shows a saturation moment close to $5 \mu_B/\text{Ho}$ ion (dashed line).	77
6.4	Temperature dependence of the real part of the ac susceptibility χ'_{ac} for different frequencies in zero applied field for $\text{Ho}_2\text{Zr}_2\text{O}_7$ and $\text{Ho}_2\text{Ti}_2\text{O}_7$	78
6.5	Frequency of the measurement (f) versus the inverse of the temperature of the maximum in χ'_{ac} ($1/T'$) with a fit to the Arrhenius law for $\text{Ho}_2\text{Zr}_2\text{O}_7$. Digitalized data of Matsuhira <i>et al.</i> [111] and Quilliam <i>et al.</i> [112] for $\text{Ho}_2\text{Ti}_2\text{O}_7$ are also displayed.	79
6.6	Temperature dependence of the total specific heat C of $\text{Ho}_2\text{Zr}_2\text{O}_7$ at zero field. The C data of Lau <i>et al.</i> [30] for $\text{Ho}_2\text{Ti}_2\text{O}_7$ are displayed. The specific heat of the isostructural nonmagnetics $\text{Lu}_2\text{Zr}_2\text{O}_7$ (C_{p1}) and $\text{Lu}_2\text{Ti}_2\text{O}_7$ (C_{p2}), and the nuclear specific heat computed as explained in the text are shown.	80

6.7	(a) The electronic specific heat C_e versus temperature of $\text{Ho}_2\text{Zr}_2\text{O}_7$ at zero field. The C_e values of $\text{Ho}_2\text{Ti}_2\text{O}_7$ were obtained by subtracting C_{p2} and C_N to the dataset of Lau <i>et al.</i> [30]. The two-level Schottky fits using equation (2.17) are shown as solid lines. (b) The electronic magnetic entropy ΔS_e versus temperature. The dashed lines denote $R \ln 2$ for a two-level spin system and the presence of residual entropy for spin ices.	82
6.8	(a) The temperature dependence of C for $\text{Ho}_2\text{Zr}_2\text{O}_7$ in different applied magnetic fields. Gray solid lines are guides to the eyes. (b) The C_e curves versus temperature and their respective two-level Schottky fits using equation (2.17), shown as solid lines. (c) The linear dependence of the energy gaps $\Delta\varepsilon$ as a function of the applied field H	83
7.1	X-ray powder diffraction for heat-treated samples of $\text{Tb}_2\text{Zr}_2\text{O}_7$ at different temperatures.	86
7.2	X-ray diffraction pattern and calculated profile data for $\text{Tb}_2\text{Zr}_2\text{O}_7$. The difference between the experimental and calculated data is showed in blue. Peak positions of the fluorite structure are marked with small vertical lines.	87
7.3	(a) Temperature dependence of the inverse susceptibility and Curie-Weiss fit for $\text{Tb}_2\text{Zr}_2\text{O}_7$. (b) Saturation magnetization versus the applied magnetic field for $\text{Tb}_2\text{Zr}_2\text{O}_7$ shows a saturation moment close to $5 \mu_B/\text{Tb}$ ion.	88
7.4	(a) Real Part of the ac susceptibility χ'_{ac} as a function of the temperature in zero magnetic field for $\text{Tb}_2\text{Zr}_2\text{O}_7$. (b) Imaginary Part of the ac susceptibility χ''_{ac} as a function of the temperature in zero magnetic field for $\text{Tb}_2\text{Zr}_2\text{O}_7$	89
7.5	(a) Frequency of the measurement (f) versus the inverse of the temperature of the maximum in χ'_{ac} ($1/T'$) with a fit to the Arrhenius law. Logarithmic spin-relaxation time ($\ln \tau$) fitted to the dynamic scaling law (b), to the Vogel-Fulcher law (c) and to the equation $\tau = \tau_0 \exp[(-E/T')^\sigma]$ (d).	91
7.6	The temperature dependence of χ'_{ac} for $\text{Tb}_2\text{Zr}_2\text{O}_7$ at different frequencies in various applied fields.	92
7.7	Specific heat C as a function of temperature for $\text{Tb}_2\text{Zr}_2\text{O}_7$ in zero field. The specific heat of the isostructural nonmagnetic $\text{Lu}_2\text{Zr}_2\text{O}_7$ (C_p) and the computed nuclear specific heat (C_N) are displayed.	93

7.8	Specific heat C versus temperature for $\text{Tb}_2\text{Zr}_2\text{O}_7$ in the low-temperature regime. The estimations for the specific heat C_{TbMet} and nuclear contributions C_N and C_{N1} are displayed. We show for comparison the nuclear term of the compound $\text{Tb}(\text{OH})_3$	94
7.9	(a) The electronic specific heat $C_e(T)$ of $\text{Tb}_2\text{Zr}_2\text{O}_7$ at zero field and the two-level Schottky fit using equation (2.17) (solid line). (b) The electronic magnetic entropy $\Delta S_e(T)$ for $\text{Tb}_2\text{Zr}_2\text{O}_7$. The dashed lines denote the entropy for a two level system ($R \ln 2$) and the entropy reported for $\text{Tb}_2\text{Ti}_2\text{O}_7$ ($R \ln 4$) [21, 54].	95
7.10	(a) The total specific heat $C(T)$ for $\text{Tb}_2\text{Zr}_2\text{O}_7$ in different applied magnetic fields. Gray solid lines are guides to the eyes. (b) The electronic specific heat $C_e(T)$ in fields up to 6 T. Solid lines are the two-level Schottky fits using equation 2.17. (c) Gap values $\Delta\varepsilon$ determined from the Schottky fit as a function of the applied field H	96
A.1	Program implemented in Python for the account of the nuclear specific heat of the $\text{Er}_2\text{Ti}_{2-x}\text{Sn}_x\text{O}_7$ series.	109
A.2	Program implemented in Python for the account of the electronic specific heat of the $\text{Er}_2\text{Ti}_{2-x}\text{Sn}_x\text{O}_7$ series.	110
A.3	Program implemented in Wolfram Mathematica 12.0 for the account of the nuclear specific heat of the disordered fluorites. As an example is shown the nuclear specific heat of metallic Tb used in the analysis of $\text{Tb}_2\text{Zr}_2\text{O}_7$	111

List of Tables

5.1	Refined structural parameters for $\text{Dy}_2\text{Zr}_2\text{O}_7$ and $^{162}\text{Dy}_2\text{Zr}_2\text{O}_7$	62
5.2	Frequency f , the temperature T' , and the $\delta T'$ values for $\text{Dy}_2\text{Zr}_2\text{O}_7$. † results from the values marked with a and b , ‡ comes from the values labelled with b and c , and * results from the values marked with c and d	65
6.1	Frequency f , the temperature T' , and the $\delta T'$ values for $\text{Ho}_2\text{Zr}_2\text{O}_7$. † results from the values marked with a and b , ‡ comes from the values labelled with b and c , and * results from the values marked with c and d	79
7.1	Frequency f , the temperature T' , and the $\delta T'$ values for $\text{Tb}_2\text{Zr}_2\text{O}_7$. † results from the values marked with a and b , ‡ comes from the values labelled with b and c , * results from the values marked with c and d	90

Introduction

Geometrically frustrated magnetism is a central topic in modern condensed matter physics for giving rise to a diverse set of highly correlated magnetic phases. This rich phenomenology in possible materials has attracted enormous interest and extensive investigations over the last twenty years [1,2]. The competition between nearest-neighbour and further interactions, in together with the arrangement of the magnetic sites play an important role selecting the magnetic ground states or spin configurations, but also can lead to perpetually dynamic magnetism [1–3]. Frustrated systems cannot minimize the energy of all their interactions simultaneously, and this could lead to a large degeneracy of ground states even at extremely low temperatures [1,2]. The concept of frustration is fundamental outside of magnetism in the study of negative thermal expansion of materials, soft matter and protein folding kinetics [2,4].

Geometrically frustrated magnets are often based on triangular or tetrahedral lattices. Experimental realizations are the pyrochlores with the chemical formula $R_2M_2O_7$ in which R^{3+} is a magnetic rare-earth ion (e.g., Tb, Ho, Dy, Er, Gd) and M^{4+} is a transition-metal ion (e.g., Ti, Sn, Zr, Ge). Both cations reside on two distinct lattices of corner-sharing tetrahedra and if either R or M is magnetic, frustration can develop. The rare-earth series of pyrochlore titanates; $R_2Ti_2O_7$, have displayed a remarkable broad range of phenomena including the spin liquid $Tb_2Ti_2O_7$ [5,6], the spin ices $Ho_2Ti_2O_7$ and $Dy_2Ti_2O_7$ [7,8], the long-range magnetic ordering induced by fluctuations in $Er_2Ti_2O_7$ [9], the partial magnetic ordering in $Gd_2Ti_2O_7$ [10–12] among others [2].

Besides the pyrochlore titanates mentioned above, research on isostructural examples has also been discussed on the pyrochlore stannates, $R_2Sn_2O_7$. The substitution of Ti^{4+}

by Sn^{4+} can dramatically alter the magnetic properties of the system down to low temperatures. For example, $\text{Tb}_2\text{Ti}_2\text{O}_7$ remains in a dynamic cooperative magnetic state down to 0.05 K while $\text{Tb}_2\text{Sn}_2\text{O}_7$ develops long-range order below 0.87 K driven by antiferromagnetic and ferromagnetic correlations. $\text{Gd}_2\text{Ti}_2\text{O}_7$ orders antiferromagnetically through two magnetic transitions leading to partial ordering, and $\text{Gd}_2\text{Sn}_2\text{O}_7$ possesses only one transition and classical long-range order. On the other hand, the spin-ice state appear to be very robust to the substitution of Ti by Sn. For $\text{Er}_2\text{Sn}_2\text{O}_7$, long-range order is developed [13, 14] and the magnetic ground state was reported to be Palmer-Chake type [15]. In this work, we study the erbium based pyrochlores $\text{Er}_2\text{Ti}_{2-x}\text{Sn}_x\text{O}_7$.

To understand the wealth phenomena in $R_2M_2O_7$, researchers have begun to look beyond the typical non-magnetic M site. Recently, several groups have been working on geometrically frustrated hafnates ($R_2\text{Hf}_2\text{O}_7$) and zirconates ($R_2\text{Zr}_2\text{O}_7$). The $R_2M_2O_7$ compounds could also crystallize in the disordered defect-fluorite structure for small lanthanide elements. This structure depends strongly of the ratio between ionic radii r_R/r_M [2]. In the defect-fluorite, the cations R and M occupy a single site becoming disordered in the lattice. For the rare-earth zirconates $R_2\text{Zr}_2\text{O}_7$, the ones with light-rare-earth R cation have attracted much interest for their particular electronic properties. For example, in $\text{Pr}_2\text{Zr}_2\text{O}_7$ spin-ice-like correlations and quantum fluctuations of magnetic monopoles were reported [16]. For $\text{Nd}_2\text{Zr}_2\text{O}_7$, neutron-scattering results revealed the co-existence of a fluctuating Coulomb phase with an ordered one [17]. Another examples are $\text{Tb}_2\text{Hf}_2\text{O}_7$ and $\text{Pr}_2\text{Hf}_2\text{O}_7$ in which long-range ordered ground states are prevented down to 100 mK [18, 19].

In Chapter 2, we present the fundamentals of the magnetic interactions in spin systems. We also study how frustration is involved with magnetic systems. We study the crystal structures of the pyrochlore and of the disordered-fluorite materials which are the focus of this thesis. We review previous results concerning the low-temperature magnetic phases of the pyrochlore compounds that have the same rare earth in $R_2M_2O_7$ as the compounds studied in this work. For example, $\text{Er}_2\text{Ti}_2\text{O}_7$, $\text{Er}_2\text{Sn}_2\text{O}_7$, the spin ices $\text{Dy}_2\text{Ti}_2\text{O}_7$ and $\text{Ho}_2\text{Ti}_2\text{O}_7$ and the spin liquid $\text{Tb}_2\text{Ti}_2\text{O}_7$. The proposed magnetic states are studied from magnetic, thermal, and neutron diffraction results of the literature.

In Chapter 3, we study the physical phenomena and operating concerning the experiments used in this work. We detailed the synthesis employed to prepare polycrystalline

powder of $\text{Er}_2\text{Ti}_{2-x}\text{Sn}_x\text{O}_7$, $\text{Dy}_2\text{Zr}_2\text{O}_7$, $\text{Ho}_2\text{Zr}_2\text{O}_7$ and $\text{Tb}_2\text{Zr}_2\text{O}_7$. The structural analysis was carried out by performing x-ray powder diffraction. We present the basics of neutron diffraction to determine magnetic structures and their correlations. Magnetic measurements were studied using an adiabatic demagnetization refrigerator, an ac home-made susceptometer, a superconducting quantum interference device SQUID, while thermal experiments were performed by using a commercial calorimeter and a dilution refrigerator.

In Chapter 4, we study the family of XY pyrochlores erbium based $\text{Er}_2\text{Ti}_{2-x}\text{Sn}_x\text{O}_7$ with $x = 0$ to 2. For $\text{Er}_2\text{Ti}_2\text{O}_7$ ($x = 2$) the magnetic moment of Er^{3+} is proposed to exhibit XY anisotropy, in which the spins are constrained to lie in the plane perpendicular to their local [111] axis [20]. However, for $\text{Er}_2\text{Sn}_2\text{O}_7$ the magnetic state observed is reported as Palmer-Chake state [13, 14]. We present an analysis of experimental thermal results at very low temperature including evidence that there is a change of spin anisotropy through the series $\text{Er}_2\text{Ti}_{2-x}\text{Sn}_x\text{O}_7$.

In Chapter 5 and Chapter 6 we discuss about the low-temperature magnetic and thermal behaviour of the zirconates $\text{Dy}_2\text{Zr}_2\text{O}_7$ and $\text{Ho}_2\text{Zr}_2\text{O}_7$, respectively. These compounds has the same rare earth on the site R as the pyrochlores $\text{Dy}_2\text{Ti}_2\text{O}_7$ and $\text{Ho}_2\text{Ti}_2\text{O}_7$, but displays a different disordered structure. $\text{Dy}_2\text{Ti}_2\text{O}_7$ and $\text{Ho}_2\text{Ti}_2\text{O}_7$ are remarkable examples of spin ices in which the spin configuration satisfies the 2-in 2-out ice rules, with a strong anisotropy of the type Ising-like spin [7, 8]. AC susceptibility experiments give insights in the dynamics of $\text{Dy}_2\text{Zr}_2\text{O}_7$ and $\text{Ho}_2\text{Zr}_2\text{O}_7$. Specific heat experiments found short-range correlations for both compounds and recovered entropy values different from spin ices. Neutron experiments in $\text{Dy}_2\text{Zr}_2\text{O}_7$ reveal the nature of these correlations and its length on the lattice.

In Chapter 7, we discuss about the low-temperature magnetism of the $\text{Tb}_2\text{Zr}_2\text{O}_7$ compound. We present results of the dynamic susceptibility and specific heat. We perform different analysis to the ac susceptibility to probe its spin glass character. The analysis of the specific heat suggest the presence of fluctuations.

Finally, in Conclusions we will sum up the most important results of this thesis and we will mention the work concerning future perspectives.

Magnetism and Frustration

This chapter is an introduction to the main themes of my work which are magnetism and geometric frustration. First, we study the concept of magnetic moment, the interactions between magnetic moments, and how they are modified by their local environment in a crystal. Afterwards, we deal with how the combination of the local moments and interactions leads to ordered phases. We define the concept of geometrical frustration and its implications on exotic magnetic phases, and then we describe the crystal structure of experimental realizations subject to frustration. Finally, we summarize results covering examples of rare-earth frustrated systems which are the focus of this thesis as the XY pyrochlores $\text{Er}_2\text{Ti}_2\text{O}_7$ and $\text{Er}_2\text{Sn}_2\text{O}_7$, the spin ices $\text{Dy}_2\text{Ti}_2\text{O}_7$ and $\text{Ho}_2\text{Ti}_2\text{O}_7$, and the spin liquid $\text{Tb}_2\text{Ti}_2\text{O}_7$.

2.1 Magnetic moment

The magnetic moment of atoms is a contribution of the motion of electrons and the intrinsic spin, and it occurs in compounds that have atoms with unfilled electronic shells. Examples in nature are the rare earth elements with partially filled $4f$ shells and the $3d$ ions of the transition metal series. Classically, a magnetic moment is pictured as a circulating current loop. For a moving particle in a loop with charge e , mass m_e , and angular momentum L , the magnetic moment μ can be expressed as

$$\mu = -\frac{e\hbar}{2m_e}\mathbf{L}, \quad (2.1)$$

where \mathbf{L} is the orbital angular momentum and $e\hbar/2m_e$ is the unit of the magnetic moment size named the Bohr magneton μ_B with a value of 9.274×10^{-24} A.m². Electrons

have also spin angular momentum and then its magnetic moment is given by

$$\mu_s = -g_s \frac{\mu_B}{\hbar} \mathbf{S}, \quad (2.2)$$

where \mathbf{S} is the spin of the electron and g is the spin g-factor, which for an electron is nearly equal to 2. The total magnetic moment at each atom is associated with its total angular momentum $\mathbf{J} = \mathbf{L} + \mathbf{S}$ which is a sum of the orbital and spin degrees of freedom, then

$$\mu_J = -g_J \frac{\mu_B}{\hbar} \mathbf{J}, \quad (2.3)$$

where the constant g_J is the Landé g-factor; which for atoms with the approximation $g_s = 2$, is defined as

$$g_J = \frac{3}{2} + \frac{S(S+1) - L(L+1)}{2J(J+1)}. \quad (2.4)$$

Due to the quantized nature of the angular momentum, the magnitude of the total magnetic moment is given by

$$\mu_J = g_J \mu_B \sqrt{J(J+1)}. \quad (2.5)$$

The values of the quantum numbers L , S , and J for the ground state configuration of a many-electrons system is determined by the Hund's rules. The first one establishes that the largest total spin number S is the lowest in energy. For a spin configuration selected by the first rule, the second one dictates that the ground state maximize the value of the orbital quantum number L . For the values selected of L and S , the total quantum number J favours the value $|L - S|$ for less than half-filled shells and the maximum value $L + S$ for more than half-filled shells. The many-electron ground configuration is represented by the term symbol $^{2S+1}L_J$, where the total orbital quantum number is denoted by the letters S, P, D, F, G, H , etc. The Hund's rules are well satisfied by the rare-earth ions since their outer $4f$ shell electrons are confined in the space lying deep the $5s$ and $5p$ shells. Therefore, they are usually treated as free ions.

2.2 Magnetic interactions

In many-electron systems, each magnetic moment of the electrons influences its neighbours through different magnetic interactions. We will study some of these interactions between magnetic moments.

2.2.1 Magnetic dipolar interactions

The dipolar interaction is the most familiar one on a macroscopic scale as it gives rise to observable magnetic fields. In the case of small magnetic moments, this interaction is weak and is usually the contribution of least importance for magnetic order. The energy for the dipolar interaction, for two magnetic spins \mathbf{S}_i and \mathbf{S}_j , separated by \mathbf{r}_{ij} is given by,

$$\mathcal{H}_{dip} = (g\mu_B)^2 \sum_{ij} \left[\frac{\mathbf{S}_i \cdot \mathbf{S}_j}{r_{ij}^3} - 3 \frac{(\mathbf{S}_i \cdot \mathbf{r}_{ij})(\mathbf{S}_j \cdot \mathbf{r}_{ij})}{r_{ij}^5} \right], \quad (2.6)$$

where g is the electron spin g -factor and μ_B is the Bohr magneton. This interaction is generally insignificant since it is much weaker than the exchange interaction. However, it can play an important role in materials that order at milliKelvin temperatures with large moments, such in the rare-earth magnets.

2.2.2 The Heisenberg and Ising models

The Heisenberg model describes the interaction between neighbouring spins and the Hamiltonian for this model, written in terms of the Heisenberg exchange J_{ij} and the spin operators \mathbf{S}_i at sites i , has the form

$$\mathcal{H} = - \sum_{ij} J_{ij} \mathbf{S}_i \cdot \mathbf{S}_j, \quad (2.7)$$

where the sum runs over nearest-neighbour pairs at sites ij . The spins \mathbf{S}_i are treated as three-dimensional vectors since there is no constraint to them, so they are allowed to point in any direction in the three-dimensional space. While the Hamiltonian above provides a suitable starting point for understanding the properties of many geometrically frustrated magnets, for a more realistic model various additional terms to the Hamiltonian are required [1].

In the Ising model, the spins possess only two discrete orientations that is can only point up or down. In other words, we restrict to the z component of the spin. The Hamiltonian of the Ising model is

$$\mathcal{H} = - \sum_{ij} J_{ij} \mathbf{S}_i^z \cdot \mathbf{S}_j^z, \quad (2.8)$$

here the spins \mathbf{S}_i are taken as one-dimensional vectors (the spins are only allowed to point along $\pm z$). A simple configuration is when the Ising spins are placed on a linear

chain, as shown in figure 2.1. If we assume $J_{ij} < 0$, the ground state is obtained by having antiparallel collinear spin alignments meaning antiferromagnetic correlations. On the other hand for $J_{ij} > 0$, a parallel spin alignment favours the ground state.

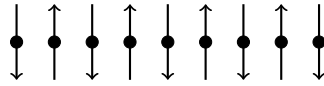


Figure 2.1: Spins on a linear arrangement illustrating its ground state corresponding to antiferromagnetic interactions.

2.2.3 Crystal–field interaction

Now we consider the effect of the local environment surrounding an ion on its energy levels. In the simplest picture, a central ion is surrounded by point charges that lie on neighboring sites. The electrostatic field known as the crystal electric field (CEF) produces an additional Coulomb energy that must be taken into account. For example, in $4f$ electrons of the rare–earth ions, this effect can be considered as a perturbation since its energy scale is usually smaller than the energy of Hund’s rules. On the other hand, for $3d$ electrons of the transition metals, the order of magnitude of the CEF levels can be stronger than the spin–orbit coupling. Then, the total angular momentum J does not work as good quantum number in these ions. In addition, the measured moment can only be explained if the values $L = 0$ and $J = S$ are assumed, which is known as the quenching of the angular momentum. Quenching results of the symmetry lowering of the effective electronic potential due to the charges around the magnetic ion. As an example, we show in figure 2.2 from [23] some computed and experimental CEF energy levels of the compounds $R_2\text{Ti}_2\text{O}_7$ where R is a rare–earth ion.

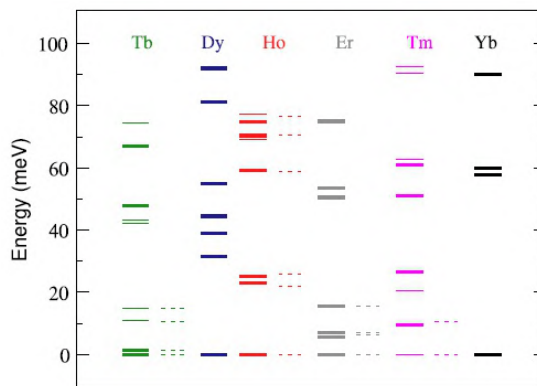


Figure 2.2: CEF levels for the rare-earth ions R in the pyrochlores $R_2\text{Ti}_2\text{O}_7$. The computed and experimental levels are presented as solid and dashed lines, respectively. Solid thin and thick lines denote single and doublet states. Figure taken from [23].

2.3 Specific heat

The specific heat C being a thermodynamic quantity is defined by the amount of heat required to raise the temperature of a unit mass by a temperature unit degree. C can be expressed by the equation:

$$C = \left(\frac{dQ}{dT} \right), \quad (2.9)$$

where dQ is the applied heat, and dT is the resultant change in temperature. For most bulk measurements, C experiments are carried on at constant pressure.

For the insulating frustrated magnets, the total specific heat C can be separated in different contributions as:

$$C = C_p + C_e + C_N, \quad (2.10)$$

where C_p is the specific heat due to the phonons or lattice, C_e is the electronic magnetic contribution, and C_N is the nuclear magnetic contribution.

First, we describe the lattice contribution C_p to the specific heat total. The Debye model provides an excellent fit to the low temperature specific heat of the phonons of many solids [24]. In the low-temperature regime, the lattice contribution to the specific heat is given by [24]

$$C_p = \frac{12\pi^4}{5} n k_B \left(\frac{T}{\Theta_D} \right)^3 = \beta T^3. \quad (2.11)$$

where Θ_D is the Debye characteristic temperature, n is the atom concentration in the solid, and k_B is the Boltzmann constant.

The electronic magnetic specific heat C_e is computed by considering magnons or spin waves, which are collective spin excitations. For example, the procedure proposed in [9] for the pyrochlore antiferromagnet $\text{Er}_2\text{Ti}_2\text{O}_7$ assumes that the dispersion relation $\hbar\omega(\mathbf{q})$ for low-energy magnons can be approximated at small wave vectors as

$$\hbar^2\omega^2(\mathbf{q}) = \hbar^2\omega^2(q) = \Delta^2 + \hbar^2v_{sw}^2q^2, \quad (2.12)$$

where Δ is the gap energy of the spectrum at the zone center and v_{sw} is the magnon velocity. Then, the expected electronic magnetic contribution C_e is derived [9]:

$$C_e(T) = A_v \left(\frac{15}{16\pi^4} \int_0^\infty dX \frac{X^2 (X^2 + (\Delta/T)^2)}{\sinh^2 \left(\frac{\sqrt{X^2 + (\Delta/T)^2}}{2} \right)} \right) T^3 \quad (2.13)$$

with

$$A_v = \frac{\pi^2}{120} N_A \frac{k_B^4 a^3}{\hbar^3 v^3} = 1534.5 \frac{a^3}{v^3}, \quad (2.14)$$

where Δ is the gap energy of the magnon spectrum at the zone center, N_A is the Avogadro's number, a is the lattice constant $\sim 10 \text{ \AA}$, and v is the magnon velocity. The expression for $C_e(T)$ could be written as:

$$C_e(T) = A_v \cdot I_\Delta(T) \cdot T^3. \quad (2.15)$$

Finally, we will discuss the case of the nuclear magnetic contribution C_N to the specific heat. This contribution arises from the combination of a nuclear electric quadrupole interaction, and a nuclear magnetic hyperfine interaction of the magnetic atoms. Then, the nuclear specific heat is given by [25]

$$C_N = \frac{R}{(k_B T)^2} \frac{\sum_{i,j} (W_i^2 - W_i W_j) \exp[-(W_i + W_j)/k_B T]}{\sum_{i,j} \exp[-(W_i + W_j)/k_B T]}, \quad (2.16)$$

where $i, j = -I, -I+1, \dots, I$ with I the number of spin nuclear, and W_i the nuclear energy of the i level.

An additional contribution to the specific heat that we will or is known as the Schottky anomaly. This anomaly occurs in systems with quantized energy levels and is reflected in the specific heat by the presence of a maximum. For example, for a spin S there are $2S+1$ possible orientations of the spin; in a magnetic field, there are a number of discrete energy levels. So, when the temperature is comparable to the energy separation there is

a broad peak in the specific heat due to a large change in entropy for a small change in temperature. For a system with two energy levels the Schottky specific heat C_{Sch} at a temperature T is given by [26]

$$C_{\text{Sch}} = R \left(\frac{\Delta\varepsilon}{k_{\text{B}}T} \right)^2 \frac{g_0}{g_1} \frac{\exp(\Delta\varepsilon/k_{\text{B}}T)}{[1 + (g_0/g_1) \exp(\Delta\varepsilon/k_{\text{B}}T)]^2}, \quad (2.17)$$

where g_0 and g_1 are the degeneracies of the two energy levels, $\Delta\varepsilon$ is the excitation gap, and $R = 8.314 \text{ J.K}^{-1}.\text{mol}^{-1}$ is the gas constant.

2.4 Magnetic models

A ferromagnet material has a spontaneous magnetization or density of magnetic moments even in the absence of an applied field. The magnetic moments could lie along a single unique direction, being this the effect of exchange interactions. For a ferromagnet in an applied magnetic field \mathbf{B} , the Hamiltonian of interaction is:

$$\mathcal{H} = - \sum_{(ij)} J_{ij} \mathbf{S}_i \cdot \mathbf{S}_j - g\mu_B \sum_{(i)} \mathbf{S}_i \cdot \mathbf{B}, \quad (2.18)$$

where the exchange constants for nearest neighbours will be positive (negative) to ensure ferromagnetic (antiferromagnetic) alignment. The first and second terms on the right are the Heisenberg exchange energy and the Zeeman energy, respectively.

2.4.1 The Weiss model of a ferromagnet–antiferromagnet

In order to discuss the transition temperature to a ferromagnetic state, it is introduced the Weiss model [22]. This procedure requires to define the effective mean (or molecular) field at the i -site given by [22]

$$\mathbf{B}_{mf} = \frac{2}{g\mu_B} \sum_i J_{ij} \mathbf{S}_i. \quad (2.19)$$

By looking at the i th spin in (2.18), we have that its energy is due to an exchange part and a Zeeman part $-g\mu_B \mathbf{S}_i \cdot \mathbf{B}$. The total exchange interaction between the i th spin and its neighbours is $-2 \sum_j J_{ij} \mathbf{S}_i \cdot \mathbf{S}_j$ and then can be written as

$$-2 \mathbf{S}_i \sum_j J_{ij} \cdot \mathbf{S}_j = -g\mu_B \mathbf{S}_i \cdot \mathbf{B}_{mf}. \quad (2.20)$$

The exchange interaction is replaced by the effective mean field \mathbf{B}_{mf} produced by the neighbouring spins. In this approach all magnetic ions experience an identical mean field. The effective Hamiltonian (2.21) can now be written as

$$\mathcal{H} = -g\mu_B \sum_i \mathbf{S}_i \cdot (\mathbf{B}_{mf} + \mathbf{B}) \quad (2.21)$$

which can be picture as the Hamiltonian for a magnet in a magnetic field $\mathbf{B}_{mf} + \mathbf{B}$. For a ferromagnet the mean field will act to align neighbouring magnetic moments, and for an antiferromagnet it will establish an antiparallel alignment. The mean field measures the effect of the ordering of the system, it is assumed that

$$\mathbf{B}_{mf} = \lambda \mathbf{M}, \quad (2.22)$$

where λ is a constant for parametrizing the intensity of the mean field as a function of the magnetization. For the case of a ferromagnet $\lambda > 0$.

In ferromagnets, below the Curie temperature T_C the magnet orders spontaneously and gives rise to bulk magnetism. The Curie temperature is the point at which the susceptibility presents an anomaly, and is given by [22]

$$T_C = \frac{g\mu_B(J+1)\lambda M_s}{3k_B} = \frac{n\lambda\mu_{eff}^2}{3k_B}, \quad (2.23)$$

where λ is the parameter representing the mean field, M_s is the saturation magnetization, $\mu_{eff} = g\mu_B\sqrt{J(J+1)}$ the effective magnetic moment, J total quantum number, g Landé g -factor, μ_B the Bohr magneton and $k_B = 1.38062 \times 10^{-23}$ J.K⁻¹ Boltzmann's constant. The order parameter λ is related to the exchange constant J by [22]:

$$\lambda = \frac{2zJ}{ng^2\mu_B^2}, \quad (2.24)$$

where z is the number of nearest neighbours of an ion. By substituting λ in (2.23), the Curie temperature T_C can be written in terms of the exchange constant J :

$$T_C = \frac{2zJ}{3k_B} J(J+1). \quad (2.25)$$

2.4.2 Magnetic susceptibility

The magnetic susceptibility χ as a function of the temperature is described by the Curie-Weiss law [22]:

$$\chi = \frac{C}{T - \theta_{CW}}, \quad (2.26)$$

where θ_{CW} is the Curie–Weiss temperature and the Curie constant is $C = n \mu_{eff}^2 / 3k_B$ with n the spin concentration, $\mu_{eff} = g\mu_B \sqrt{J(J+1)}$ the effective magnetic moment, J the total quantum number, and k_B is the Boltzmann constant. This result comprises the magnetic susceptibility for a paramagnet, ferromagnet, and antiferromagnet in the mean field approximation [22]. Thus, if the material is a paramagnet, $\theta_{CW} = 0$. For a ferromagnet, $\theta_{CW} > 0$ and it is expected that $\theta_{CW} = T_C$. The behaviour of the inverse of susceptibility $1/\chi$ versus temperature is shown in figure 2.3.

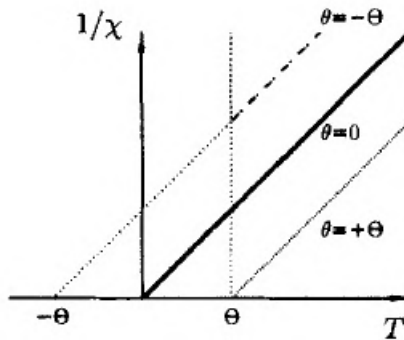


Figure 2.3: Inverse of magnetic susceptibility versus temperature graphs for $\theta_{CW} = 0$ (paramagnet), $\theta_{CW} = \Theta > 0$ (ferromagnet) and $\theta_{CW} = \Theta < 0$ (antiferromagnet). Figure taken from [22].

From (2.26) the inverse magnetic susceptibility is:

$$\chi^{-1} = \frac{T}{C} - \frac{\theta_{CW}}{C} \quad (2.27)$$

and

$$\frac{\theta_{CW}}{C} = \frac{3k_B \theta_{CW}}{n g^2 \mu_B^2 J(J+1)}. \quad (2.28)$$

2.5 Geometrically frustrated magnetism

Geometric frustration is present in systems with competing interactions among the components. It is defined as a system's inability to minimize its energy because of the spatial arrangement of the components [3]. This phenomenon is the core for exotic magnetic phenomena present in the pyrochlores. In many magnetic spin systems, nearest-neighbour Heisenberg exchange interaction dominates. For a simple linear chain, minimising the nearest-neighbour exchange interaction (antiferromagnetic or ferromagnetic) specifies a

unique ground state. However, novel magnetic ground states arise when those interactions compete in more complex lattices. The inability of frustrated systems to satisfy all pairs of interactions leads to an extensive degeneracy [27].

The canonical example of a geometrically frustrated lattice is the equilateral triangle in which the spins lie at the vertices as shown in figure 2.4. For Ising spins, interacting via nearest-neighbour antiferromagnetic exchange we see that it is impossible for the three spins to satisfy each bond simultaneously. This is because once two of the spins are antialigned to satisfy their antiferromagnetic interaction, the third one can no longer point in a direction opposite to both other spins. Also, the lowest energy state of these three spins is not unique, but six equal energy states exist. If we consider the tetrahedron as shown in figure 2.4, it can be seen that if the bondings are antiferromagnetic the same situation arises as all the pairwise interactions cannot be simultaneously satisfied.

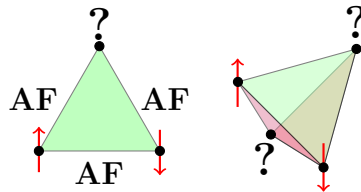


Figure 2.4: Spins with antiferromagnetic exchange arranged on a triangle or tetrahedron are geometrically frustrated.

Figure 2.5 shows some examples of geometrically frustrated lattices that are based on the canonical equilateral triangle, which include the edge shared triangular lattice (a), and the corner shared triangular lattice known as Kagomé (b).

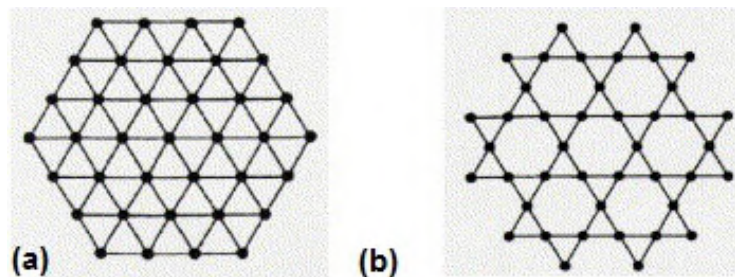


Figure 2.5: Geometrically frustrated lattices: edge-sharing triangular (a), and corner-sharing triangular or Kagomé, (b). Figure taken from [28].

Experimentally, we can identify geometrically frustrated magnets because their magnetic susceptibility has a characteristic behaviour. In this way, the inverse susceptibility

χ^{-1} follows the usual Curie–Weiss law down to temperatures well below the expected transition temperature θ_{CW} , and at some low temperature $T' \ll \theta_{\text{CW}}$ the values of χ^{-1} exhibit a substantial deviations from the linear behaviour. This denotes a transition to a state that depends of the material which could be ordered or glassy [1]. Figure 2.6 displays the temperature dependence of χ^{-1} for an antiferromagnet, a ferromagnet and a frustrated magnet. The level of frustration of is defined as the ratio $f' \equiv |\theta_{\text{CW}}|/T'$ between the Curie–Weiss temperature and the transition temperature. Large values of f' in magnetic systems are a signature of frustration [3].

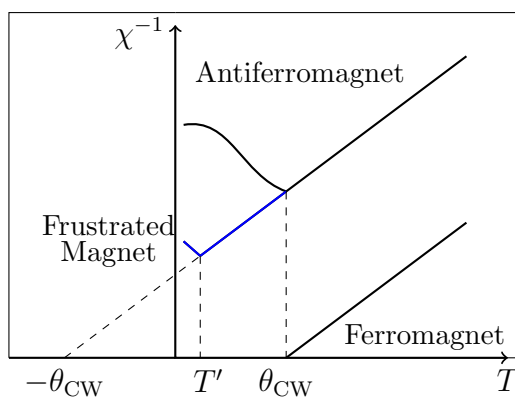


Figure 2.6: Characteristic behaviour of $\chi^{-1}(T)$ for an antiferromagnet, a ferromagnet and a geometrically frustrated magnet (blue line).

2.6 Geometrically frustrated lattices

In this section we describe the pyrochlore structure, which is a lattice subject to geometric frustration. Materials with this geometry have a general formula $R_2M_2O_7$, where R is a trivalent rare earth, R^{3+} , which includes the rare earth (Gd, Tb, Dy, Ho, Er, Yb), and M is either a transition metal or a p-block metal ion (Ti, Sn, Mn, Mo, Pb) with valence M^{4+} . Pyrochlores $R_2M_2O_7$ are oxides that crystallize in the space group $Fd\bar{3}m$. The standard method to study the crystal structure of pyrochlores is to formulate them as $R_2M_2O_6O'$ and to place the M ion at $16c$, R at $16d$, O at $48f$ and O' at $8b$ [2].

Both the R site and the M site, independently, reside on a network of corner-sharing tetrahedra, as shown in the left side of figure 2.7. Also, the two pyrochlore lattices of the cations R^{3+} and M^{4+} are displaced from each other by a translation along the cubic diagonal $[111]$. From figure 2.7, there are two types of tetrahedra in the pyrochlores, which

are labeled as the down tetrahedra and the up tetrahedra. For the rare earth pyrochlores the length of a unit cell is approximately $a_0 \approx 10 \text{ \AA}$. From the perspective of chemical bonding, the pyrochlore structure can be described as an ordered defect fluorite (CaF_2).

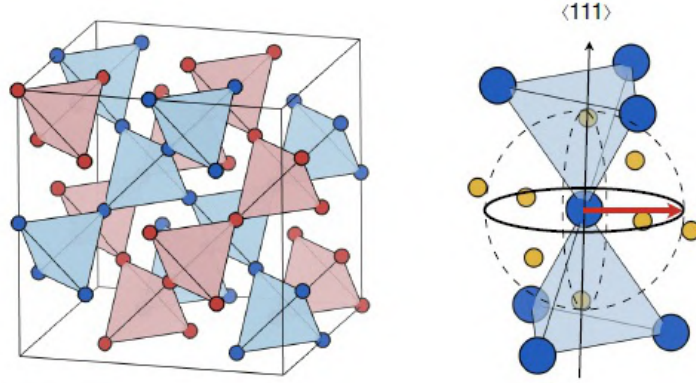


Figure 2.7: *Left:* The R (blue) and M (red) sites of the pyrochlore lattice $R_2M_2O_7$. *Right:* The R site is surrounded by eight oxygen anions (yellow). Spin (red arrow) with XY anisotropy are confined in the plane perpendicular to their local $[111]$ axis. Figures taken from [29].

The disordered fluorite lattice is also subject to geometrical frustration. This structure is found for example in zirconates $R_2Zr_2O_7$ where R/M site mixing is observed [2], as shown in figure 2.8. The disordered-fluorite structure can be described by a conversion from the pyrochlore lattice. Here, the cations R and M lying on two crystallographic different sites of the pyrochlore ($16d$ and $16c$) become disordered and equally distributed on the single $4a$ site of the fluorite structure. Also, the oxygen anions on the $48f$ and $8b$ sites of the pyrochlore shift to occupy a higher symmetry position on the $4a$ of the fluorite. This oxygen $4a$ site is $7/8$ occupied. The oxygen coordination around the cations is changed from eight and six for the R and M sites, respectively, in the pyrochlore to an oxygen coordination of seven for the disordered cations in the fluorite lattice.

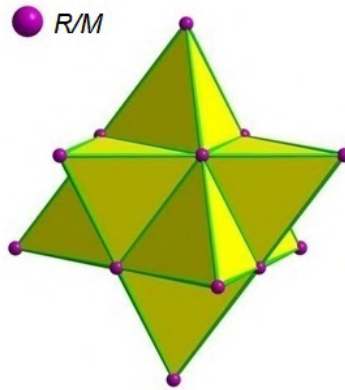


Figure 2.8: Fluorite structure showing the mixing of the R and M cations. Figure from [30].

2.7 Magnetic ground states in pyrochlores

Compounds with the pyrochlore structure studied before could enter in the magnetic phases of long-range order, spin ice, spin liquids or spin glass [2]. In order to understand compounds with similar compositions $R_2M_2O_7$ to the pyrochlores and same rare-earth magnetic ion, we will review a few results of the literature relevant to this thesis. First, we discuss about the long-range XY ordering and proposed magnetic structures in $\text{Er}_2\text{Ti}_2\text{O}_7$ and $\text{Er}_2\text{Sn}_2\text{O}_7$, next we move on to the spin-ice phases in $\text{Dy}_2\text{Ti}_2\text{O}_7$ and $\text{Ho}_2\text{Ti}_2\text{O}_7$, then we study results of the spin liquid $\text{Tb}_2\text{Ti}_2\text{O}_7$, and finally present the spin-glass phase.

2.7.1 $\text{Er}_2\text{Ti}_2\text{O}_7$ and $\text{Er}_2\text{Sn}_2\text{O}_7$

Since a decade, extensive research about the magnetic structures in the XY pyrochlores has been considered with much interest. Here, the magnetic cation Er^{3+} is proposed to exhibit XY anisotropy in which the spins are constrained to lie in the plane perpendicular to their local [111] axis [20], as shown in the right side of figure 2.7. Specific heat data shows that $\text{Er}_2\text{Ti}_2\text{O}_7$ undergoes a phase transition towards an antiferromagnetic non collinear phase at T_N 1.2 K [31], as shown in figure 2.9. The magnetic structure is described by the ψ_2 phase [20], shown in the left side of figure 2.10. In $\text{Er}_2\text{Ti}_2\text{O}_7$, there is a difference of ~ 80 K between the ground states and their first excited crystal state by [29]. Then, the entropy variation is expected to be for an isolated doublet state $R \ln 2$ [31].

The role of disorder in $\text{Er}_2\text{Ti}_2\text{O}_7$ has been studied by magnetic dilution of the erbium sublattice by yttrium [32]. In $\text{Er}_{2-x}\text{Y}_x\text{Ti}_2\text{O}_7$ a crossover of the state ψ_2 and an additional

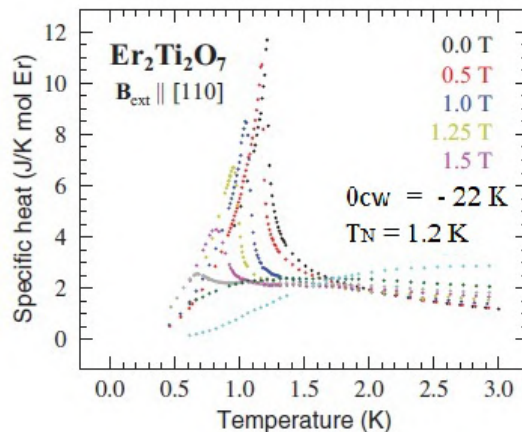


Figure 2.9: Specific heat versus temperature of $\text{Er}_2\text{Ti}_2\text{O}_7$ for different external fields. The transition peak vanishes for fields above 1.7 T. Figure taken from [31].

magnetic structure was identified [32]. In XY pyrochlores it is also proposed that the introduction of large levels of random disorder induce spin-glass domains [33]. The non-magnetic dilution of the Ti sublattice on $\text{Er}_2\text{Ti}_2\text{O}_7$ has been studied by our group in [13]. Here, results obtained from specific-heat experiments for the $\text{Er}_2\text{Ti}_{2-x}\text{Sn}_x\text{O}_7$ series under zero magnetic field were reported. All compositions present clear transition peaks associated with long-range magnetic ordering at temperatures T_N below 1 K. The long-range ordering and the magnetic ground states were confirmed by neutron studies [13]. Besides temperature, other factor as pressure, magnetic field, or doping level can constraint the order transition, and then a quantum phase transition can occur even at $T = 0$. The presence of a quantum critical point around the composition $x = 1.7$ is suggested in [13] but more experiments are required.

The compound $\text{Er}_2\text{Sn}_2\text{O}_7$ seems to belong to the family of the XY pyrochlores. As reported by neutron diffraction experiments at very low temperatures ≈ 68 mK, it enters to an antiferromagnetic Palmer-Chalker (PC) state [13,14], which is in the boundary with the magnetic phase ψ_2 of $\text{Er}_2\text{Ti}_2\text{O}_7$. $\text{Er}_2\text{Sn}_2\text{O}_7$ has an ordering temperature close to 100 mK, as reported by ac magnetic susceptibility and specific heat measurements [13,14]. The Palmer-Chalker state embraces the problem of the pyrochlore antiferromagnet including dipole-dipole interactions [15]. For spins on a pyrochlore lattice is shown in the right side of figure 2.10. Here, all the spins lie on a plane, and form pairs of antiparallel spins that are parallel to the opposite edge of the tetrahedron they belong to [15]. The ground state for the full pyrochlore lattice is a periodic repetition of that for a pair of tetrahedra.

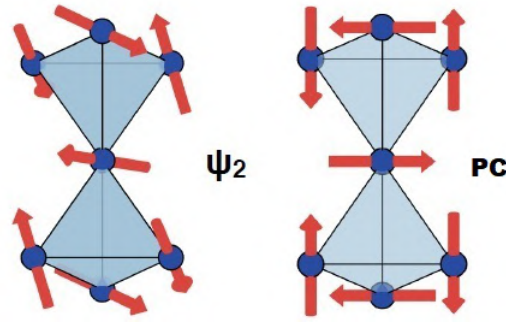


Figure 2.10: *Left*: Antiferromagnetic ψ_2 phase of $\text{Er}_2\text{Ti}_2\text{O}_7$. *Right*: The Palmer–Chalker state for $\text{Er}_2\text{Sn}_2\text{O}_7$. Figure taken from [29].

2.7.2 $\text{Dy}_2\text{Ti}_2\text{O}_7$ and $\text{Ho}_2\text{Ti}_2\text{O}_7$

The spin–ice state has been studied extensively in the rare earth pyrochlore $\text{Dy}_2\text{Ti}_2\text{O}_7$, as well in $\text{Ho}_2\text{Ti}_2\text{O}_7$. In these spin ices, the lattice geometry leads to frustration of ferromagnetic and dipolar interactions [8]. The single–ion electronic ground states of Dy^{3+} and Ho^{3+} are described by the terms ${}^6\text{H}_{15/2}$ and ${}^5\text{I}_8$, respectively. Because of the strong crystal field acting on these cations it stabilises a ground–state doublet of states [34], giving rise to a classical Ising spin with easy–axis along the local $\langle 111 \rangle$ direction [2, 28]. With this constraint on a tetrahedron, a spin can only point “in” toward the centre of the tetrahedron, or point “out” of the tetrahedron. Regarding the problem of the ground state, it was discussed that this ground state or spin configuration could be mapped onto the problem of the proton (hydrogen) positions in water ice studied by Pauling [35]. Thus, the spin configuration; minimizing the dipole and ferromagnetic exchange interactions, is “two spins in, two spins out” called the ground state of spin ice [36]. The spin–ice rule is illustrated on the left side of figure 2.11.

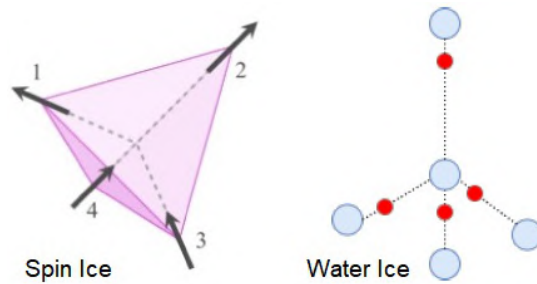


Figure 2.11: Ising spins decorating the vertices of a tetrahedron with the ice rule, oriented along their local easy–axis $\langle 111 \rangle$, and the analogy with the arrangement of protons (red circles) about oxygen (blue circles) in water ice. Figure adapted from [37].

Figure 2.11 displays how the spins with local $\langle 111 \rangle$ direction pointing inside (outside) the tetrahedron correspond to short covalent bonds (long H-bond) for water ice [37]. Pauling showed that for water ice there is a large degeneracy of the ground state, and there is therefore an extensive or residual entropy of the ground state. The value of this residual entropy was calculated by Pauling as $S_0 = \frac{R}{2} \ln(\frac{3}{2})$ [35]. The first experimental verification of the spin ice in $\text{Dy}_2\text{Ti}_2\text{O}_7$ was provided by Ramirez *et al.* in [7]. They observed from the electronic or magnetic specific heat $C_m(T)$ shown in figure 2.12(a) that the residual entropy in $\text{Dy}_2\text{Ti}_2\text{O}_7$ approached the Pauling value for water ice [7]. The entropy removed $\delta S_{1,2}$ upon cooling between temperatures T_1 and T_2 can be determined from the specific heat measurements using the thermodynamic relationship:

$$\delta S_{1,2} \equiv \int_{T_1}^{T_2} \frac{C(T)}{T} dT. \quad (2.29)$$

The entropy $S = k_B \ln(\Omega)$ for a magnetic system of N Ising spins (two spin orientations) is determined from its total number of microstates $\Omega = 2^N$, so the expected entropy is $S = Nk_B \ln 2$. Then, the total entropy per mol is $R \ln 2$. Figure 2.12(b) shows that the entropy recovered at 10 K is $3.9 \text{ J.K}^{-1}.\text{mol}^{-1}$, a value that is less than the expected $R \ln 2 = 5.76 \text{ J.K}^{-1}.\text{mol}^{-1}$. The difference of entropies, $1.86 \text{ J.K}^{-1}.\text{mol}^{-1}$, is very close to Pauling's estimate for the residual extensive entropy of water ice, $S_0 = \frac{R}{2} \ln(\frac{3}{2}) = 1.68 \text{ J.K}^{-1}.\text{mol}^{-1}$, thus with this result Ramirez *et al.* proved that $\text{Dy}_2\text{Ti}_2\text{O}_7$ carries an extensive entropy close to S_0 and obeys the ice rules [7].

Spin ices $\text{Dy}_2\text{Ti}_2\text{O}_7$ and $\text{Ho}_2\text{Ti}_2\text{O}_7$, with ions Dy^{3+} and Ho^{3+} , carries a sizeable magnetic moment $\mu \approx 10 \mu_B$ which leads to dipolar interactions that are not negligible [2,37]. For both ions the dipolar interactions are on the same energy scale as the exchange interaction [2]. The minimal model of Hamiltonian for the dipole spin ice [8], which includes the terms of nearest-neighbour exchange and magnetic dipole interactions, is

$$\mathcal{H} = -J \sum_{\langle ij \rangle} \mathbf{S}_i \cdot \mathbf{S}_j + D r_{\text{nn}}^3 \sum_{i>j} \left[\frac{\mathbf{S}_i \cdot \mathbf{S}_j}{|\mathbf{r}_{ij}|^3} - \frac{3(\mathbf{S}_i \cdot \mathbf{r}_{ij})(\mathbf{S}_j \cdot \mathbf{r}_{ij})}{|\mathbf{r}_{ij}|^5} \right], \quad (2.30)$$

where J , D and $r_{\text{nn}} \approx 3.5 \text{ \AA}$ are, respectively, the antiferromagnetic exchange coupling, the dipole-dipole coupling and the nearest neighbour distance between rare earth ions, which has been shown to provide a comprehensive quantitative description of spin ice materials [8].

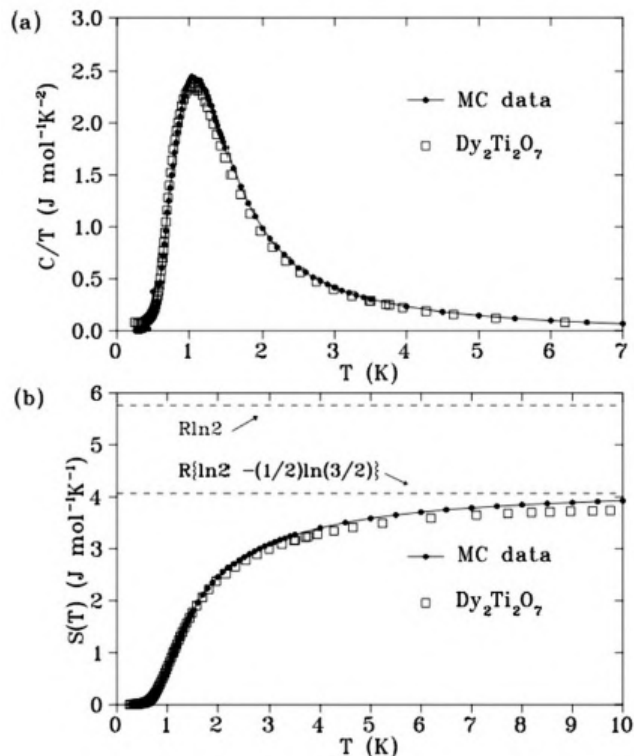


Figure 2.12: $\text{Dy}_2\text{Ti}_2\text{O}_7$: (a) Specific heat and (b) entropy as a function of the temperature reported by [7]. The residual entropy of $\text{Dy}_2\text{Ti}_2\text{O}_7$, $1.86 \text{ J.K}^{-1}.\text{mol}^{-1}$, is in agreement with Pauling’s entropy, $\frac{R}{2} \ln(\frac{3}{2}) = 1.68 \text{ J.K}^{-1}.\text{mol}^{-1}$ [7]. (a) and (b) also show a comparison with Monte Carlo simulations (MC data) of [8]. This figure was taken from [7].

As reported in [38, 39], measurements of the ac magnetic susceptibility versus temperature of $\text{Dy}_2\text{Ti}_2\text{O}_7$ exhibit two maxima in ac susceptibility, at 2.5 K and 19 K. The maximum at 2.5 K is related to the developing of the spin ice [38]. It was also observed that the maximum at 19 K possesses a frequency dependence related to a freezing of the system [38, 39].

2.7.3 $\text{Tb}_2\text{Ti}_2\text{O}_7$

In the family of pyrochlore compounds, some of them exhibit a more dynamic magnetic behaviour named spin liquid. Their existence in these materials are favoured by frustrated interaction for which there is a large ground state degeneracy. The spin-liquid phase is known for having spins that continue to fluctuate and evade order even at the lowest temperature observed [40], resembling the constant motion of molecules within a liquid. Such a spin liquid is an unusual phenomenon since it has a non-magnetic ground state,

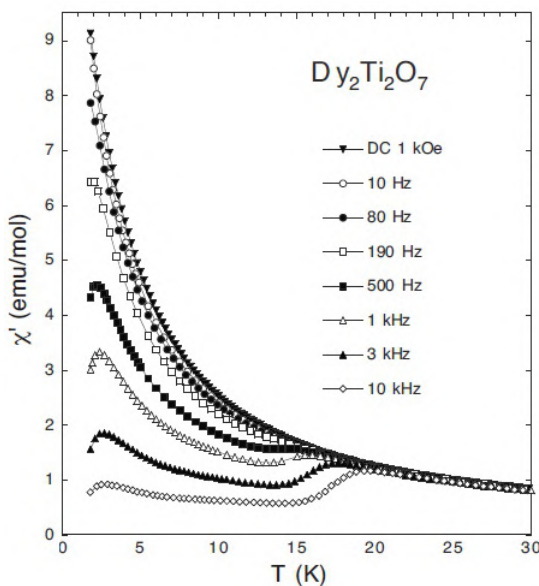


Figure 2.13: ac susceptibility versus temperature at different frequencies. Figure from [38].

even though of their well-defined local magnetic moments [40]. This highly correlated state was first proposed by Anderson in 1973 [41] and since then their theoretical picture is still an open discussion.

One frustrated magnet which stands out among pyrochlore oxides is $\text{Tb}_2\text{Ti}_2\text{O}_7$. The vast interest in this material lies in that the Tb^{3+} spins remains dynamic without developing long-range order to temperatures as low as 50 mK. This occurs despite of its antiferromagnetic Curie-Weiss temperature $\Theta_{\text{CW}} = -19$ K [5,21], and strong magnetic correlations present at low temperatures, as reported by neutron studies [42]. It is proposed to entering into a classical spin-liquid state. The magnetic Tb^{3+} in $\text{Tb}_2\text{Ti}_2\text{O}_7$ possesses a strong Ising-like CEF anisotropy [21] analogous to one along the local $\langle 111 \rangle$ axes reported for the spin ices $\text{Dy}_2\text{Ti}_2\text{O}_7$ [7, 43] and $\text{Ho}_2\text{Ti}_2\text{O}_7$ [44, 45]. For $\text{Tb}_2\text{Ti}_2\text{O}_7$ the energy of its CEF states lies in orders of magnitude many hundred times smaller when compared to spin ices, and then the doublet ground state permits an admixing with excited CEF states. Even though the Tb^{3+} ground state is Ising-like, fluctuations of the ground-state moment appear after spin interactions are taken into account [46]. $\text{Tb}_2\text{Ti}_2\text{O}_7$ is also proposed to be a kind of a quantum spin-ice system where the spin-ice-like correlations remain hidden down to 0.5 K [27, 46]. Inelastic neutron studies reveal magnetoelastic modes in $\text{Tb}_2\text{Ti}_2\text{O}_7$ suggesting a Coulomb phase with bosonic excitations [47]. Experimental evidence for spin-lattice coupling has also been reported by studies that found magnetic long-range order in $\text{Tb}_2\text{Ti}_2\text{O}_7$ driven by pressure and structural distortions induced by

field [48, 49]. ac and dc susceptibility measurements in zero field showed spin-glass state signatures close to 300 mK [6, 50]. In presence of magnetic fields, ac susceptibility (χ_{ac}) experiments by Ueland et al. revealed frequency dependent peaks on the real and imaginary parts of χ_{ac} indicating unexpected slow spin relaxations [51]. Measurements of specific heat reveal a high sample dependence and notorious changes in different crystals which display different thermal data of their broad peaks below 1 K, as shown in figure 2.14.

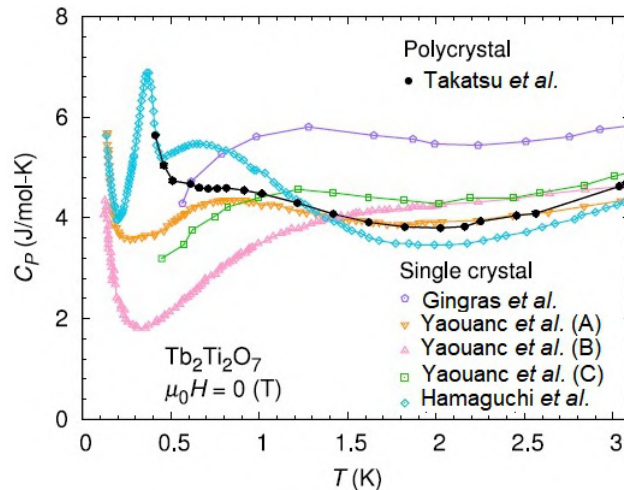


Figure 2.14: Specific heat versus temperature for different samples of $\text{Tb}_2\text{Ti}_2\text{O}_7$. Figure from [52] which displays data from [21], [53] and [54].

2.7.4 Spin Glasses

The competing interactions in frustrated, the magnetic anisotropy, and the degree of sensitivity to dilute disorder are responsible for selecting the ground states of these materials. The mentioned mechanisms can work together to develop a ground state or a set of states which could or could not result in long-range ordered states. In the framework of non-ordered states, the spin glass is a state with their magnetic moments frozen in random configurations [55]. The configuration of a spin glass consists of spins frozen under a established rule from a dynamic state at freezing temperature T' . A given ground state is determined by the experimental conditions from a large set of frozen states. Experimentally observed transitions to the spin-glass state are characterized by some signatures as a diverging non-linear susceptibility, the frequency dependence of the ac susceptibility or the line shape in muon spin relaxation [2, 55]. An example of spin glass in the pyrochlore lattice is $\text{Y}_2\text{Mo}_2\text{O}_7$ in which the magnetic ion is the transition metal Mo^{4+} [2, 56]. Neu-

neutron scattering experiments evidence a broad peak at 1.8 K which suggest short-range correlations for four different sublattices in the structure [56], as shown in figure 2.15.

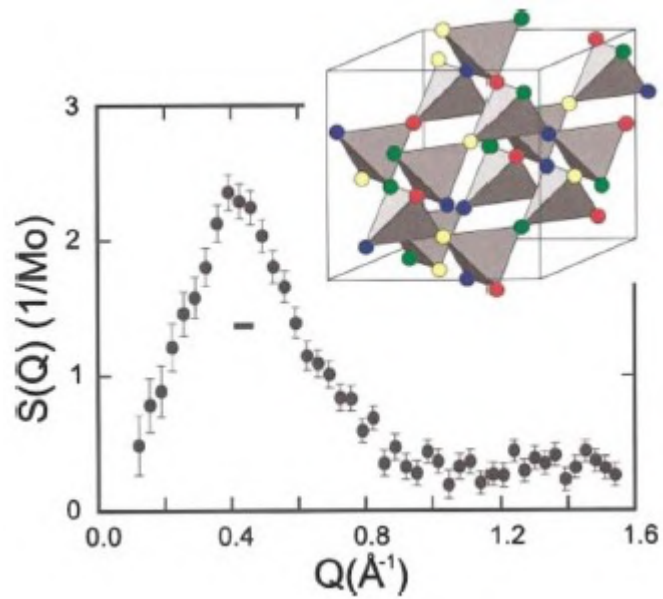


Figure 2.15: Neutron scattering of $\text{Y}_2\text{Mo}_2\text{O}_7$ at 1.8 K. Inset: the four sublattices correspond to different colors in the vertices of the tetrahedra. Figure from [56].

Experimental Methods

In this chapter we describe the growth of our samples using two synthesis methods. Next, we review the basics of x-ray and neutron diffraction techniques employed to determine the crystalline and magnetic structure of our samples. Finally, we describe the operation of the experiments for magnetic and thermal studies which were carried out on an adiabatic demagnetization refrigerator, a home-made susceptometer, a superconducting quantum interference device, and a calorimeter Physical Property Measurement System.

3.1 Sample preparation

For the preparation of our samples two different synthesis route have been used. The $\text{Er}_2\text{Ti}_{2-x}\text{Sn}_x\text{O}_7$ ($x = 0 - 2$) series were prepared by solid-state reaction at high temperature, and the zirconates $\text{Dy}_2\text{Zr}_2\text{O}_7$, $\text{Ho}_2\text{Zr}_2\text{O}_7$, and $\text{Tb}_2\text{Zr}_2\text{O}_7$ were prepared by the soft-chemistry sol-gel method. All samples used for experiments in this work are polycrystalline powder samples.

3.1.1 Solid-state reaction

A method widely used to prepare polycrystalline powder erbium samples $\text{Er}_2\text{Ti}_2\text{O}_7$ and $\text{Er}_2\text{Sn}_2\text{O}_7$ is the solid-state reaction method [57, 58]. Using this standard technique, a single phase polycrystalline sample of $\text{Er}_2\text{Ti}_2\text{O}_7$ is prepared by mixing and grinding stoichiometric ratios of the oxides Er_2O_3 and TiO_2 . The mixture of the oxides is heated several times up to 1350°C with intermediate grindings for more than 24 hours, as detailed in Ref. [57]. The set of different compositions ($x = 0.5, 1, 1.5, 1.7, 1.8, 2$) of the

$\text{Er}_2\text{Ti}_{2-x}\text{Sn}_x\text{O}_7$ series were made by the same technique, but reacting stoichiometric amounts of Er_2O_3 , TiO_2 , and SnO_2 . $\text{Er}_2\text{Ti}_{2-x}\text{Sn}_x\text{O}_7$ samples used in this thesis were prepared by Prof. Jorge Lago from País Vasco University.

3.1.2 Sol–gel method

To produce polycrystalline powder samples of $\text{Dy}_2\text{Zr}_2\text{O}_7$, $\text{Ho}_2\text{Zr}_2\text{O}_7$, and $\text{Tb}_2\text{Zr}_2\text{O}_7$ we use an alternative process named the sol–gel method. This technique appears to be very promising since it provides a simpler route to synthesize oxides at lower temperatures and in shorter times than usual solid–state reactions. The sol–gel method outstands by the advantage of producing high purity and homogenization of the powder sample, achieved by an excellent molecular level mixing [60–62]. Materials properties as hardness, porosity, and a great control over particles morphology and size can be produced by this process [62].

In this work the starting materials used for the synthesis were: Dy_2O_3 , Ho_2O_3 and Tb_4O_7 . The rare–earth (R) oxide and tetrabutyl zirconate, $\text{C}_{16}\text{H}_{36}\text{O}_4\text{Zr}$, were employed as precursors of two dissolutions of the cations R^{3+} and Zr^{4+} , respectively. For the first one, a stoichiometric amount of the rare–earth powder was dissolved into a non–stoichiometric quantity of nitric acid HNO_3 (65%, Sigma–Aldrich) with some drops of water, and with a molar rate of $R/\text{Zr} = 1$. The excessive HNO_3 was evaporated by slow heating and stirring at 80°C . For the second dissolution, powder citric acid $\text{C}_6\text{H}_8\text{O}_7$ (Merck) was dissolved into ethanol $\text{C}_2\text{H}_5\text{OH}$ (Sigma–Aldrich) with a stoichiometric amount of $\text{C}_{16}\text{H}_{36}\text{O}_4\text{Zr}$, maintaining the magnetic stirring vigorously. The molar quantity of citric acid was 2.5 times the mol of the R ion and Zr. The mixture of both dissolutions was maintained in magnetic stirring for 12 hours at 80°C until it changed into a gel (right panel of 3.1). Finally, the resulting gel was calcinated at 950°C for 24 hours and turn into a white powder (left panel of 3.1), as detailed in [60–63]. We also prepared the isotopically enriched compound $^{162}\text{Dy}_2\text{Zr}_2\text{O}_7$ which is suited for our neutron scattering experiments due to the small absorption cross section of ^{162}Dy . The same method was employed for preparing $\text{Dy}_2\text{Ti}_2\text{O}_7$, $\text{Ho}_2\text{Ti}_2\text{O}_7$, and the nonmagnetics $\text{Lu}_2\text{Ti}_2\text{O}_7$ and $\text{Lu}_2\text{Zr}_2\text{O}_7$ used for specific–heat analysis. $\text{Dy}_2\text{Zr}_2\text{O}_7$, $^{162}\text{Dy}_2\text{Zr}_2\text{O}_7$, $\text{Dy}_2\text{Ti}_2\text{O}_7$, $\text{Ho}_2\text{Ti}_2\text{O}_7$, $\text{Lu}_2\text{Ti}_2\text{O}_7$ and $\text{Lu}_2\text{Zr}_2\text{O}_7$ samples were prepared in collaboration with Prof. Flavio Vichi and Dr. Marina Leite from the Institute of Chemistry, USP. $\text{Ho}_2\text{Zr}_2\text{O}_7$ and $\text{Tb}_2\text{Zr}_2\text{O}_7$ samples were prepared by me and

undergraduate student Pedro Oliviera at the laboratory of our group.



Figure 3.1: *Right:* Dried gel of $\text{Ho}_2\text{Zr}_2\text{O}_7$ after magnetic stirring at 80°C . *Left:* White powder of $\text{Ho}_2\text{Zr}_2\text{O}_7$ after heat treatment of 950°C . Photo credits to P. Oliviera.

3.2 X-ray diffraction

Diffraction of photons, neutrons and electrons are the most powerful methods for evaluating crystal and magnetic structures. Diffraction occurs when an incident radiation is scattered by the periodic arrangement of atoms or magnetic moments in the solid, producing constructive interference at specific angles without changing its wavelength. For photons, the varying electric field accelerates the electrons in the atoms which then radiate photons of the same wavelength. The x-ray wavelength (0.1 to 100 Å) is similar to typical atomic distances, being an excellent probe of the microscopic structure [24].

Bragg's law is fundamental to the physics of diffraction. For crystallographic planes of atoms shined by an incoming beam, Bragg's law establishes the relationship between the wavelength of the beams and the differences of the pathways of the beams:

$$n\lambda = 2d \sin\theta, \quad (3.1)$$

where n is an integer, λ is the wavelength of the radiation, d is the spacing between two planes, and θ is the scattered angle, as shown in figure 3.2. Bragg peaks occurs only when the difference in path length of the x-rays is an integer number of wavelengths combining constructively.

Powder x-ray diffraction is an extremely functional technique used in this thesis to assess the phase, crystallinity, composition of our compounds, and to perform a detailed

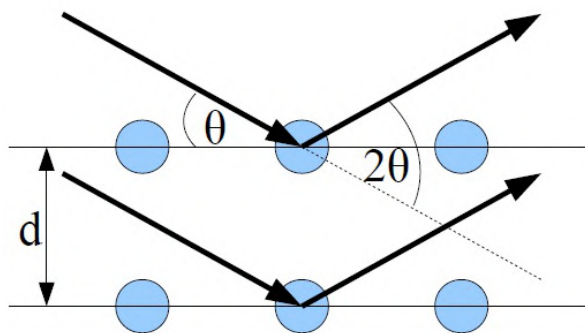


Figure 3.2: Bragg diffraction representation showing the incoming x-ray scattering from the atoms within the crystallographic planes. The path length difference is $2d \sin\theta$.

structural analysis. In this technique a single wavelength of incident x-rays is employed, and the diffraction angle 2θ is varied. If the sample is in crystal form, it is ground into a powder, composed of individual crystallites randomly oriented. Then, the diffraction pattern is averaged over all crystallographic directions. Figure 3.3 shows a schema of the diffractometer with the x-ray tube as the source of the beam, and the detector of the diffracted x-rays. Figure 3.3 also displays the Bragg-Brentano geometry for powder-diffraction experiments, which is one of the most common systems used [65]. The incident and diffracted beams are focussed at fixed distances from the sample position, and the diffraction angle 2θ is defined between the incident beam and the detector [65]. The incident angle θ is defined between the x-ray source and the sample, being the half of the diffraction angle 2θ . X-ray powder-diffraction experiments were performed using a Bruker AXS D8 Discover diffractometer from the Laboratory of Crystallography of the Physics Institute, USP. The Bragg-Brentano geometry and copper $K\alpha_1$ radiation (1.5406 Å) were used. In next Chapters we present the x-ray patterns of our samples and their respective structural analysis.

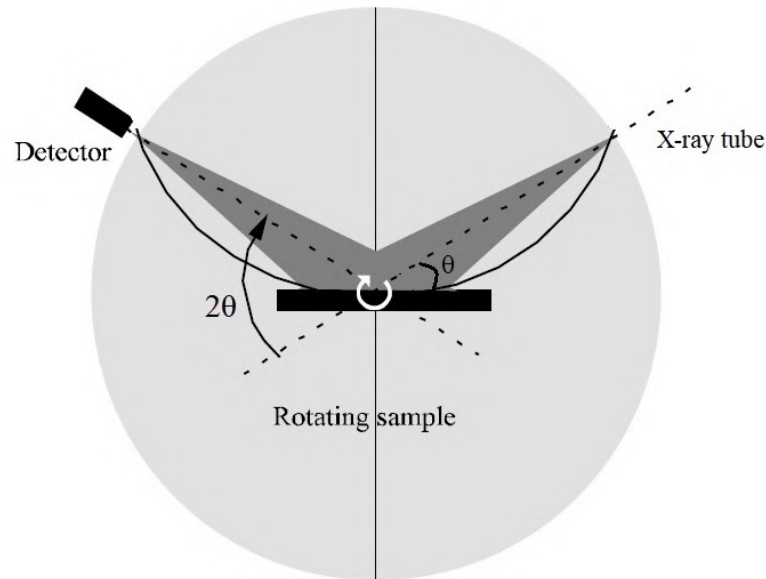


Figure 3.3: Schematic image of the Bragg–Brentano diffractometer. The detector in the 2θ position measures the diffraction peaks of the incident angle θ . Figure modified from [65].

3.3 Neutron diffraction

X-ray and neutron diffraction work together as complementary techniques due to the different nature of the atomic scattering. In the range of the interatomic distances in solids is the de Broglie wavelength for thermal neutrons (1.8 \AA), being then suitable for probe crystalline structures. Their energy on the order of 10 meV makes them useful for determine phonons, magnons and crystal field excitations. One advantage over other scattering probes is the zero charge of the neutron which makes its interaction with matter very weak. The absence of the Coulomb interaction allows the neutron to penetrate deeply into the sample and if the neutron pass close enough to the nuclei of atoms, they interact via short-range strong forces. The neutron also carries a magnetic dipole moment of $\mu = 1.91\mu_N$, where μ_N is the nuclear magneton. Therefore it can be used to explore the crystal magnetism by interacting with its unpaired electrons through magnetic dipole forces. This way neutrons are ideal for studying the crystal and magnetic structures of materials.

In a scattering experiment, a neutron with incident momentum \mathbf{k}_i and energy E_i is scattered by the sample, leaving with final momentum \mathbf{k}_f and energy E_f . The distribution of momentum and energy of the neutrons scattered are then measured. The scattering

process is described by the momentum and energy transfer which follow as

$$\mathbf{Q} = \mathbf{k}_i - \mathbf{k}_f \quad (3.2)$$

$$\hbar\omega = E_i - E_f = \frac{\hbar^2}{2m_n}(\mathbf{k}_i^2 - \mathbf{k}_f^2) \quad (3.3)$$

where \mathbf{Q} and $\hbar\omega$ are the momentum and energy gained by the sample. If the energy transfer $\hbar\omega = 0$, the scattering is named elastic and otherwise inelastic. The fundamental quantity measured during a neutron scattering experiment is the partial differential cross section. It describes the change of the neutron-sample system from the initial state \mathbf{k}_i to the final state \mathbf{k}_f and is defined as [66]

$$\frac{d^2\sigma}{d\Omega dE} = \frac{k_f}{k_i} \left(\frac{m_n}{2\pi\hbar} \right)^2 |\langle \mathbf{k}_f | V(\mathbf{r}) | \mathbf{k}_i \rangle|^2 \delta(\hbar\omega + E_i - E_f). \quad (3.4)$$

This expression is described by the Fermi golden rule and is based on first-order perturbation theory. $V(\mathbf{r})$ is the potential of the nuclear and magnetic interactions that the neutron experiences. The scattering of both potentials are treated separately, since there are no interference terms between them.

The strong force interaction can be approximated as pointlike, and is characterized by the single parameter b named the scattering length. This parameter can be complex and its imaginary component corresponds to the absorption cross section. The potential is the given by $V(\mathbf{r}) = (2\pi/m_n) \sum_i b_i \delta(\mathbf{r} - \mathbf{r}_i)$, where \mathbf{r}_i and b_i are the position of the i nucleus in the lattice and its scattering length, respectively. Using this potential along with 3.4, the partial differential cross section becomes [66]

$$\frac{d^2\sigma_{nucl}}{d\Omega dE} = N \frac{k_f}{k_i} \frac{1}{4\pi} [\sigma_c S(\mathbf{Q}) + \sigma_i S_i(\mathbf{Q})], \quad (3.5)$$

where N is the number of nuclei and the total scattering cross section for the nucleus is separated in the coherent σ_c and incoherent σ_i parts. The incoherent scattering is due to not all nuclear scatterers are identical and arises from a random distribution of the scattering lengths from their mean value \bar{b} . σ_i is proportional to the variance of the scattering lengths present. σ_c is due to coherent scattering which is as if all the scattering lengths of the nuclei are equal to \bar{b} . It is proportional to the square of the mean scattering length $|\bar{b}|^2$. $S(\mathbf{Q})$ is the dynamic nuclear structure factor given by

$$S(\mathbf{Q}) \propto \sum_i b_i e^{-i\mathbf{Q}\cdot\mathbf{r}} \quad (3.6)$$

which is an important quantity in crystallographic studies since the intensity of the Bragg peaks or number of neutrons counted is proportional to $S(\mathbf{Q})^2$.

For the magnetic interaction involving the spin of the neutron σ , the potential term in (3.4) is substituted by $|\langle \mathbf{k}_f, \sigma_f | V(\mathbf{r}) | \mathbf{k}_i, \sigma_i \rangle|$. The magnetic potential is given by $V(\mathbf{r}) = -\gamma\mu_N\sigma\cdot\mathbf{B}(\mathbf{r})$, where \mathbf{B} is the magnetic induction. This interaction arises from the spin and orbital motion of an electron. For the elastic scattering case, the cross section becomes [66]

$$\frac{d\sigma}{d\Omega} = \left(\frac{m_n}{2\pi\hbar}\right)^2 |\langle \mathbf{k}_f, \sigma_f | V(\mathbf{r}) | \mathbf{k}_i, \sigma_i \rangle|^2. \quad (3.7)$$

Integrating over all \mathbf{r} ; with no specification of the nuclear spin σ (unpolarized neutrons), and solving for the magnetic potential returns a dependence with the sample magnetization that is perpendicular to the scattering vector \mathbf{Q} [66]

$$\langle \mathbf{k}_f | V(\mathbf{r}) | \mathbf{k}_i \rangle = \int V(\mathbf{r}) e^{i\mathbf{Q}\cdot\mathbf{r}} \cdot d\mathbf{r} = \mathbf{M}_\perp(\mathbf{Q}), \quad (3.8)$$

and by substituting in (3.7)

$$\frac{d\sigma_{mag}}{d\Omega} = \langle \mathbf{M}_\perp^*(\mathbf{Q}) \rangle \langle \mathbf{M}_\perp(\mathbf{Q}) \rangle. \quad (3.9)$$

Neutron scattering therefore probes the components of the sample magnetization \mathbf{M}_\perp that are perpendicular to the neutron's momentum transfer \mathbf{Q} . In this way the magnetic correlations are measured. The two cross sections above are summed together, and then the magnetic scattering can be isolated by a subtraction of the nuclear component. The nuclear scattering can be considered as a background and it is isolated by running experiments at a temperature above the energy scale of their magnetic correlations.

Neutrons are produced by spallation or reactor sources, and they can provide a wide range of wavelengths. In elastic diffraction experiments, the instruments are designed with a fixed momentum and the outgoing momentum is assumed to be the same. Figure 3.4 shows a diagram of a simple diffractometer. First, a polychromatic beam is guided to the instrument from the neutron source. Then, a single crystal called a monochromator is used to reflect and select the required wavelength towards the sample by satisfying the Bragg's law. Around the perimeter of a circle centred on the sample, ^3He position-sensitive detector tubes measure scattering from the sample in specific directions. These cylindrical detectors are based on ^3He since they have a large absorption cross section. By rotating the sample it is possible to map out a large region of the reciprocal space in \mathbf{Q} .

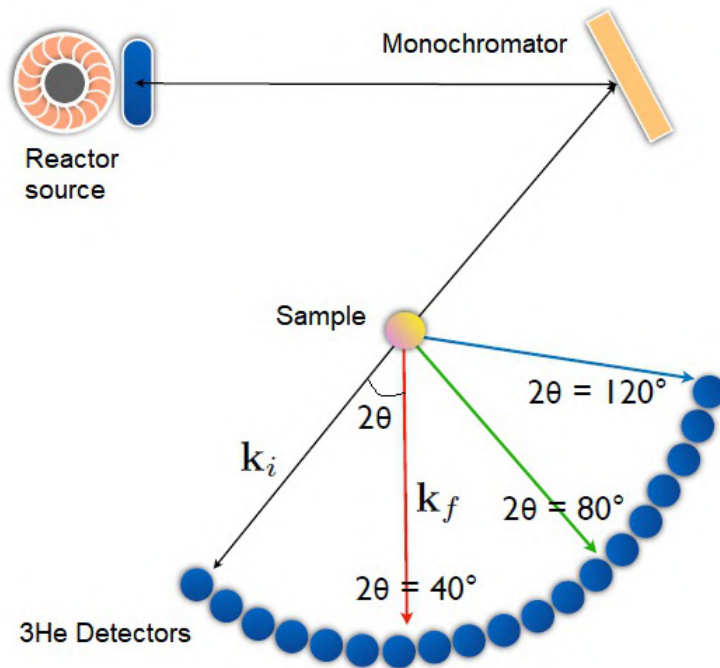


Figure 3.4: Schematic diagram of a diffractometer. Figure modified from [67].

Structural diffraction experiments on the isotopically enriched $^{162}\text{Dy}_2\text{Zr}_2\text{O}_7$ were carried out at the high-resolution ECHIDNA [68] at the Australian Nuclear Science and Technology Organization (ANSTO, Sydney). We use a germanium monochromator at 140 degrees take-off angle and the sample was placed in a vanadium can for measurements at room temperature. Magnetic diffraction studies were performed at the high-intensity neutron diffractometer WOMBAT [69] at ANSTO using 4.744 Å neutrons. We use a pyrolytic graphite monochromator at 90 degrees take-off angle [69]. The $^{162}\text{Dy}_2\text{Zr}_2\text{O}_7$ sample of 300 mg was loaded in an oxygen-free cooper container and mounted to the end of a Kelvinox dilution insert from Oxford Instruments to reach a temperature of 40 mK. In-field experiments employed a 12 T magnet by Oxford Instruments. Experiments at ANSTO were performed by Jason Gardner and Chin-Wei Wang.

3.4 Rietveld refinement

The structural analysis was conducted by the Rietveld refinement which is an excellent method to validate the structure to which a material belongs [70]. The Rietveld method is a refinement process in which an initial profile of the crystal structure is required [71]. Information of the structure and chemistry such the space group, lattice constant, atom

positions, and thermal parameters are detailed in the model. The analysis was done by using the software FULLPROF [72] together with its graphical interface WINPLOTR.

The Rietveld refinement employs an algorithm which minimizes the difference between the experimental data and a model, evaluated on a least-squares approach. In the analysis, a background can be accounted with a polynomial or by specifying a number of interpolated points. Additional parameters can also be specified including as the peak broadening, absorption, geometry, or anisotropic temperature factors. The quality of the fitting is determined by the factors χ^2 , R_{wp} and R_{exp} . χ^2 is the square ratio of R_{wp} and R_{exp} , R_{wp} is the residual taking into account weights in intensity and R_{exp} is the expected residual value. The refinement continues until convergence is reached with the value of the goodness-of-fit χ^2 approaching 1. The factors below are defined as follow:

$$R_{wp} = \left[\frac{\sum_{i=1}^n w_i (y_i - y_{c,i})^2}{\sum_{i=1}^n w_i y_i^2} \right]^{1/2} \quad (3.10)$$

$$R_{exp} = \left[\frac{n - p}{\sum_{i=1}^n w_i y_i^2} \right]^{1/2} \quad (3.11)$$

$$\chi^2 = \left(\frac{R_{wp}}{R_{exp}} \right)^2, \quad (3.12)$$

where w_i is the variance of the intensity measured y_i , $y_{c,i}$ is the calculated value of y at the i position, n is the total number of data points and p is the number of refined parameters.

Common peak-shape functions to model the intensity of the Bragg reflections include the Gaussian, Lorentzian and Pseudo-Voigt. The profile function used in this thesis is the Pseudo-Voigt $V(x)$ which is defined as the sum of a Gaussian peak $G(x)$ and a Lorentzian peak $L(x)$, weighted by a parameter η with values between 0 and 1.

$$V(x) = (1 - \eta)G(x) + \eta L(x) \quad (3.13)$$

There is a wide spectre of complicated functions that are possible, including the ones that allow for asymmetric broadening at low scattered angle. The broadening of peak reflections can be due to strain in the sample or to the crystallite size forming in the material, which can also be incorporated in the refinement model. The crystal size, D , are modelled following the Scherrer equation:

$$D = \frac{K\lambda}{\beta \cos\theta}, \quad (3.14)$$

where K is a dimensionless factor of value 0.9, λ is the wavelength, β is the full width at half maximum, and θ is the Bragg angle.

3.5 Magnetic measurements

3.5.1 Adiabatic demagnetization refrigerator

The measurements of the ac magnetic susceptibility χ_{ac} were carried using a susceptometer consisted of an adiabatic demagnetization refrigerator (ADR, Cambridge Cryogenics), inserted at a liquid–helium cryostat.

In an ac susceptometer, a modulation field $h_{ac} = h_0 \cos(\omega t)$ is produced by a coil and applied to the sample. Then, the ac magnetic susceptibility χ is measured by a secondary coil and is given by [76]

$$\chi = \frac{dM}{dh_{ac}}, \quad (3.15)$$

where M is the magnetization of the sample. The ac magnetic susceptibility is studied as a complex number and separates in two components: $\chi'_{ac} + i\chi''_{ac}$. We usually focus on the real component of the susceptibility χ'_{ac} that represents the part of χ_{ac} that is in phase with the applied ac field. The imaginary component χ''_{ac} is related to the energy losses.

The magnetic refrigerator provides a 50 mK base temperature, and it is configured to reach this temperature operating with a 9 T coil. The cooling of the ADR is due to a paramagnetic salt pill. A simple example of an ADR system consists of a paramagnet connected to the sample to be cooled and via a thermal switch to a heat sink. A simplified diagram of the ADR setup is shown in figure 3.5, which was taken from [74]. The ADR system is cyclic, and in the first part of the cycle, the paramagnetic solid is thermally linked to a 1 K bath and a magnetic field is applied to the solid. As the field is increased, the magnetic regions in the solid start to align and the paramagnet heats up. Next, the thermal switch is connected, and heat is transferred from the solid to the heat sink while the magnetic field is held constant. This reduces the temperature of the paramagnet, back to near its starting point. The thermal switch is now open, isolating the paramagnetic pill and the magnetic field is now reduced. This is the adiabatic demagnetization portion of the cycle. As the magnetic field is reduced the paramagnetic regions become more disordered and absorb entropy from the thermal vibrations resulting in a cooling of the paramagnetic material and of the object being cooled.

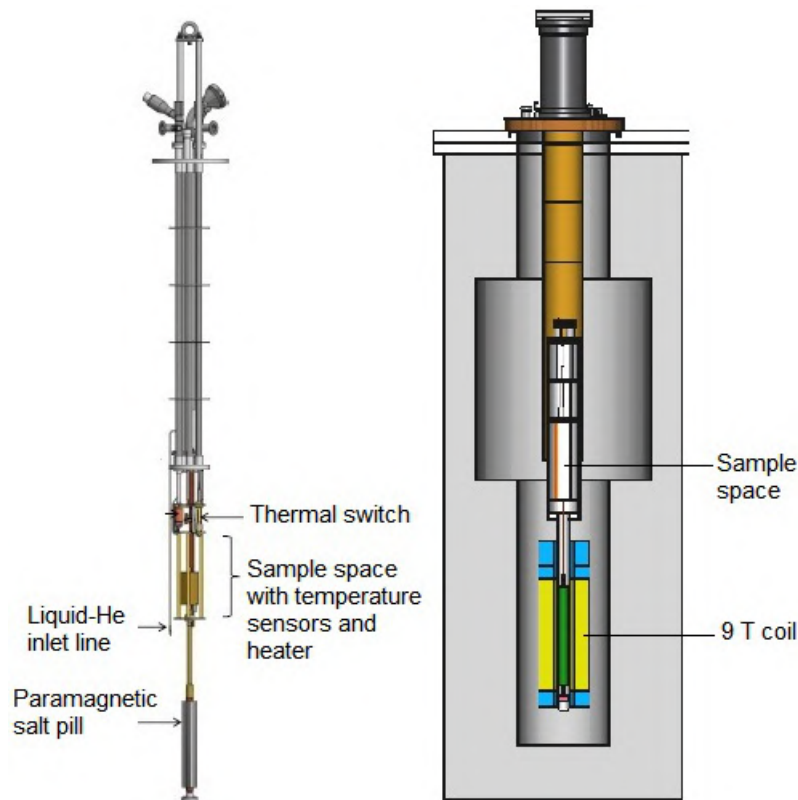


Figure 3.5: *Left*: Magnetic refrigerator. Figure taken from [74]. *Right*: Cross-section of the liquid-helium magnet cryostat with the magnetic refrigerator inserted in its operating position.

The ac susceptibility data were collected using the ADR with an amplitude and phase compensator circuit over a wide range of frequencies from 2 Hz to 10 kHz in a modulation field of 0.5 Oe.

3.5.2 Home-made ac susceptometer

The measurements of the dynamic susceptibility were also carried out at a home-made ac susceptometer. It consists of a pumped-helium (^4He or ^3He) cryostat; as seen in figure 3.6; and of a mutual inductance bridge. The ac susceptometer reaches a temperature of 1.1 K using ^4He liquid and a minimum of 0.35 K using ^3He liquid. The ac susceptometer uses pickup coils to detect changes in the magnetic flux due to the sample.

To start experiments within the pumped ^4He cryostat, it is required to cool down first the space of the superconducting coil with liquid nitrogen (77 K). When the system reaches the thermal equilibrium, the liquid nitrogen is pumped out and the helium (4.2 K) is transferred into the superconducting coil space. To cool down the sample space at

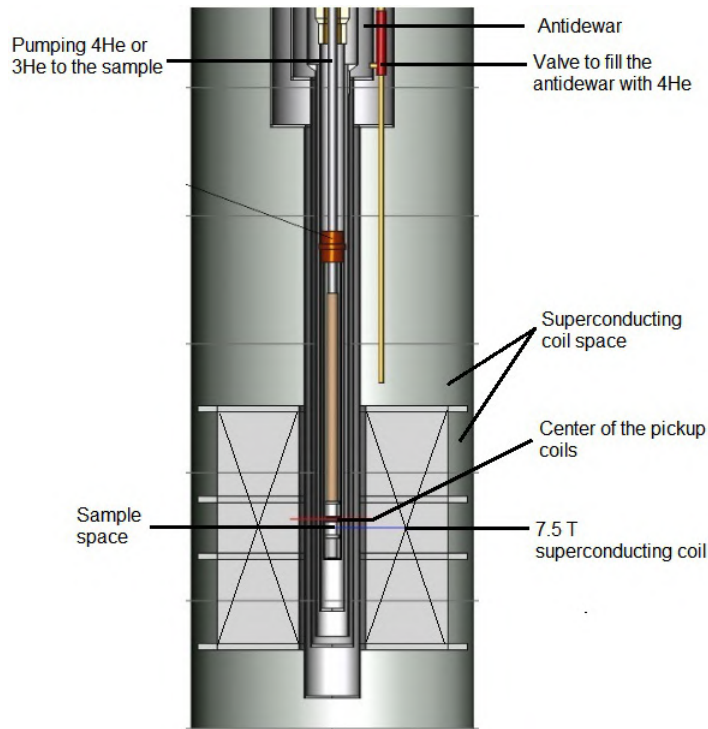


Figure 3.6: Schematic diagram of the susceptometer inside the pumped ^4He cryostat. Figure adapted from [75].

lower temperatures, ^4He is transferred to the antidewar region which allows the thermal contact with the inner chamber of the sample space. By pumping the antidewar region, the ^4He gas of the sample space is liquefied. To reach temperatures down to 4.2 K, it is used a vacuum pump in the sample space allowing a minimum temperature of 1.1 K. In the sample space we can also use ^3He liquid to measure in temperatures below 1.26 K, and with the help of a vacuum pump it reaches a minimum of 0.35 K.

We used together with the cryostat a mutual inductance bridge for determining the χ_{ac} values. The sample is placed between two coupled coils known as the primary and secondary coils. A diagram of this configuration is shown in figure 3.7. The secondary coils are two identical pickup coils positioned symmetrically inside the primary coil. Both are connected in opposition in order to cancel the voltages induced by the modulation field itself or external sources. To collect the χ_{ac} data, we used a typical setup as detailed in reference [76]. By measuring the induced voltage with a lock-in amplifier, the real and the imaginary parts of the susceptibility can be separated. The ac modulation signal produced by the primary coil is applied to the sample and the sample induces a signal on the secondary coils. The induced signal which is proportional to the susceptibility is

then measured. The magnetic susceptibility of the sample is obtained from the difference between the values of inductance of the bridge with the sample and without the sample.

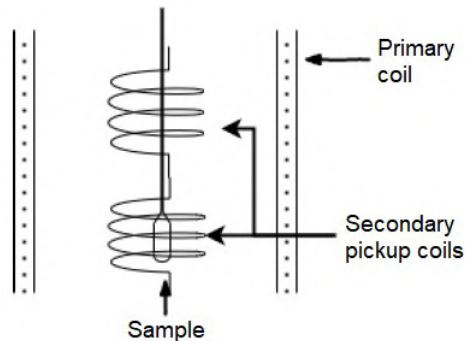


Figure 3.7: Setup configuration of the primary and secondary pickup coils.

Experiments were performed with a modulation field $h_{ac} = 1$ Oe and a drive frequency of 155 Hz. The setup of our home-made susceptometer provides a superconducting coil able to generate fields up to 7.5 T.

3.5.3 Superconducting quantum interference device

The signal induced in magnetometers is due to change of magnetic flux. Nowadays, the most sensitive instrument for measuring flux is the superconducting quantum interference device (SQUID) which is able to probe extremely low fields up to a magnitude order of 10^{-14} T [77]. SQUID devices make use of the quantisation of magnetic flux in a superconducting ring in combination with the Josephson-effect [78, 79].

The SQUID is a magnetometer that measures magnetic flux and a output voltage signal. From the output signal, the magnetic moment of a material and consequently its magnetization is determined. The SQUID consists of a superconducting ring with Josephson junctions or insulating barriers at two points of the ring, as shown in figure 3.8. The basis of its operation is described by a current I flowing through the SQUID and the Josephson Effect. This effect occurs when a current carrying Cooper pairs can tunnel through the junctions until a critical current I_c is reached. After I_c is exceeded, the SQUID permits the tunnelling of single electrons through the barriers and a output voltage U starts to appear.

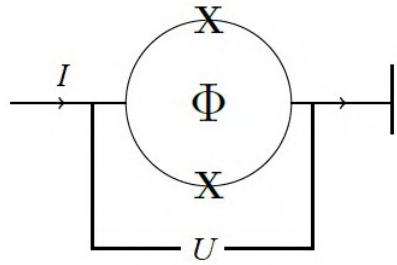


Figure 3.8: Diagram of the SQUID showing the Josephson junctions; denoted with X, and the superconducting ring. Φ is the magnetic flux, I is the current through the loop and U is the measured voltage.

The application of a magnetic flux to a SQUID can penetrate the device through its Josephson junctions. The change in the flux inside the ring (Φ) generates a measurable change in the current or output voltage through the Josephson junction. In superconducting loops, the amount of Φ is quantised to multiples of the magnetic flux quantum ϕ_0 [78]. Due to this quantisation condition, the voltage between the two junctions is a periodic function with the magnetic flux inside the loop or ϕ_0 [80].

Figure 3.9 shows a diagram for the detection of the output signal and the SQUID device. It is shown the pickup coils to detect the signal and the sample. The sample is positioned at the center of two pickup coils and then a magnetic field is applied. The external field induces a current in the pickup coils that goes through the loop which is inductively coupled to the SQUID device. On the bottom right side, it is displayed the SQUID device which works as explained above.

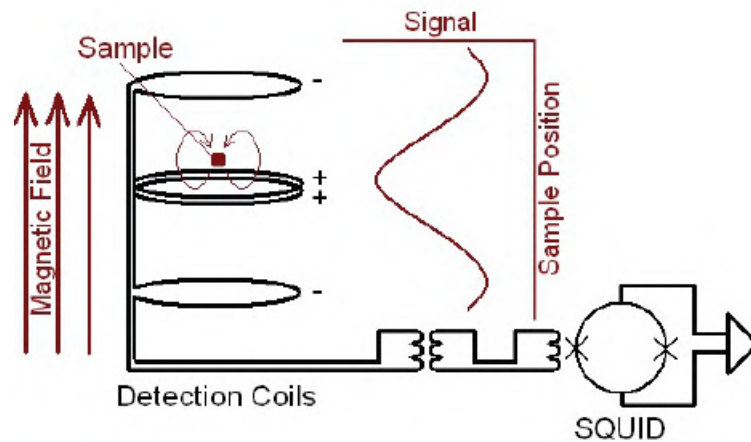


Figure 3.9: Diagram of the detection setup of the SQUID. The pickup coils, the sample, and the detection loop are shown as well. Figure adapted from [77].

Measurements of the dc magnetization were carried out on a commercial MPMS XL7 SQUID magnetometer of the Quantum Design, operating at a cryostat of ^4He in the interval of temperatures from 2 to 300 K and static external fields up to 7 T.

3.6 Thermal measurements

3.6.1 Physical Property Measurement System

The specific heat experiments were conducted on the calorimeter Physical Property Measurement System (PPMS) from Quantum Design. The calorimeter is a closed-cycle system and is equipped with a 9 T superconducting magnet for application of external fields. This instrument measures the heat capacity or specific heat of a material at constant pressure with a relaxation technique.

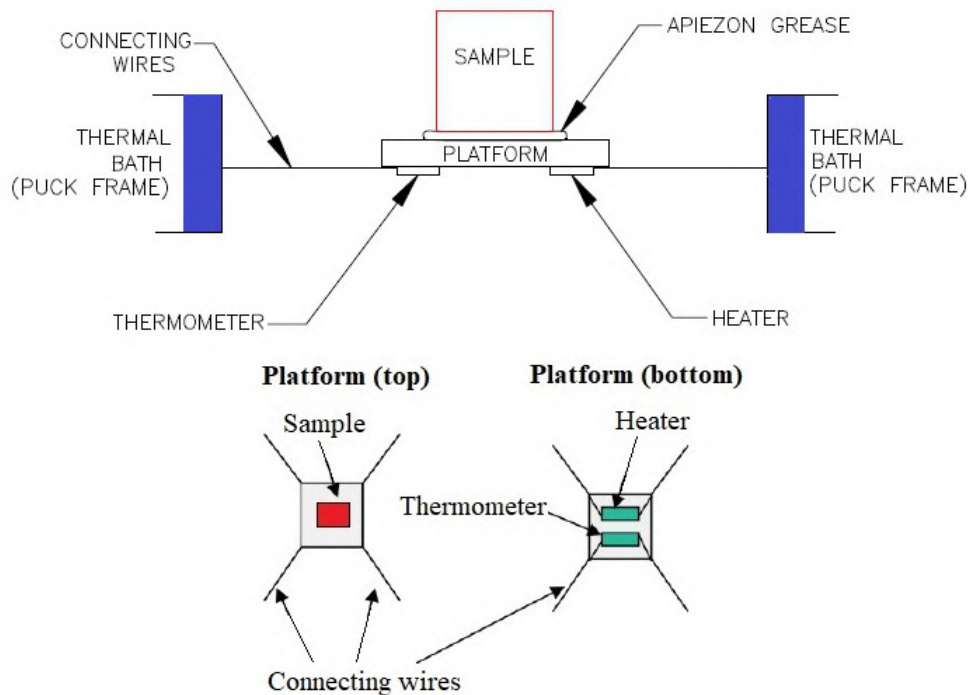


Figure 3.10: Inner components of the calorimeter puck of the PPMS. Figure adapted from [81].

Figure 3.10 shows a diagram of the calorimeter puck which is placed into a high vacuum PPMS cryostat for experiments. Before the measurement can be started, the sample must first be kept at a stable baseline temperature. During the measurement of one point, a known amount of heat P is applied at constant power for a fixed time with a

heater. The heating period is followed by a cooling period of relaxation during the same or longer times [81]. The PPMS consists of a platform heater and platform thermometer which are attached to the bottom side of the platform. Small wires provide electrical connection to the thermometer and heater as well as the thermal connection and support for the platform. The sample is mounted to the platform by using a thin layer of vacuum Apiezon grease which maintains the required thermal contact even at low temperatures.

In the relaxation technique, after each measurement cycle, the response of the temperature of the whole sample platform is fitted to a theoretical model. This model measures the total specific heat C by accounting the thermal relaxation of the sample platform to the bath temperature, and the relaxation between the sample platform and the sample itself [81]. A simple expression for the temperature T of the platform as a function of time t is written as follows [81]

$$C \frac{dT}{dt} = P(t) - K_w(T - T_b), \quad (3.16)$$

where $P(t)$ is the power applied by the heater. The second term express heat loss between platform and the puck. Here, K_w is the thermal conductance of the supporting wires and T_b is the temperature of the thermal bath or puck frame. The heater power $P(t)$ is equal to P_0 during the heating period of the measurement and is reduced to zero during the cooling period [81]. The solution of this equation is given by an exponential function with a characteristic time constant τ equal to C/K_w [81].

By fitting the measured $T(t)$ dependence to the solution of equation 3.16 provides the C value. We are interested only in the specific heat of the sample and in order to isolate it, we must subtract the specific heat of the platform and Apiezon grease (named as addenda) C_{add} . Experiments are carried out by first measuring the specific heat of the addenda. Then, we put the sample on the addenda and run experiments again. The difference $C - C_{add}$ accounts only the specific heat of the sample. Since the amount of Apiezon grease is constantly changed for each sample mounted on the platform, this is a more precise way to measure specific heat than using the puck calibration files of the PPMS software. The thermal data were collected in the temperature region from 2 to 300 K using the heat capacity option of the PPMS.

Dilution refrigerator

To further lower the temperature down to 50 mK and perform specific heat experiments, we use the PPMS equipped with a dilution refrigerator insert.

The dilution refrigerator employs a mixture of the two isotopes ^3He and ^4He to cool to 50 mK. The opposite quantum nature of the isotopes makes them immiscible below about 0.87 K, and they spontaneously separate into two phases [82]. One phase called the dilute phase consists of 6% ^3He and 94% ^4He and the other one named the concentrated phase is almost entirely ^3He . The interface between the two is called the phase boundary. Since ^3He is lighter than ^4He , the ^3He -rich phase sits on top of the dilute phase. Figure 3.11 shows the mixing chamber containing the liquid. The phase boundary is located near to the vertical center of the mixing chamber. The dilute phase extends from the bottom of the mixing chamber through the counter-flow heat exchanger and partially fills the still. By pumping continuously on the still using a turbo pump, it reduces its temperature near to 0.6 K and decreases the ^3He concentration in the still. Osmotic pressure conduct ^3He up the dilute side of the counter-flow heat exchanger from the mixing chamber into the still. To replace ^3He in the dilute phase, ^3He atoms cross the phase boundary from the concentrated phase into the dilute phase. The ^3He atoms doing so by absorbing heat, and providing cooling power.

The ^3He gas exiting from the turbo pump is circulated back into the condenser of the dilution refrigerator for liquefaction. The ^3He transports down through a flow impedance into the still heat exchanger, and then down the concentrated side of the heat exchanger. A flow impedance ensure that the returning gas is at a low enough temperature when it enters the concentrated phase of the mixing chamber. The liquid ^3He then crosses the phase boundary again, completing the circulation path. This way the mixture continuously circulates to provide cooling to the sample and to maintain a temperature of 50 mK.

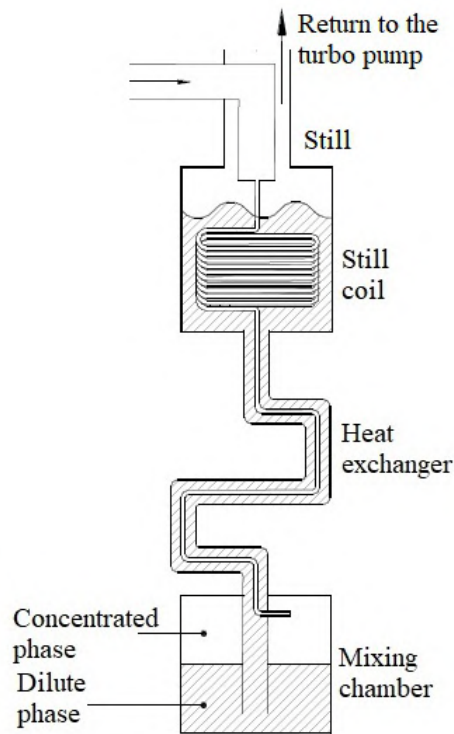


Figure 3.11: Schematic of the dilution refrigerator. Figure adapted from [83].

The dilution refrigerator operates using two cooling modes to allow temperatures down to order of millikelvin. In the mode of dilution cooling, measurements are conducted in the interval of 50 mK to 1.1 K. The refrigerator runs with its full capacity of the ^3He – ^4He mixture and keeping a helium liquid level in the still. By forcing ^3He across the phase boundary or mixing of the two phases requires energy, which is taken from the walls of the mixing chamber and creating its cooling power. The second mode is called the evaporating cooling which is employed for temperatures between 1 and 4 K. Here, the system operates with mostly ^4He in circulation with the helium liquid level down in the mixing chamber. The amount of mixture left is isolated in the tank on its gas-handling system [83]. To achieve this cooling mode, the liquid ^3He is first distilled and then stored in the tank so that almost pure ^4He is left to circulate.

AC measurement system option

We also use the PPMS for ac susceptibility experiments carried out using its ac susceptometer option (ACMS). It operates by using a detection coil set that inductively responds to both the sample magnetic moment and an excitation field [84]. A diagram of the ACMS is shown in figure 3.12. The measurement method is called the extraction method and

it is the same that commercial magnetometers use, as discussed in the previous section. During measurements, an ac field is applied to the measurement region and the sample is located at the center of two detection pickup coils. The signal induced in the detection coils indicates variations on the applied field caused by the presence of the sample.

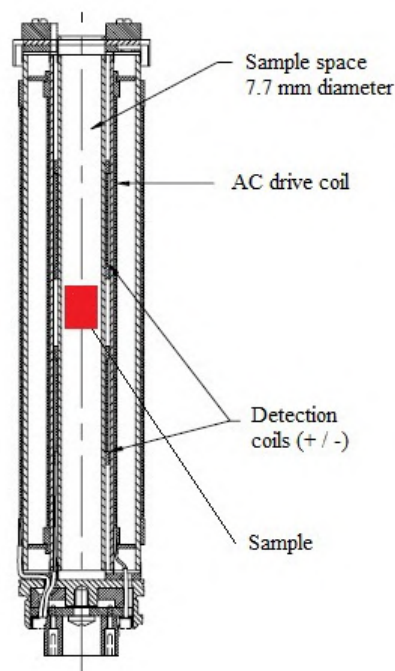


Figure 3.12: Schematic of the ACMS insert. Figure adapted from [84].

Dynamic measurements were completed at the Central Experimental Multiusuário (CEM) facilities of the Universidade Federal do ABC (UFABC). We run experiments with an excitation field of 1 Oe in the frequency range from 10 Hz to 10 kHz.

$\text{Er}_2\text{Ti}_{2-x}\text{Sn}_x\text{O}_7$

In this chapter we discuss about the change of anisotropy of the magnetic ground state of Er^{3+} in the pyrochlore $\text{Er}_2\text{Ti}_2\text{O}_7$ when we introduce Sn ions on the sublattice of Ti. By using the zero-field specific-heat measurements of the $\text{Er}_2\text{Ti}_{2-x}\text{Sn}_x\text{O}_7$ series ($x = 0 - 2$), we perform a different specific-heat analysis from the one reported by our group in [13], and our computation of the contribution terms to the thermal data allow us to gain information about the ground magnetic state of Er^{3+} for each composition in the series. We study physical quantities linked to the electronic magnetic field of Er^{3+} obtained from specific-heat experiments. We collect the in-field specific-heat data of the $\text{Er}_2\text{Ti}_{2-x}\text{Sn}_x\text{O}_7$ series in order to discuss the evolution of the long-range order transition and magnetic excitations.

4.1 Structural analysis

To verify the synthesized polycrystalline phase via the solid-state reaction is indeed $\text{R}_2\text{M}_2\text{O}_7$, we performed x-ray powder diffraction experiments. We collected the data at room temperature only for the $\text{Er}_2\text{Ti}_2\text{O}_7$ sample ($x = 0$) since it was the unique of the series that was provided to us in a required amount for x-ray studies. In figure 4.1, the diffraction data found the sample to be single phase, with no additional impurities detected. By carrying out a Rietveld refinement, and modelling the data with the cubic space group, $Fd\bar{3}m$, consistent with the pyrochlore structure resulted in an excellent fit (red solid line) with a goodness-of-fit value χ^2 close to one. We found a refined cubic lattice parameter of value $a_0 = 10.09 \text{ \AA}$. As reported in [13], the value of a_0 in the series

increases linearly with the Sn content, x , due to the larger ionic radius of Sn compared to Ti.

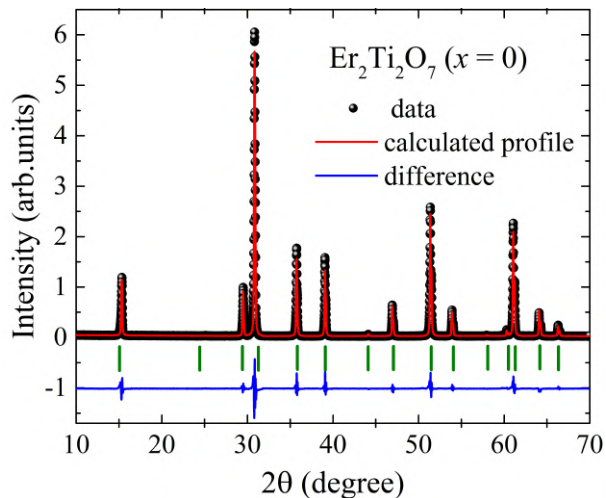


Figure 4.1: X-ray powder diffraction pattern for the $x = 0$ composition. Peak positions of the pyrochlore structure are marked with small vertical lines. The line at the bottom shows the difference between the data and the refinement model.

4.2 Specific heat

Specific-heat experiments were performed down to 50 mK for all the investigated compositions ($x = 0, 0.5, 1, 1.5, 1.7, 1.8, 2$), and the measurements are presented in two sets. The first one presents a thermal analysis including low-temperature fittings to the zero-field specific-heat data which results in direct information about the type of ordering of the magnetic moments of Er^{3+} for each composition. The second set presents the change and the competition of the long-range order magnetic transition and the Schottky anomaly under an external magnetic field up to $\mu_0 H = 2$ T.

4.2.1 Zero field specific heat

In figure 4.2, we present the published data of our group for the temperature dependence of the total specific heat (C) for the $\text{Er}_2\text{Ti}_{2-x}\text{Sn}_x\text{O}_7$ series ($x = 0, 0.5, 1, 1.5, 1.7, 1.8, 2$) measured under zero magnetic field. The total specific heat arises from three terms: the contribution of the lattice C_p , then from the magnetic moment of the nuclei at low temperature C_N , and from the electronic contribution with magnetic origins C_e . As a start we estimate the lattice term C_p for the $\text{Er}_2\text{Ti}_{2-x}\text{Sn}_x\text{O}_7$ series. After isolating the nuclear

and electronic terms ($C_N + C_e$), we perform fittings to the data with some parameters in play as we detail later. The fittings parameters are physical properties directly correlated to the ground magnetic state of Er^{3+} in the series.

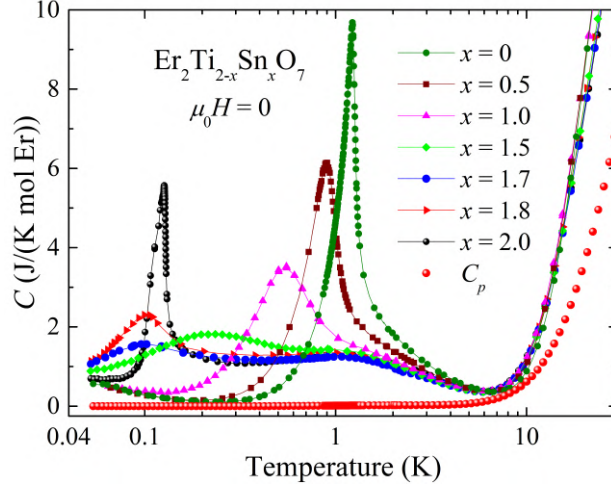


Figure 4.2: Temperature dependence of the total specific heat of $\text{Er}_2\text{Ti}_{2-x}\text{Sn}_x\text{O}_7$ ($x = 0 - 2$). The red points shows the estimated lattice contribution C_p .

Figure 4.3 displays the variation of the height of the transition peak C_{peak} , and the transition temperatures T_N of the series as reported in [13]. The ordering transitions occur at decreasing temperatures T_N when the x content is increased and the observed peak becomes smaller and broader. A linear decrease of T_N for $0 \leq x \leq 1.5$ is observed. Around $x = 1.7$, it is still an open question if exists an interval between $1.7 \leq x \leq 2$ where the series goes trough a quantum phase transition at $T_N = 0$.

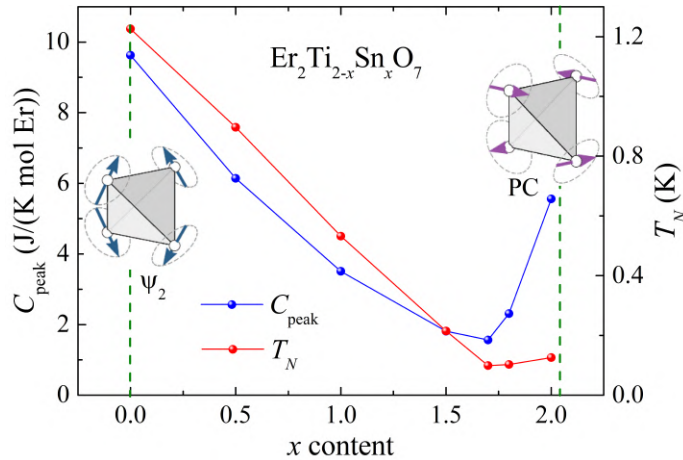


Figure 4.3: Height peak of specific heat C_{peak} and transition temperature T_N versus the x content.

In the accounting for the lattice term is important to state that there is no unique method to do this, and some approximations have to be made. For example, C_p can be estimated as the specific heat of an isomorphic nonmagnetic compound, or as proportional to T^3 in the Debye approach. These methods are constantly used in the literature; however, for our data they result in lattice terms with larger values than the total specific heat. For temperatures above 10 K, the data of the $\text{Er}_2\text{Ti}_{2-x}\text{Sn}_x\text{O}_7$ samples present very slight variations, and for simplicity we consider the lattice terms of the series as constant and equal to the lattice term of $\text{Er}_2\text{Ti}_2\text{O}_7$. We use the scaling method which has been successfully used in pyrochlores [31, 87]. By measuring the specific-heat data of the nonmagnetic $\text{Lu}_2\text{Ti}_2\text{O}_7$, C_p was estimated using the scaling law [88]

$$C_p(T) = C_{\text{Lu}_2\text{Ti}_2\text{O}_7}(T/r), \quad (4.1)$$

where r is the ratio of the Debye temperatures θ for $\text{Er}_2\text{Ti}_2\text{O}_7$ and $\text{Lu}_2\text{Ti}_2\text{O}_7$. Since the Debye temperature θ is inversely proportional to the square root of the molecular weight \bar{M} ($\theta \propto \bar{M}^{-1/2}$) [26]:

$$r = \frac{\theta_{\text{Er}_2\text{Ti}_2\text{O}_7}}{\theta_{\text{Lu}_2\text{Ti}_2\text{O}_7}} = \left(\frac{\bar{M}_{\text{Er}_2\text{Ti}_2\text{O}_7}}{\bar{M}_{\text{Lu}_2\text{Ti}_2\text{O}_7}} \right)^{-1/2}, \quad (4.2)$$

leading to a value of $r = 1.014$. Using this scaling for all the compositions results in differences less than 10% of r , confirming the use of the lattice term of $\text{Er}_2\text{Ti}_2\text{O}_7$ for the series. Figure 4.2 shows the values of the accounted C_p . After subtracting C_p to C , the sum of the terms $C_e + C_N$ is displayed in figure 4.4. We named this sum the magnetic specific heat C_m .

The second step of our analysis of the specific-heat data consists in compute the nuclear (C_N) and the electronic (C_e) contributions. The nuclear term arises from the nuclear magnetic moment of the only isotope ^{167}Er with spin ($I = 7/2$). C_N is determined from the nuclear Hamiltonian \mathcal{H} which counts the contact hyperfine \mathcal{H}_{Hyp} and the electric quadrupolar \mathcal{H}_{Qua} interactions, written as

$$\mathcal{H}_{Hyp} = -\hbar\gamma_{167} \mathbf{I} \cdot \mathbf{B} \quad (4.3)$$

and

$$\mathcal{H}_{Qua} = P \left[\mathbf{I}_z^2 - \frac{1}{3}I(I+1) \right], \quad (4.4)$$

where \hbar is the Planck constant, $\gamma_{167} = -0.772 \times 10^7 \text{ rad s}^{-1} \text{ T}^{-1}$ is the gyromagnetic ratio of ^{167}Er [85], \mathbf{I} is the spin operator, \mathbf{B} is the effective magnetic field due to the Er^{3+} ordered magnetic moments, and P depends of the quadrupole moment Q of ^{167}Er .

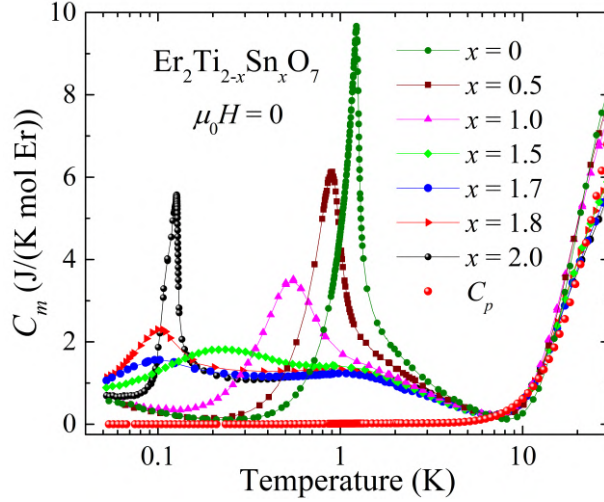


Figure 4.4: Temperature dependence of the magnetic specific heat of $\text{Er}_2\text{Ti}_{2-x}\text{Sn}_x\text{O}_7$ ($x = 0 - 2$).

Due to the XY anisotropy of the ordered moments as reported previously [31], we consider equal the x and y components of \mathbf{B} ($B_x = B_y$). Then,

$$\mathcal{H} = -\hbar\gamma_{167} \mathbf{I} \cdot \mathbf{B} + P \left[\mathbf{I}_z^2 - \frac{1}{3} I(I+1) \right] \quad (4.5)$$

is:

$$\mathcal{H} = -\hbar\gamma_{167} [B_x(\mathbf{I}_x + \mathbf{I}_y) + B_z \mathbf{I}_z] + P \left[\mathbf{I}_z^2 - \frac{1}{3} I(I+1) \right], \quad (4.6)$$

depends of the parameters B_x and B_z . For example, using values reported in [31], for $B_x = 215.7$ T and $B_z = 0$ we obtain eight energy nuclear energy levels E_N : -0.09, -0.07, -0.04, -0.01, 0.02, 0.04, 0.06 and 0.08 K. The nuclear partition function is given by $Z = \sum_{i=1}^8 e^{-\beta E_{N_i}}$, and the calculation of the nuclear contribution to the specific heat is direct.

The electronic contribution C_e to the specific heat arises from magnons. The theory of this contribution has been detailed in the literature [9]. As we present in Chapter 2, for low-energy magnons in $\text{Er}_2\text{Ti}_2\text{O}_7$, the expected electronic contribution C_e is [9]:

$$C_e(T) = A_v \cdot I_\Delta(T) \cdot T^3, \quad (4.7)$$

with

$$A_v = 1534.5 \left(\frac{a_0^3}{v^3} \right). \quad (4.8)$$

Then, C_e depends of the parameters Δ ; which is the gap energy of the magnons, and v ; is the magnon velocity. a_0 is the lattice parameter.

The fits were made numerically by implementing a code in Python language, as shown in Appendix A, since the complexity of the integral $I_\Delta(T)$, and the matricial nature of the spin operators \mathbf{I}_x , \mathbf{I}_y , and \mathbf{I}_z .

Having establish the background of the contributions to the specific heat, we perform the data analysis. Figure 4.5(a) presents the low temperature magnetic specific heat of the $\text{Er}_2\text{Ti}_{2-x}\text{Sn}_x\text{O}_7$ series. For $x = 0, 0.5$, and 1 , the nuclear contribution becomes apparent (below 0.1 K) and it seems to prevail on the specific heat; however, in this region temperature we can not neglect the electronic term. On the other hand, for $x = 1.5, 1.7, 1.8$ and 2 the data does not extend to lower temperatures than 50 mK allowing us to see the nuclear contribution; however, for these compositions the data was measured just after the magnetic transitions in which the electronic contribution dominates. The magnetic specific heat (C_m) for each composition was fitted to the sum of the terms $C_N + C_e$ in the temperature region below the transition peaks. The sum $C_N + C_e$ depends on four parameters B_x , B_z , Δ , and v . Figure 4.5(b) shows the best computed fits for all the investigated compositions.

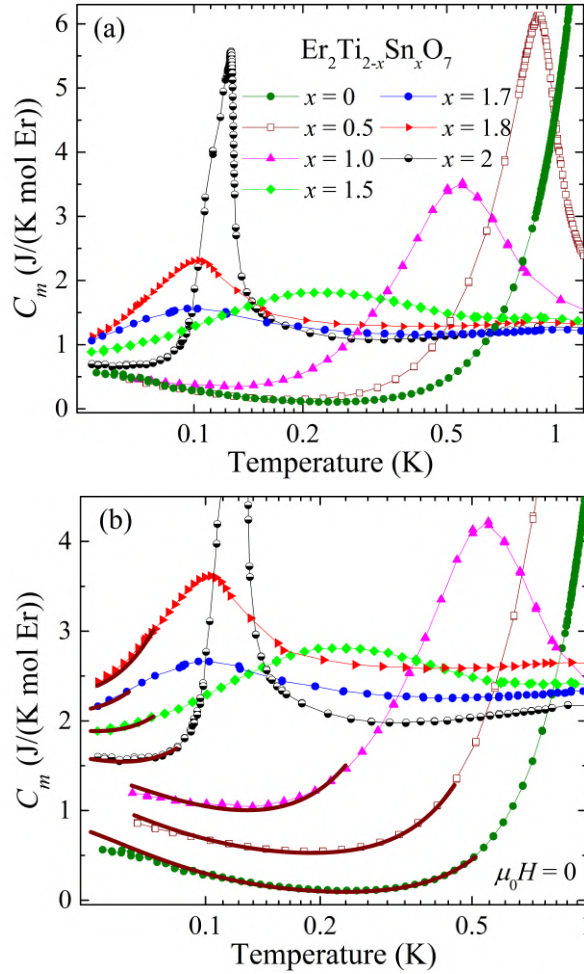


Figure 4.5: (a) The low-temperature magnetic specific heat of the series $\text{Er}_2\text{Ti}_{2-x}\text{Sn}_x\text{O}_7$ ($x = 0 - 2$). (b) The solid lines result from fitting the data to the sum $C_N + C_e$, as explained in the text.

We now report the best parameters obtained from the fits to C_m . The hyperfine components B_x and B_z of each composition tell us about the XY symmetry present and from it we can obtain information about the ordered magnetic moment. By using the ratio between the hyperfine field and the moment which is $87.2 \text{ T}/\mu_B$; as reported by Mössbauer experiments [89], the moment can be estimated. Figure 4.6(a) shows the values of the fitting parameters across the $\text{Er}_2\text{Ti}_{2-x}\text{Sn}_x\text{O}_7$ series. The values of the magnetic moments μ_x (red points) decrease through the series from a value of $3.44 \mu_B$ ($x = 0$) to $2.01 \mu_B$ ($x = 2$). This behaviour is consistent with the decrease of the component μ_x of the magnetic moments obtained from neutron diffraction experiments (blue points) reported in [13]. For samples with $x = 0$ and 0.5 , the best fits are provided when the component B_z or μ_z is zero in contrast with samples with a higher x content (green area). These

results evidence that the system is changing its anisotropy from XY symmetry in $\text{Er}_2\text{Ti}_2\text{O}_7$ ($x = 0$) to having a strong magnetic component μ_z in $\text{Er}_2\text{Sn}_2\text{O}_7$ ($x = 2$). In figure 4.6(b) we show the values of the magnetic moment in the plane XY; $\mu_{xy} = \sqrt{2}\mu_x$, and of the component μ_z , through the different compositions. It exhibits the crossover of the curves approximately at $x = 1.7$ in agreement to the reported curves of the magnetic moments μ_{xy} and μ_z [13].

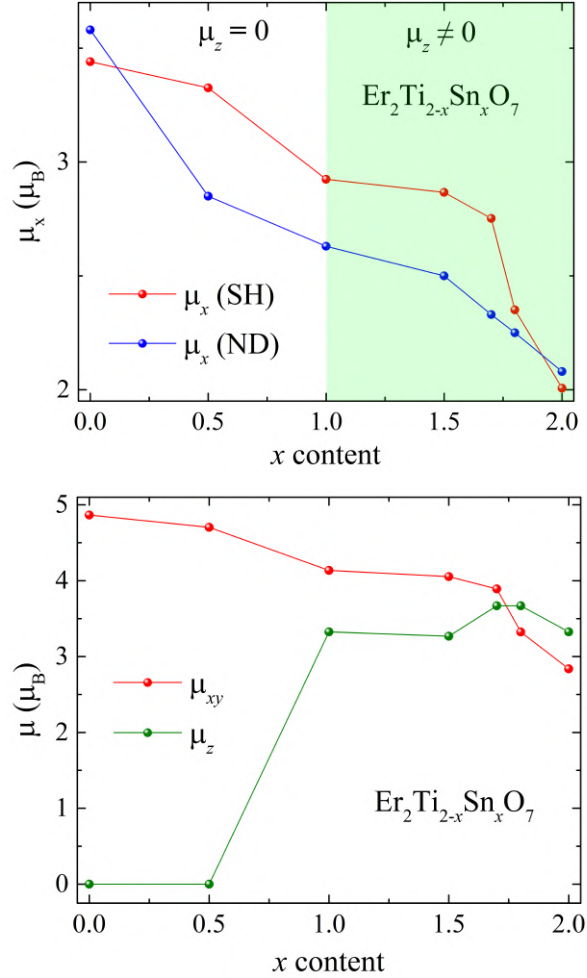


Figure 4.6: (a) Variation in the magnetic moment μ_x with the x content in $\text{Er}_2\text{Ti}_{2-x}\text{Sn}_x\text{O}_7$ obtained from specific heat (SH), which occurs for values of μ_z zero (white area) and non-zero (green area). The values of the magnetic moments reported in [13] and obtained from magnetic neutron diffraction (ND) are included. (b) μ_{xy} and μ_z versus the x content.

From the fits we also compute the values of the spin wave energy gap (Δ) and magnon velocity (v) across the $\text{Er}_2\text{Ti}_{2-x}\text{Sn}_x\text{O}_7$ series. Figure 4.7 shows that the energy gap Δ decreases with x . For $\text{Er}_2\text{Sn}_2\text{O}_7$ it is almost negligible $\Delta \sim 0.0001$ K. A similar decrease is present in the values of v (orange points) followed by a slight increase at $x = 1.8$. This occurs in analogue trend to what occurs with the transition temperatures T_N reported in [13].

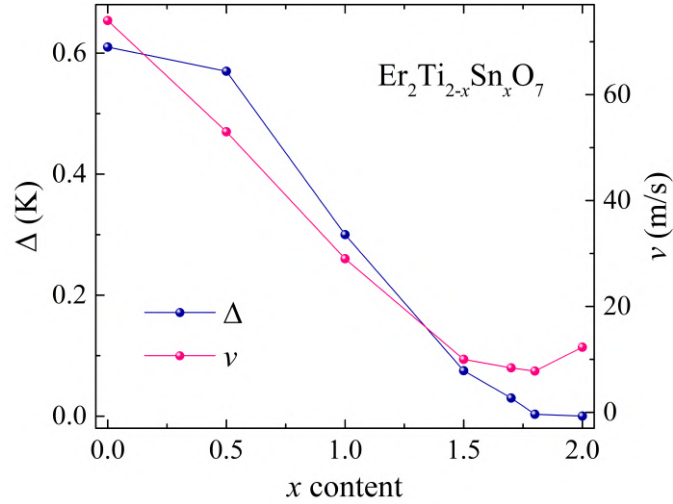


Figure 4.7: Variation in the energy gap Δ and magnon velocity v with the x content in $\text{Er}_2\text{Ti}_{2-x}\text{Sn}_x\text{O}_7$.

We finish this section by computing the recovered entropy of the different compositions of $\text{Er}_2\text{Ti}_{2-x}\text{Sn}_x\text{O}_7$ using our specific-heat data C . We isolate the electronic specific heat C_e by subtracting the contributions from the lattice and nuclear moments to C . We use the estimated lattice term (C_p) and the nuclear term (C_N) of each composition computed from the obtained parameters and fittings presented above in this section. The resulting C_e data is displayed in figure 4.8(a). The recovered electronic entropy $\Delta S_e(T)$ is obtained by integrating $C_e(T)/T$ from 50 mK to 10 K. Figure 4.8(b) shows that the values of $\Delta S_e(T)$ for the $\text{Er}_2\text{Ti}_{2-x}\text{Sn}_x\text{O}_7$ series reach the expected $R \ln(2)$, which is the value for a system with a doublet ground state, at approximately 10 K. For $x = 1.7$, the recovered entropy saturates at a smaller value than $R \ln(2)$. This discrepancy is reasonable considering the limited amount of C_e data in the temperature range below the magnetic transition where low-energy spin excitations dominate.

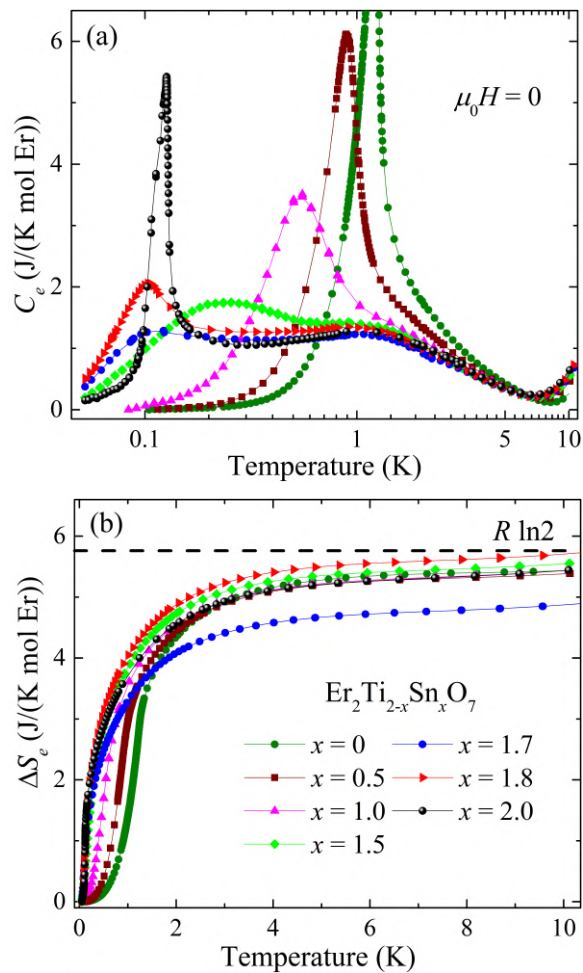


Figure 4.8: (a) Temperature dependence of the electronic specific heat C_e of the $\text{Er}_2\text{Ti}_{2-x}\text{Sn}_x\text{O}_7$ series. (b) The recovered electronic entropy ΔS_e as a function of the temperature. The dashed line $R \ln(2)$ denotes the expected value for a doublet ground state.

4.2.2 In field specific heat

Specific-heat measurements for the $\text{Er}_2\text{Ti}_{2-x}\text{Sn}_x\text{O}_7$ series ($x = 0 - 2$) were taken up in various applied magnetic fields, and the results are presented in this section. Figure 4.9 shows the temperature dependence of the specific heat C for $x = 0, 0.5, 1.0, 1.5, 1.7$ and 1.8 . The application of a magnetic field ($\mu_0 H$) causes the ordering-transition peaks at T_N to shift monotonically to lower temperature and to decrease in amplitude. For all compositions, the sharp peak positioned at T_N is followed by a broad Schottky anomaly on the high-temperature side. This broad feature centered at ~ 2 K becomes evident for $x \geq 0.5$. For the $x = 1.7$ and 1.8 samples, the peak seen in the zero-field C curves is replaced by a much broader feature in modest values of fields, and also the Schottky anomaly developed at ~ 2 K becomes rapidly visible. For fields above 1.5 T there are no sharp features in the data and the magnitude of C decreases rapidly with increasing $\mu_0 H$. This is consistent with the critical field value $\mu_0 H_c = 1.5$ T reported in $\text{Er}_2\text{Ti}_2\text{O}_7$ for which the sharp peak disappears suggesting a quantum critical point [31, 92]. For all compositions $x = 0 - 2$, the specific heat converges to the same temperature dependence around 10 K and then lattice contribution which dominates at this temperature range is clearly independent of applied field. At the lowest temperature an upturn in the specific heat is attributed to nuclear contributions from the Er atoms. [86].

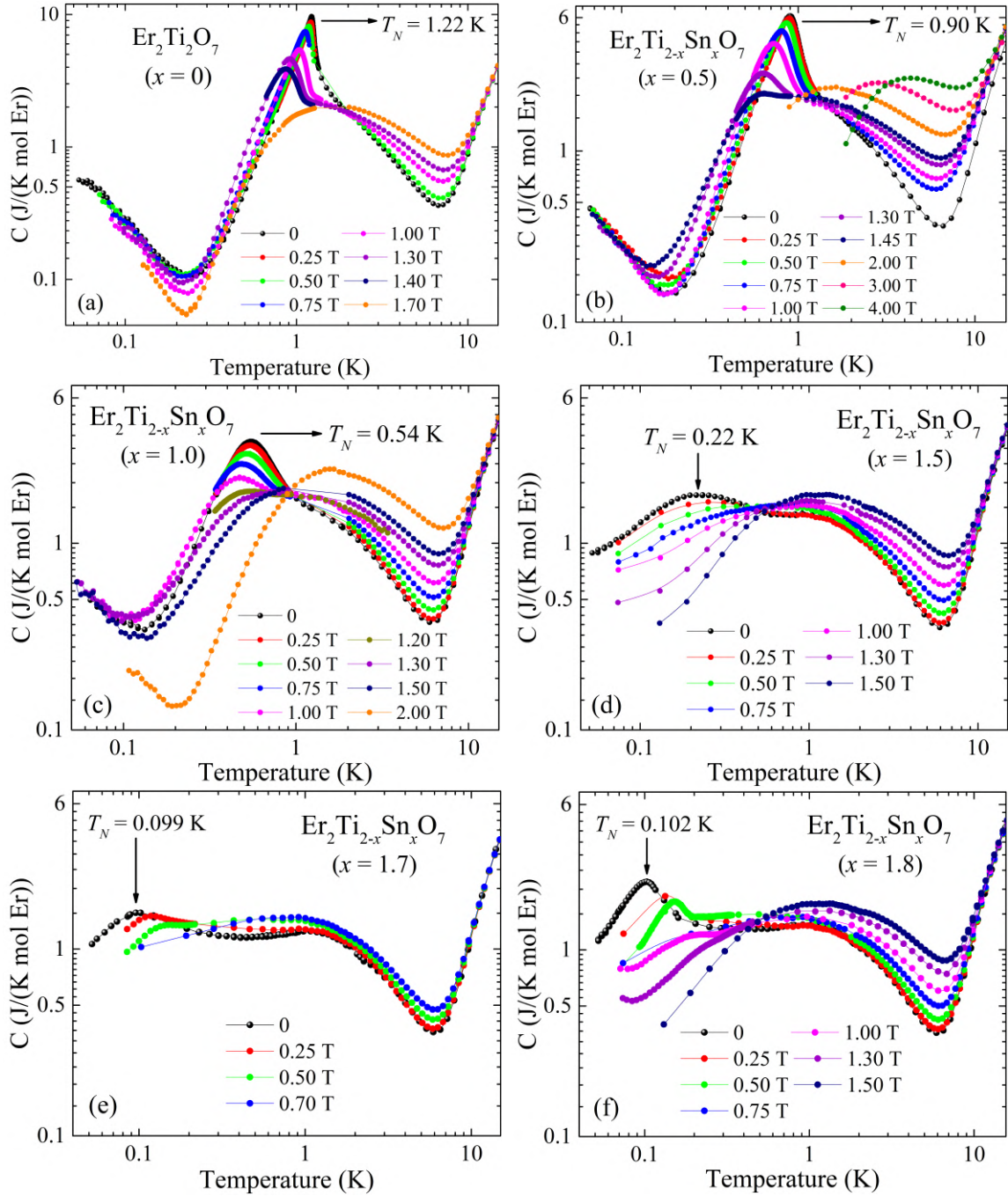


Figure 4.9: Specific heat of $\text{Er}_2\text{Ti}_{2-x}\text{Sn}_x\text{O}_7$ ($x = 0, 0.5, 1.0, 1.5, 1.7$ and 1.8) for different applied magnetic fields. T_N marks the temperature of the ordering transition at zero field.

Figure 4.10(a) shows the temperature dependence of C for $\text{Er}_2\text{Sn}_2\text{O}_7$ ($x = 2$) in different magnetic fields. The sharp peak in the specific heat at $T_N = 0.130$ K decreases rapidly in magnitude and broadens with increasing fields. The position of the peak does not change monotonically with the applied field, the peak first shifts to higher temperature in fields up to 0.5 T, then it moves to lower temperature in the field range of 0.6–0.7 T, and finally it shifts back again to higher temperature in a field of 1 T. Data measured in fields above 1.3 T revealed no sharp features but instead a broad Schottky anomaly centered at 2 K associated with in-field excited levels. Figure 4.10(b) shows that the Schottky anomaly moves to higher temperature and its magnitude increases rapidly with fields higher than 1.5 T. The values of C at temperatures above 10 K are once again attributed to the lattice term which is observed to be independent of the applied field.

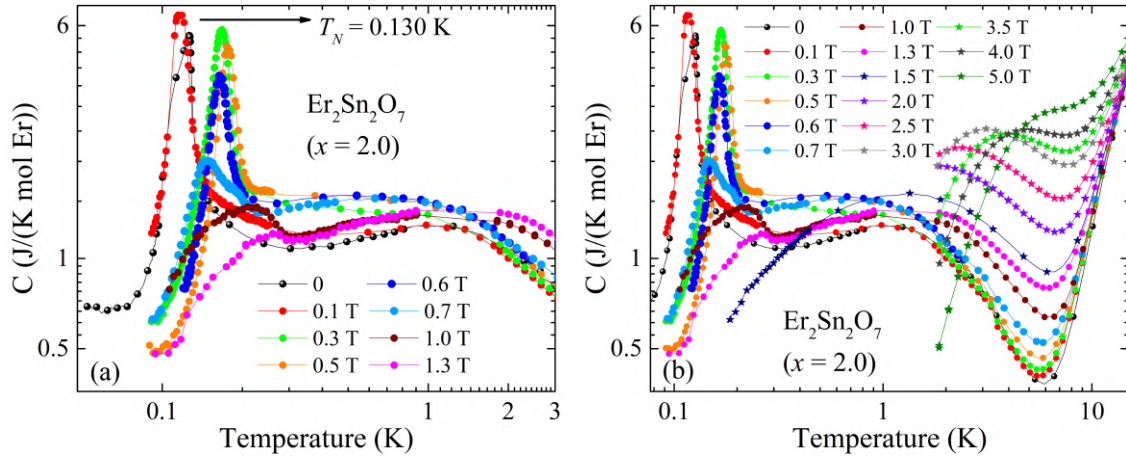


Figure 4.10: Temperature dependence of the specific heat of $\text{Er}_2\text{Sn}_2\text{O}_7$ for different magnetic fields. T_N marks the temperature of the ordering transition at zero field.

We now construct the field–temperature (H – T) phase diagram for the $\text{Er}_2\text{Ti}_{2-x}\text{Sn}_x\text{O}_7$ series using the specific–heat data shown in figures 4.9 and 4.10. The temperature in which occurs the sharp peak versus the field intensity is displayed in figure 4.11. Our results for $x = 0$ are in agreement with the published work in single crystals of $\text{Er}_2\text{Ti}_2\text{O}_7$ [31, 91, 92]. For $x = 0.5$, the same delineated tendency is maintained but shifted to low temperature. The H – T diagram displays two clear trends marked by the dashed arrows: for samples with $x = 0, 0.5$, and 1.0 the maximum of the specific–heat peak moves to lower temperatures as the field increases, and for $x = 1.5, 1.7, 1.8$, and 2.0 the specific–heat peak does the opposite behaviour. These different trends can be associated to the two different magnetic phases developed.

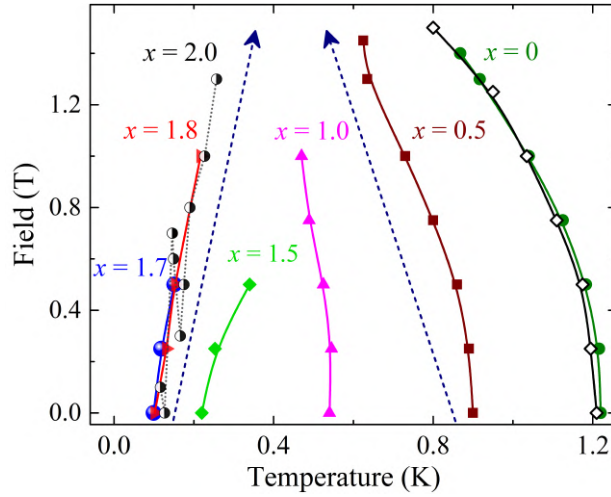


Figure 4.11: The phase diagram of the $\text{Er}_2\text{Ti}_{2-x}\text{Sn}_x\text{O}_7$ series ($x = 0 - 2$) derived from specific-heat measurements in different magnetic fields. The open symbols show experimental data from Dalmas de Réotier *et al.* [31]. The lines connecting the symbols are guides to the eye.

Upon increasing the field the single sharp peak of the specific heat for each composition is progressively suppressed and the Schottky anomaly moves to higher temperatures. These features are indications of a excitation gap increasing monotonically with external field. In order to measure this trend we compare the data to the behaviour expected for a system with an excited level at energy $\Delta\varepsilon$ above the ground state using equation 2.17. This equation was fitted to the in-field measured data in the temperature range up to the broad peak maximum and avoiding the transition-peak part where magnetic contributions are seen. Before fitting the data, the lattice contribution C_p was subtracted from the total specific heat C .

Figure 4.12 shows the temperature dependence of the specific heat divided by temperature, C/T , for $x = 0, 0.5, 1, 1.5, 1.7$ and 1.8 and their respective fits to equation 2.17. For fields smaller than 1.5 T, we observe that the C data can be described by equation 2.17 in the temperature region above 2 K. Around 10 K, the solid line of the fits do not reproduce well the data since in small fields the Schottky anomaly is not entirely visible. For $x = 0.5$ we have measured the C curves in fields higher than 2 T, and here the fit encompasses the values of the entire Schottky maximum showing that the excitations can be in fact modelled as two-level systems with a field-dependent gap $\Delta\varepsilon$.

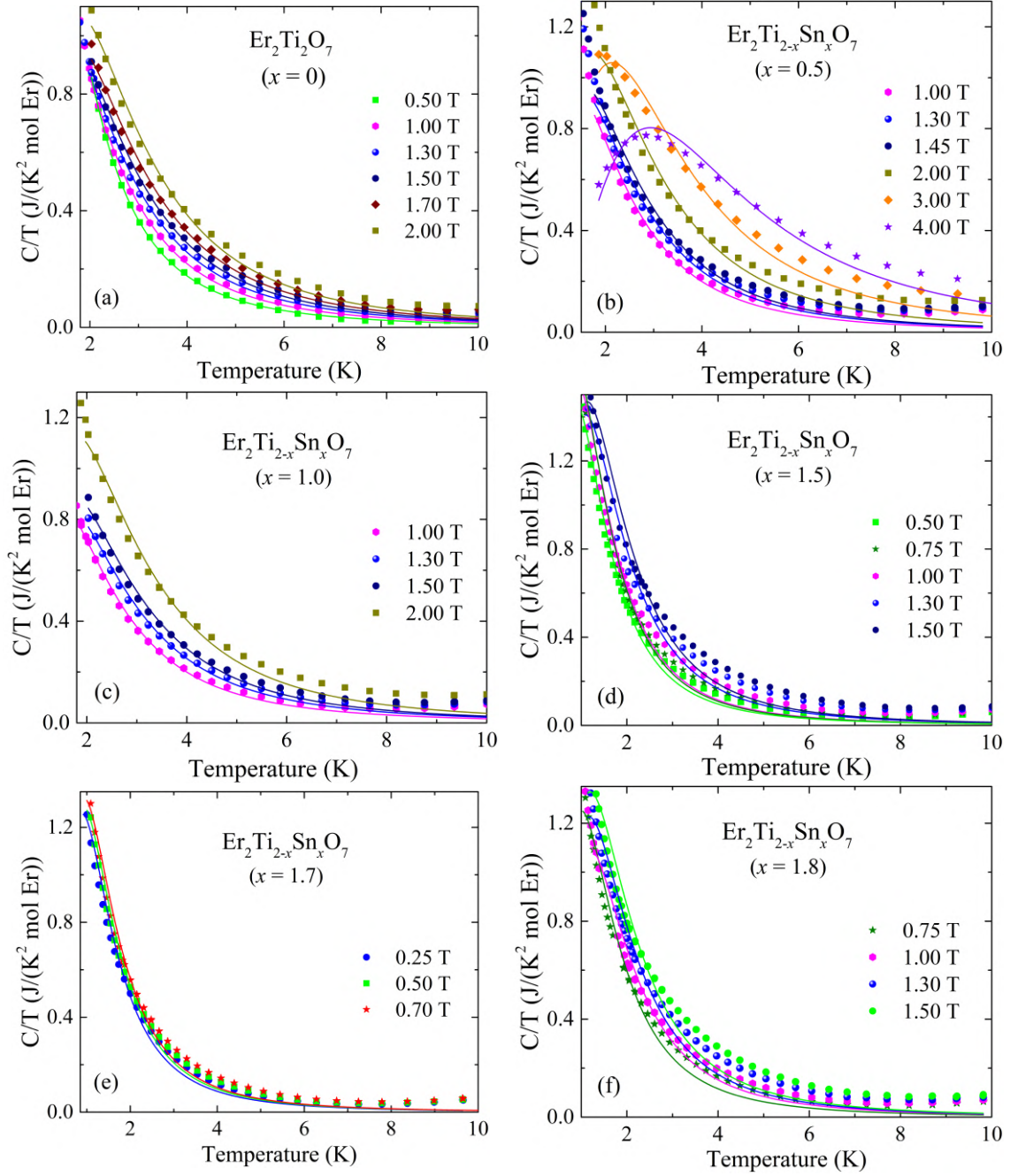


Figure 4.12: Temperature dependence of C/T of $\text{Er}_2\text{Ti}_{2-x}\text{Sn}_x\text{O}_7$ ($x = 0, 0.5, 1, 1.5, 1.7$ and 1.8) measured in different applied magnetic fields. Red solid lines show fits of C to the equation 2.17.

Figure 4.13 shows the temperature dependence of the C/T data for small-field and high-field values of $\text{Er}_2\text{Sn}_2\text{O}_7$ ($x = 2$). For fields smaller than 1.5 T, we observe that C can be described by equation 2.17 in the temperature region between 1 and 5 K, as shown in figure 4.13(a). In fields higher than 2 T, the Schottky maximum of the C curves can be described again as two-level systems with the presence of a gap energy.

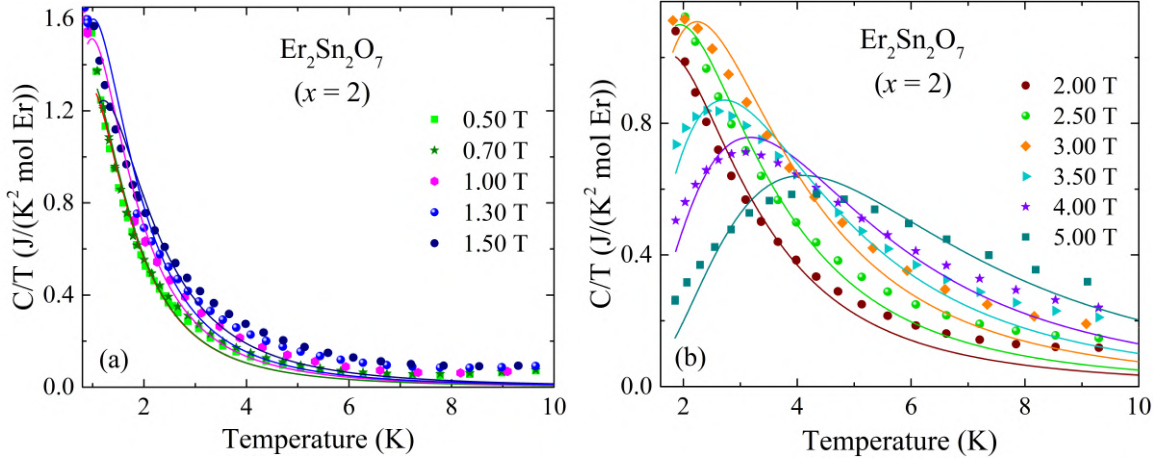


Figure 4.13: Temperature dependence of C/T of $\text{Er}_2\text{Sn}_2\text{O}_7$ ($x = 2$) in different applied magnetic fields.

The field dependence of the gap values $\Delta\varepsilon$ is presented in figure 4.14. The $\Delta\varepsilon$ values for $x = 0$ are consistent with the ones obtained from Schottky fits to in-field specific heat studies of $\text{Er}_2\text{Ti}_2\text{O}_7$ [91]. Our measurements for $x = 0.5$ and 2 in the field region above 2 T show the same linear field-dependence and values of the gap $\Delta\varepsilon$ as observed for $x = 0$. This could suggest the same linear behaviour across the series. For fields smaller than the critical point of 1.5 T, the values of $\Delta\varepsilon$ across the series present a slow but monotonically increase in applied field. In this field interval, $\Delta\varepsilon$ takes values between 3 and 5 K.

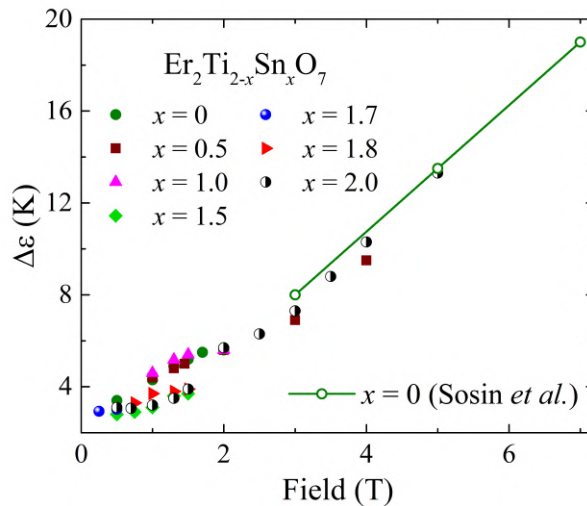


Figure 4.14: Gap values $\Delta\varepsilon$ determined from fitting the in-field data to equation 2.17. The open symbols show experimental data from Sosin *et al.* [91].

4.3 Discussion

Results from the fitting of the low temperature specific heat to the sum proposed $C_N + C_e$; for $\text{Er}_2\text{Ti}_{2-x}\text{Sn}_x\text{O}_7$, confirm that the XY ground state is present for $x = 0$, as reported in the literature [20], but also for small contents of x . This result indicates robustness of the ground state and it is similar to the behaviour observed in [32] for which the ground state ψ_2 is preserved at small levels of dilution (around 20 %). For samples with composition x between 1.5 and 2, we observe that it starts to develop a component of the magnetic moment μ_z , which remains almost constant (see figure 4.6(a)). The change in the magnetic ground state is consistent with the Palmer–Chalker state in $\text{Er}_2\text{Sn}_2\text{O}_7$, as reported by neutron scattering in [13, 14].

From the T_N plot of figure 4.3, its linear behaviour followed by a small increase in T_N is similar to what occurs with the magnon velocity (see figure 4.7), meaning a decrease in the antiferromagnetic exchange constant trough the $\text{Er}_2\text{Ti}_{2-x}\text{Sn}_x\text{O}_7$ series.

The electronic specific heat of the $\text{Er}_2\text{Ti}_{2-x}\text{Sn}_x\text{O}_7$ samples for fields above 1.5 T, show no peak observed analogue to $\text{Er}_2\text{Ti}_2\text{O}_7$ [31]. The phase diagram of figure 4.11 resuming these results suggest that there is a possible quantum critical point driven by field. From the two dashed arrows shown in figure 4.11, it seems that small levels of dilution from the first and final members of the series maintain the magnetic phases induced by field. However, for the $x = 1.5$ and 1.7 compositions, we found that the peak vanishes even at a lower magnetic field than 1 T.

Dy₂Zr₂O₇

In this chapter we cover results concerning our study of the dysprosium zirconate Dy₂Zr₂O₇ through low-temperature thermodynamic experiments and neutron diffraction, and discuss its magnetic and structural properties. The trivalent magnetic Dy ion together with the Zr ion in the $R_2M_2O_7$ compounds is known to favour a disordered defect-fluorite structure, unlike the pyrochlore spin ice Dy₂Ti₂O₇. We compare the two dysprosium compounds, and discuss the similarities present in their thermodynamics. However, the spin-ice behaviour is absent in Dy₂Zr₂O₇ and we instead find spin-liquid features with very dynamic and short-range antiferromagnetic correlations below 10 K.

5.1 Structural analysis

We present the x-ray powder diffraction (XPD) and neutron powder diffraction (NPD) data collected at room temperature for Dy₂Zr₂O₇ and ¹⁶²Dy₂Zr₂O₇, respectively. All the peaks of both patterns could be indexed according to the calculated profile for the defect-fluorite structure with $Fm\bar{3}m$ space group, with no additional phases detected, as seen in figures 5.1(a) and 5.1(b). Summary of the employed model and refined parameters for the Dy₂Zr₂O₇ and ¹⁶²Dy₂Zr₂O₇ samples are presented in table 5.1. The calculated profile returned a lattice parameter $a_0 = 5.238(2)$ Å consistent with previous results [93–95], and the overall quality of the fit to the XPD data; as shown by the weighted R_{wp} -factor and χ^2 , is excellent. For the NPD data, the R_{wp} and χ^2 values are larger than expected but this is due to the poor statistics and sample size of ¹⁶²Dy₂Zr₂O₇. The refinement reveals that the total occupancy of the $4a$ site of Dy/Zr is close to one (100%) as well

for the occupancy of the $8c$ oxygen, excluding possibility of vacancies on both sites. In the defect-fluorite lattice 7 oxygen atoms surround locally to the rare-earth cations, distinct from the pyrochlore lattice in which the environment of the rare-earth is formed by 8 oxygen anions lying on two different crystallographically sites. The local rare earth environment in the defect-fluorites suggests a different scenario on the CEF levels from their pyrochlore-related ones.

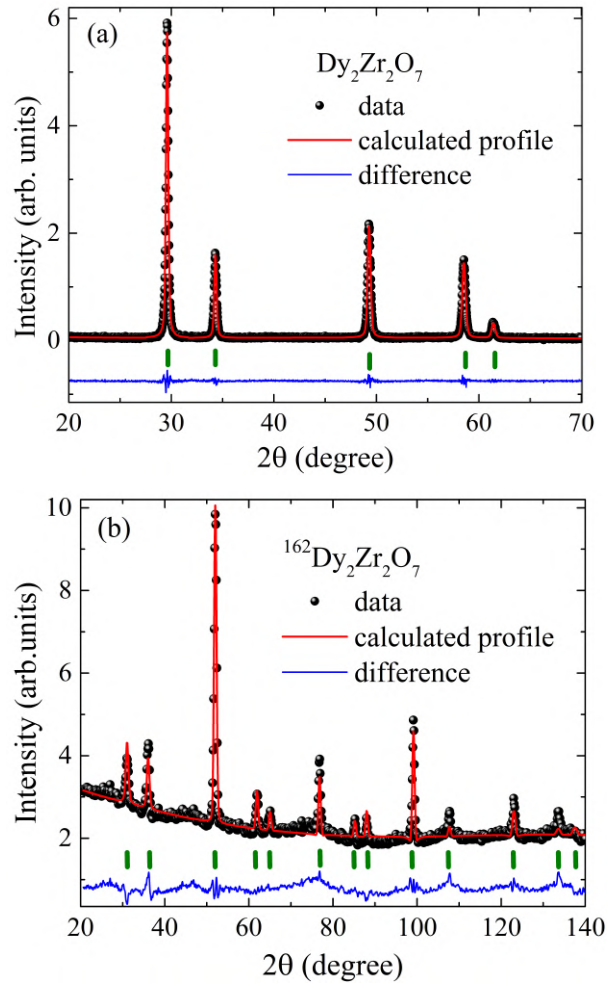


Figure 5.1: XPD pattern for $\text{Dy}_2\text{Zr}_2\text{O}_7$ (a), NPD pattern for $^{162}\text{Dy}_2\text{Zr}_2\text{O}_7$ (b), and their respective calculated profiles. Peak positions of the fluorite structure are marked with small vertical lines. The solid blue lines show the difference between the data and the refinement model.

	Dy ₂ Zr ₂ O ₇	¹⁶² Dy ₂ Zr ₂ O ₇
Space group	$Fm\bar{3}m$	$Fm\bar{3}m$
Lattice parameter (Å)	5.238(2)	5.223(2)
Occ. Dy ³⁺ : 4a	0.50	0.49
Occ. Zr ⁴⁺ : 4a	0.50	0.50
Occ. O ²⁻ : 8c	1	0.96
R_{wp} (%)	14.9	33.2
χ^2	1.46	4.26

Table 5.1: Refined structural parameters for Dy₂Zr₂O₇ and ¹⁶²Dy₂Zr₂O₇.

5.2 DC magnetization

We performed measurements of the temperature dependence of magnetization, M , in a static magnetic field $\mu_0 H = 0.01$ T for Dy₂Zr₂O₇ using a Quantum Design SQUID magnetometer. In figure 5.2(a) we display the inverse of the dc susceptibility ($1/\chi = \mu_0 H/M$) versus temperature and its fit to the Curie–Weiss law. The values of $1/\chi$ develop linearly within a large temperature range down to 10 K. The fit in the regime between 10 and 100 K yields a negative Curie–Weiss temperature $\Theta_{CW} = -3.2$ K indicating the dominance of antiferromagnetic interactions. The effective magnetic moment was found to be $\mu_{eff} = 10.5 \mu_B/\text{Dy ion}$ in agreement to the expected $10.6 \mu_B/\text{Dy ion}$ for free Dy³⁺. Using the mean–field approximation, the nearest–neighbour exchange interaction is estimated from the Curie–Weiss temperature Θ_{CW} by $J = 3\Theta_{CW}/z\mathbf{J}(\mathbf{J} + 1) = 0.03$ K, where $z = 6$ is the number of nearest neighbours. A ferromagnetic $\Theta_{CW} = +0.5$ K and a effective coupling constant $J = 1.1$ K were reported for the spin ice Dy₂Ti₂O₇ [8]. The saturation magnetization as a function of magnetic field of Dy₂Zr₂O₇ was also measured, as shown in figure 5.2(b). For the free Dy³⁺ ion, the saturation moment is expected to be $10 \mu_B/\text{Dy ion}$. At 2 K, we found that the saturation moment at 7 T is close to $5 \mu_B/\text{Dy ion}$ similar to Dy₂Ti₂O₇. Fukazawa *et al.* [96] stated that for Dy₂Ti₂O₇ the crystal–field–induced anisotropy reduces the saturation moment to be half the free–ion value. These magnetization results indicate that Dy₂Zr₂O₇ presents dominant antiferromagnetic interactions and a possible easy–axis anisotropy.

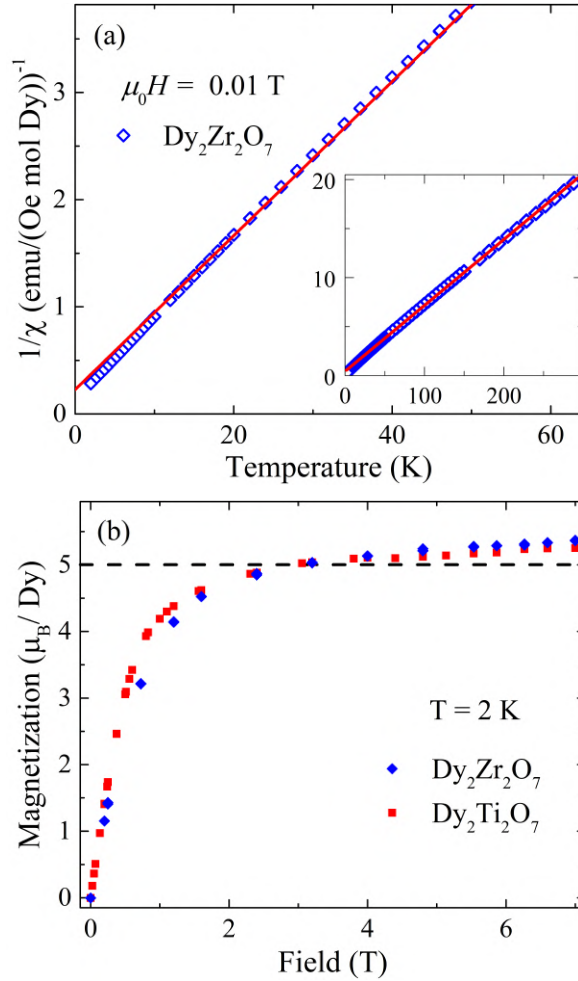


Figure 5.2: (a) Inverse susceptibility versus temperature and Curie–Weiss fit to the lowest temperature. The inset shows the data measured in an extended temperature range. (b) Saturation magnetization as a function of the applied field shows a saturation moment at a value of approximately $5 \mu_B/\text{Dy}$ (dashed line).

5.3 AC magnetic susceptibility

In order to examine the spin dynamics in $\text{Dy}_2\text{Zr}_2\text{O}_7$, we study the real part of its ac magnetic susceptibility (χ'_{ac}). Down to 50 mK, experiments were carried out using an adiabatic demagnetization refrigerator (ADR) inside a ^4He cryostat. The temperature dependence of χ'_{ac} reveals a frequency–dependent maximum at $T' \approx 1 \text{ K}$, as shown in figure 5.3. The shape and height of these maxima are similar to the ones reported in the pyrochlore spin ice $\text{Dy}_2\text{Ti}_2\text{O}_7$ [38, 39]. The drop in χ'_{ac} below T' indicates that the spins response is slowed that they cannot respond to the time–varying field. Contrary to what is observed in $\text{Dy}_2\text{Ti}_2\text{O}_7$, the values of χ'_{ac} do not drop to zero even at 0.5 K.

χ'_{ac} measurements up to 50 K show that in $\text{Dy}_2\text{Zr}_2\text{O}_7$ there is no maximum appearing at temperature ≈ 19 K as reported for $\text{Dy}_2\text{Ti}_2\text{O}_7$ in [38, 39].

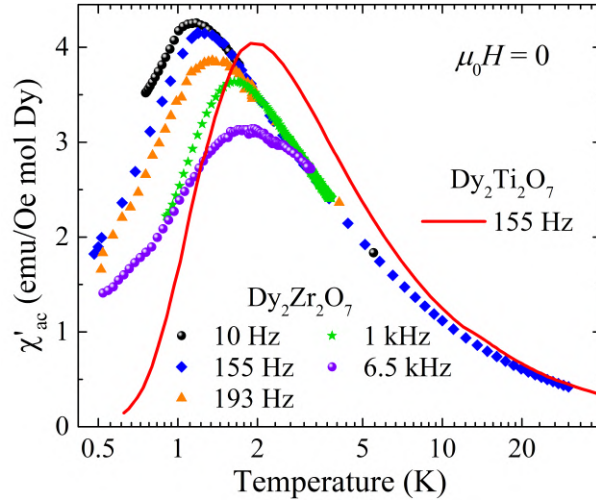


Figure 5.3: Real part of the ac magnetic susceptibility χ'_{ac} versus temperature for different frequencies in zero magnetic field for $\text{Dy}_2\text{Zr}_2\text{O}_7$ and $\text{Dy}_2\text{Ti}_2\text{O}_7$.

As the frequency of the ac measurement increases, the maximum close to 1 K shifts toward higher temperatures and becomes broader. We can characterize the dynamics of $\text{Dy}_2\text{Zr}_2\text{O}_7$ by fitting the frequency, f , versus the temperature, T' , of the maximum in χ'_{ac} to an Arrhenius law $f = f_0 \exp(-E_b/k_B T')$, where E_b is the energy barrier. The f and T' values are reported in table 5.2. We plotted them in figure 5.4 and observed that the Arrhenius law gives a good description of the entire temperature and frequency range data. We estimated a single characteristic relaxation time of $\tau_0 = 1/2\pi f_0 = 4.5 \times 10^{-5}$ s and an energy barrier $E_b = 8$ K. Our obtained values are close to the parameters reported in $\text{Dy}_2\text{Ti}_2\text{O}_7$ below 1 K in the spin-ice phase, which are an energy barrier $E_b \approx 10$ K and a relaxation time on the order of 10^{-7} s [37–39]. The frequency shift of the χ'_{ac} maximum per decade frequency $\delta T' = \Delta T' / (T' \Delta \log f)$ is a signature of a canonical spin glass behaviour for $\delta T' = 0.005 - 0.01$ [55]. By using the values of table 5.2, we find an average value $\delta T' \approx 0.21$ indicating a slower dynamics than in typical spin glasses.

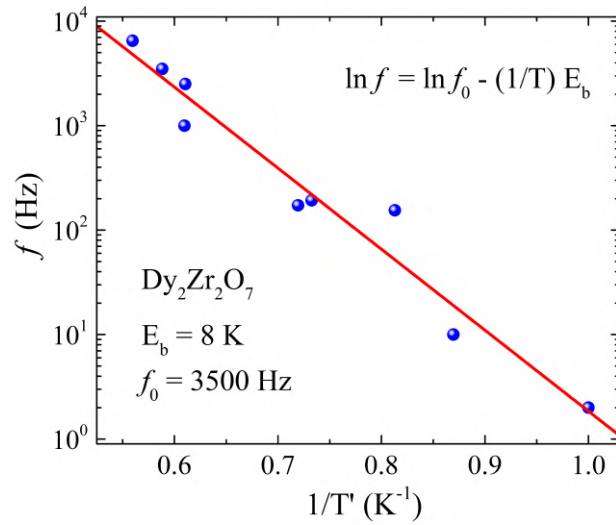


Figure 5.4: Frequency of the measurement (f) versus the inverse of the temperature of the maximum in χ'_{ac} ($1/T'$) with a fit to the Arrhenius law.

f (Hz)	T' (K)	$\delta T'$
2^a	1.00^a	0.21^\dagger
10^b	1.15^b	0.15^\ddagger
155	1.23	–
173	1.39	–
193^c	1.37^c	0.28^*
1000^d	1.64^d	–
2500	1.64	–
3500	1.70	–
6500	1.79	–

Table 5.2: Frequency f , the temperature T' , and the $\delta T'$ values for Dy₂Zr₂O₇. \dagger results from the values marked with a and b , \ddagger comes from the values labelled with b and c , and $*$ results from the values marked with c and d .

Before finishing this section, we note another similarity in the low-temperature regime between this antiferromagnetic fluorite Dy₂Zr₂O₇ and the ferromagnetic pyrochlore spin ice Dy₂Ti₂O₇ which is the characteristic spin-relaxation time τ . Figure 5.5 shows the temperature dependence of τ , obtained from the ac susceptibility and taken as the inverse of the measuring frequency at the maximum temperature. Below 2 K, we know that spin-

spin correlations are present from our next neutron-diffraction results, and we observe that the temperature dependence and values of the characteristic timescale match that of $\text{Dy}_2\text{Ti}_2\text{O}_7$ reported in [97]. The values of τ within $\text{Dy}_2\text{Zr}_2\text{O}_7$ increase rapidly and extend down to the spin-ice state of $\text{Dy}_2\text{Ti}_2\text{O}_7$ where monopole excitations are created and propagate through the lattice. Between 2 and 10 K, no plateau regime associated to quantum tunnelling was observed in $\text{Dy}_2\text{Zr}_2\text{O}_7$, as reported for $\text{Dy}_2\text{Ti}_2\text{O}_7$ [98,99].

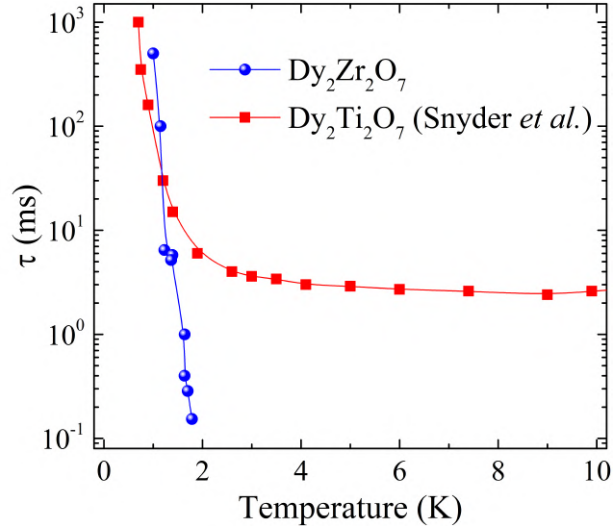


Figure 5.5: Characteristic spin-relaxation time τ as a function of temperature in $\text{Dy}_2\text{Zr}_2\text{O}_7$ and $\text{Dy}_2\text{Ti}_2\text{O}_7$ (digitalized from Snyder *et al.* [97]).

5.4 Specific heat

Specific heat measurements down to 70 mK for $\text{Dy}_2\text{Zr}_2\text{O}_7$ and $\text{Dy}_2\text{Ti}_2\text{O}_7$ were obtained using a Quantum Design PPMS calorimeter equipped with a ^3He - ^4He dilution refrigerator. Figure 5.6 shows the temperature dependence of the total specific heat (C) measured in zero field. The C data of $\text{Dy}_2\text{Zr}_2\text{O}_7$ display a broad peak at about 1.5 K, similar to our data of the spin ice $\text{Dy}_2\text{Ti}_2\text{O}_7$ and reminiscent of the results from Ramirez *et al.* [7], and could be associated with short-range magnetic correlations. Above 10 K, the lattice contribution is sizeable and was accounted for each compound as the measured specific heat of the nonmagnetic fluorite $\text{Lu}_2\text{Zr}_2\text{O}_7$ (C_{p1}) or of the pyrochlore $\text{Lu}_2\text{Ti}_2\text{O}_7$ (C_{p2}). Below 0.2 K, the nuclear contribution C_N dominates and arises from the nonspinless isotopes present in our compound, namely, ^{161}Dy and ^{163}Dy , with nuclear spin $I = 5/2$ and hyperfine and quadrupole interactions. For $\text{Dy}_2\text{Zr}_2\text{O}_7$ and $\text{Dy}_2\text{Ti}_2\text{O}_7$, C_N was calculated using a set of interaction parameters reported for metallic Dy [100], as detailed in Appendix A.

The C data of $\text{Dy}_2\text{Ti}_2\text{O}_7$ appears to be smaller than C_N below 0.2 K but this could be due that there is a difference on the specific-heat values of $\text{Dy}_2\text{Ti}_2\text{O}_7$ if measurements are thermally equilibrated as reported by Pomaranski *et al.* [101]. We also collected data for the isotopically enriched $^{162}\text{Dy}_2\text{Zr}_2\text{O}_7$ which displays the same high temperature behaviour above 10 K and a broad peak around 1 K as the former dysprosium samples. We observe a total absence of the nuclear contribution below 0.5 K since the isotope ^{162}Dy is a spin $I = 0$.

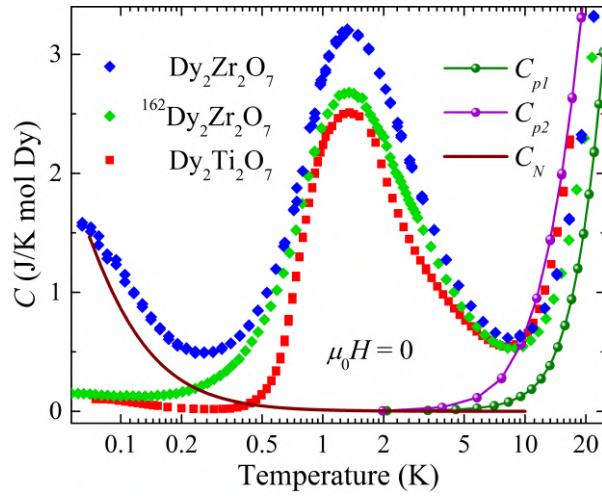


Figure 5.6: Temperature dependence of the total specific heat for $\text{Dy}_2\text{Zr}_2\text{O}_7$, $\text{Dy}_2\text{Ti}_2\text{O}_7$, and $^{162}\text{Dy}_2\text{Zr}_2\text{O}_7$ at zero field. The lattice terms (C_{p1} and C_{p2}) and the nuclear specific heat (C_N) are displayed.

After subtracting C_p and C_N to the total specific heat C , we obtain the electronic contribution C_e which is displayed in figure 5.7(a). The C_e curves show values close to zero above and below temperatures of the peak, and then our subtraction approximation is reliable. By fitting C_e to the two-level Schottky equation (2.17), we found excellent descriptions of the data for all samples in the temperature interval of 0.5 to 12 K. The energy gaps ($\Delta\varepsilon$) obtained from the fits are very close to each other with values of $\Delta\varepsilon \approx 3.3$ K for our three dysprosium compounds. These results agree with the doublet ground state reported for $\text{Dy}_2\text{Ti}_2\text{O}_7$ in the literature [23, 102]. By integrating $C_e(T)/T$ from the minimum measured to the temperature T , we computed the recovered electronic entropy ΔS_e . Figure 5.7(b) shows that the values of ΔS_e are close to the expected $R \ln 2$ for a system with only two discrete orientations, at approximately 8 K. This indicates that the residual entropy left as T goes to zero is small, if not negligible, and considerable less

than the Pauling entropy $R[\ln 2 - (1/2)\ln 3/2]$ found in spin ices ($\text{Dy}_2\text{Ti}_2\text{O}_7$) and water ice [103].

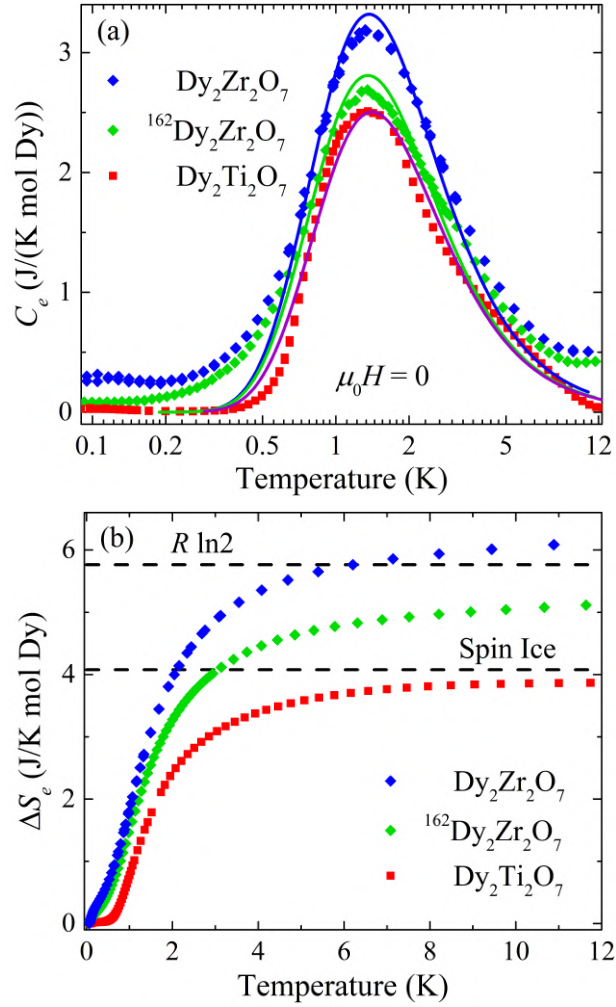


Figure 5.7: (a) Electronic specific heat $C_e(T)$ at zero field. Solid lines are the two-level Schottky fits using equation (2.17). (b) Recovered electronic entropy ΔS_e versus temperature. The dashed lines denote the expected values of entropy for a two-level system ($R \ln 2$) and spin ices.

5.5 Neutron diffraction

Neutron powder-diffraction experiments were carried out on the WOMBAT instrument at ANSTO for our well-characterized isotopically enriched $^{162}\text{Dy}_2\text{Zr}_2\text{O}_7$. The experimental details are outlined in Chapter 3. Figure 5.8(a) shows the magnetic diffraction pattern obtained from the difference of the 40 mK dataset and the 10 K background. We observe that there is no sharp diffraction features and consequently no long-range magnetic order down to 40 mK. The data revealed instead a broad diffuse peak, liquidlike, at $|\mathbf{Q}| = 1.15(7) \text{ \AA}^{-1}$ associated with correlated spins. Figure 5.8(b) shows the data collected at 10 K which display sharp and resolution-limited Bragg peaks due to the crystalline structure. The 10 K dataset was used as a background and subtracted from the lower-temperature spectrum to remove structural contributions and enhance the magnetic data.

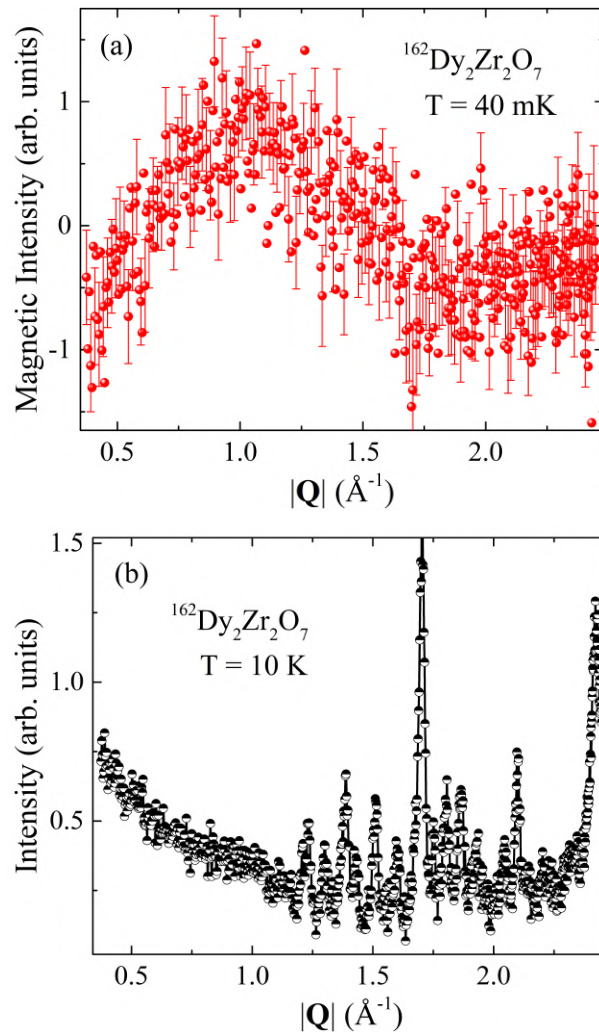


Figure 5.8: (a) Magnetic neutron diffraction for $^{162}\text{Dy}_2\text{Zr}_2\text{O}_7$ measured at 40 mK. (b) Neutron powder diffraction pattern at 10 K displays structural Bragg peaks.

For clarity, a subset of the data is shown in figure 5.9. The broad distribution of diffuse magnetic scattering centered at approximately 1.2 \AA^{-1} is characteristic of antiferromagnetically coupled Ising spins on the corner-sharing tetrahedral lattice [5, 6, 11, 18, 42, 105]. The absence of scattering data near $|\mathbf{Q}| = 0$ is associated to the absence of ferromagnetic correlations and is in agreement with the negative Curie-Weiss temperature obtained from dc magnetization. The data start to increase above 2 \AA^{-1} and appear to reach a second maximum. The net intensity of the data have been corrected for the $|\mathbf{Q}|$ dependence due to the Dy^{3+} magnetic form factor in order to compare models of possible spin structures. To understand the correlations in $\text{Dy}_2\text{Zr}_2\text{O}_7$ further, the first choices are the models for the diffuse scattering of the Dy spin ice and of the highly correlated Tb spin liquid [42]. These models for the analysis of the data were implemented by Jason Gardner coauthor of our work [106]. We plot together the calculated powder-averaged dipolar spin-ice model and that for the near-neighbour antiferromagnetic correlations on the pyrochlore lattice [42]. The latter one so-called Gardner-Berlinsky model has been used to describe the magnetic correlations in the disordered pyrochlore $\text{Tb}_2\text{Hf}_2\text{O}_7$ [18] and first used to model the spin liquid $\text{Tb}_2\text{Ti}_2\text{O}_7$ [42]. Comparing the two models plotted, clearly spin-ice correlations are not present in the $\text{Dy}_2\text{Zr}_2\text{O}_7$ fluorite.

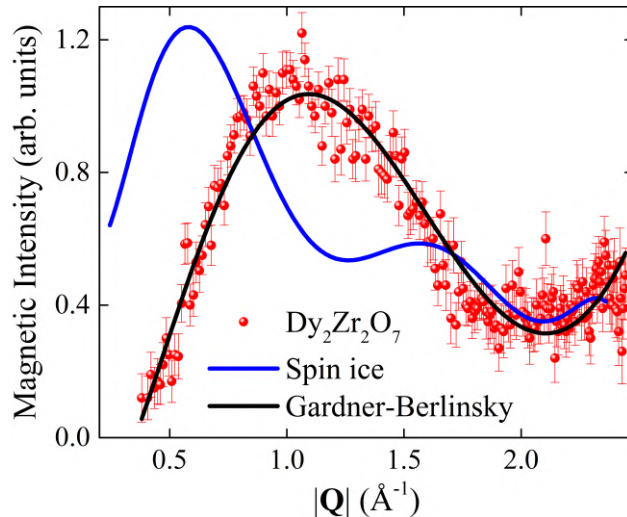


Figure 5.9: Magnetic neutron diffraction for $^{162}\text{Dy}_2\text{Zr}_2\text{O}_7$ at 40 mK. The powder-averaged dipolar spin-ice model and the Gardner-Berlinsky model are plotted.

Now we present the in-field neutron-diffraction dataset for $^{162}\text{Dy}_2\text{Zr}_2\text{O}_7$ at 40 mK which was also subtracted from the background data at 10 K. Figure 5.10(a) shows that in the presence of magnetic field, the shape of the data visibly changed in two aspects.

First, when the applied field is increased strong Bragg peaks are evident at ≈ 2.1 and 2.5 \AA^{-1} . Second, the low-angle broad scattering sharpens up, but remain centered at $|\mathbf{Q}| = 1.2 \text{ \AA}^{-1}$. The two in-field peaks can be indexed to (111) and (200) and associated to a underlying magnetic structure. This development of long-range order occurs after 0.2 T and our data shows that it extends to field values of 5 T. The diffraction data remains the same for fields higher than 3 T with an increasing intensity of the (111) and (200) peaks. Figure 5.10(b) shows in detail the evolution of the low-angle broad peak between 0 and 1.2 T.

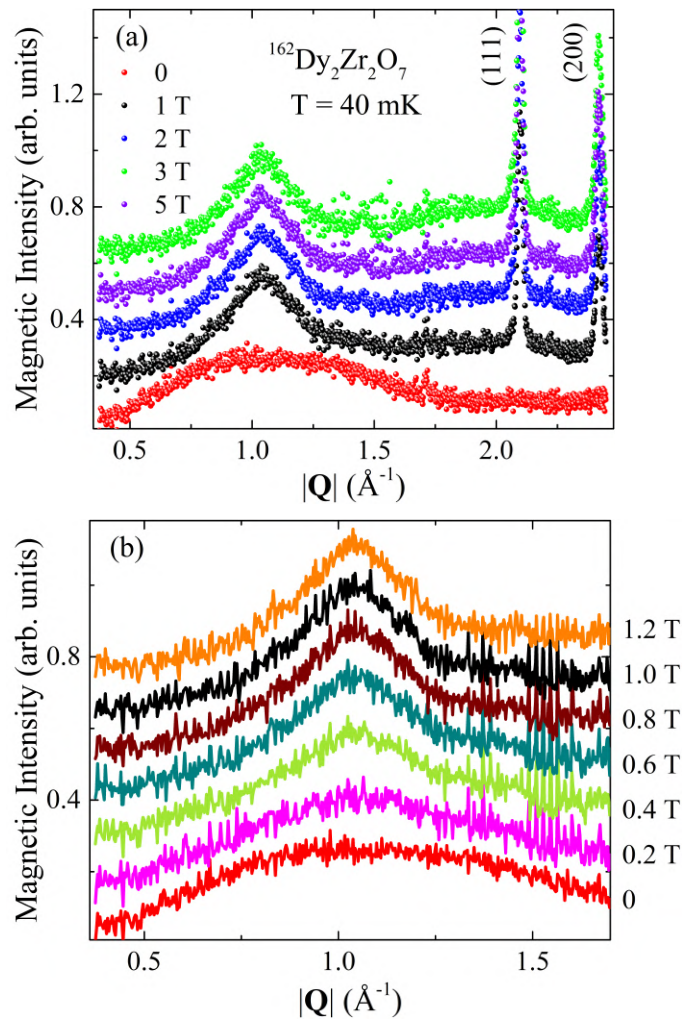


Figure 5.10: (a) Magnetic neutron diffraction for $^{162}\text{Dy}_2\text{Zr}_2\text{O}_7$ at 40 mK in different applied fields. (b) The broad diffraction peak at 1.15 \AA^{-1} for field values up to 1.2 T. The dataset in both panels are offset for clarity.

In order to calculate the mean magnetic correlation length, the peak of antiferromagnetic correlations of wave vector 1.2 \AA^{-1} is fitted to a Gaussian function. The correlation

length is calculated from the full width at half maximum of the broad diffuse scattering, and it is basically the inverse of the peak width $2\pi/|\mathbf{Q}|$. Figure 5.11(a) shows the data and the fits for 0 and 1 T as examples. We plot the correlation length as a function of the applied field figure 5.11(b). The observed short-range spin-spin correlations lengthen in a field, but appear to saturate above 1.5 T. This indicates the existence of a plateau that extends to 5 T but more studies at higher fields are required. Within this field region the correlations extend to $23.6(8)$ Å, the length of approximately six nearest neighbours or five unit cells ($a_0 = 5.24$ Å).

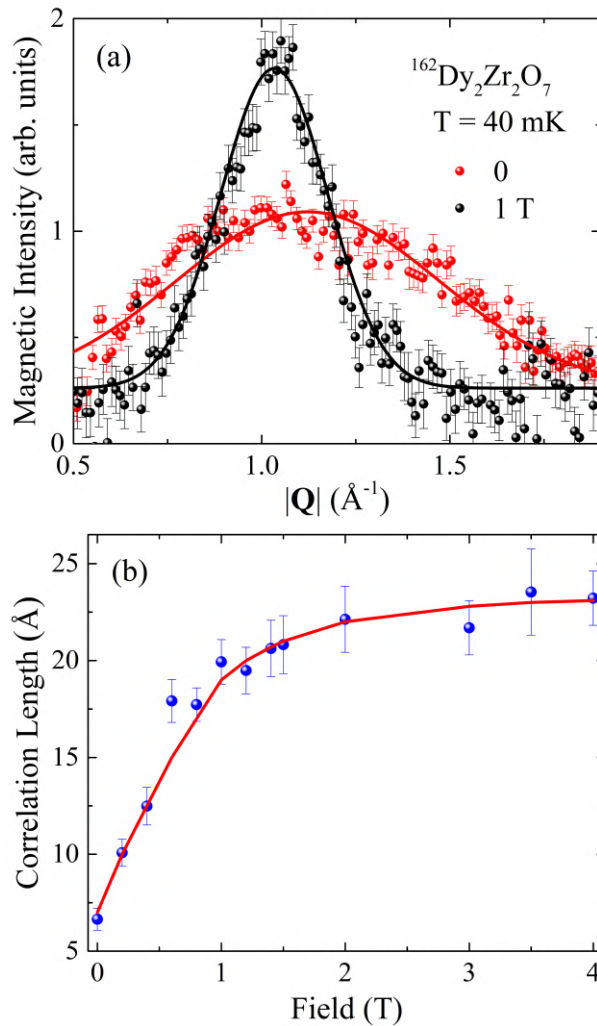


Figure 5.11: (a) Magnetic diffraction at 0 and 1 T plotted with their respective Gaussian fits. (b) Field dependence of the correlation length determined from the Gaussian width of the broad maxima see around 1.2 \AA^{-1} .

5.6 Discussion

The results of the refinement model for the x-ray and neutron diffraction data presented in figure 5.1 show that $\text{Dy}_2\text{Zr}_2\text{O}_7$ and $^{162}\text{Dy}_2\text{Zr}_2\text{O}_7$ possess a disordered fluorite structure. Here, the mixing of the Dy and Zr prevents having the ion Dy^{3+} in all the vertices of a tetrahedron but they are equally distributed.

From our ac magnetic susceptibility measurements, we found that the maxima close to 1.5 K on $\text{Dy}_2\text{Zr}_2\text{O}_7$ is similar in height and shape with the maxima found in $\text{Dy}_2\text{Ti}_2\text{O}_7$ at 2 K. The similarity between $\text{Dy}_2\text{Zr}_2\text{O}_7$ and $\text{Dy}_2\text{Ti}_2\text{O}_7$ in the values of the spin-relaxation time τ extends deep into the spin-ice regime. This behaviour of the time evolution and dynamics found in $\text{Dy}_2\text{Zr}_2\text{O}_7$ is also analogous to that exhibited in the antiferromagnetic Er^{3+} -based spinels, CdEr_2X_4 ($X = \text{Se}, \text{S}$), which has been interpreted as the existence of monopole dynamics [107, 108].

Specific heat measurements show maxima around 1 K for $\text{Dy}_2\text{Zr}_2\text{O}_7$ and $^{162}\text{Dy}_2\text{Zr}_2\text{O}_7$ in agreement with $\text{Dy}_2\text{Ti}_2\text{O}_7$. However, the computed electronic entropy evidences that the fluorites are consistent with a doublet ground state ($R \ln 2$), and they do not present residual entropy at all. This result says that there is no spin ice correlations in the fluorites. The maxima to the electronic specific heat is well described by a doublet ground state as shown in figure 5.7(a). It suggests that the ground state keeps robust even if the lattice is disordered, this doublet is similar to the ground energy levels found in spin-ice $\text{Dy}_2\text{Ti}_2\text{O}_7$ which are smaller in 300 K from the first excited levels.

The observations described for the neutron data including the broad distribution of the magnetic scattering and the absence of ferromagnetic correlations are reminiscent of those from the pyrochlore $\text{Tb}_2\text{Mo}_2\text{O}_7$ [105] in which an antiparallel alignment of adjacent spins is observed on both the R and the M sublattice and the disordered pyrochlore CsNiCrF_6 . At first glance, the data are described well by the GB model; however, the poor statistics makes it difficult to precisely model the high- $|\mathbf{Q}|$ data where the model predicts a second peak closer to 3 \AA^{-1} . More experiments are required to analyse better the diffuse neutron scattering.

Ho₂Zr₂O₇

The following chapter continues our study of the total substitution of Ti by Zr in the pyrochlore spin ices. This significant amount of disorder favours the fluorite structure which with its intrinsic disorder lattice and same $R_2M_2O_7$ composition are modelled to be excellent probes of dynamics in pyrochlores. We perform thermodynamic measurements of the holmium zirconate, Ho₂Zr₂O₇, and discuss its low temperature magnetism. Our results evidence a significant spin dynamics in the order of mK temperatures and an absence of residual entropy; contrary to what it is observed in spin ice Ho₂Ti₂O₇. This behaviour resemblances to that exhibited one in Dy₂Zr₂O₇, which we reported as having no long-ranged order and developing very short antiferromagnetic spin correlations.

6.1 Structural analysis

Literature on the synthesis of rare-earth zirconates, $R_2Zr_2O_7$, has reported that these materials undergo a transition from the disordered fluorite to the pyrochlore structure at temperatures higher than 1400 °C [93,109]. To avoid introducing additional phases, the polycrystalline powder of Ho₂Zr₂O₇ was prepared by using the sol-gel method at different calcination temperatures from 600 to 950°C. Figure 6.1 shows the x-ray powder diffraction patterns at 800, 875, and 950°C as examples. The increasing of the temperature in the synthesis improves vastly the sharp of the Bragg peaks associated to crystallinity of the samples, and also their 2θ positions are similar to ones found in Dy₂Zr₂O₇. By using the Scherrer equation (3.14), we found an increasing in the crystal sizes from 5 to 30 nm for ascendant temperatures of the synthesis. The structural analysis and thermodynamic

experiments above were performed on the $\text{Ho}_2\text{Zr}_2\text{O}_7$ sample synthesized at 900°C which possesses the best sharp peaks on its XPD pattern and higher crystallite size.

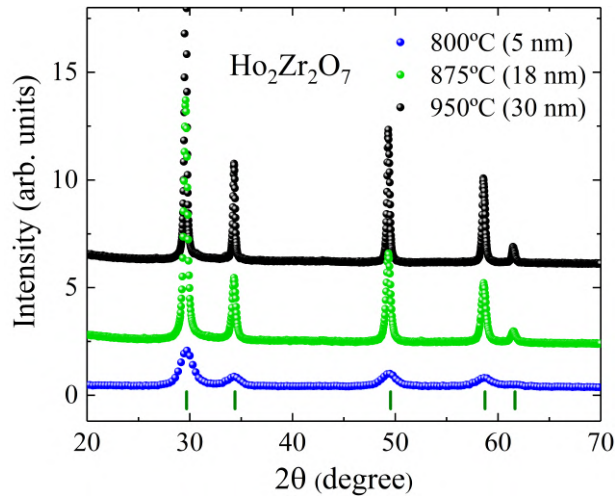


Figure 6.1: X-ray powder diffraction patterns of $\text{Ho}_2\text{Zr}_2\text{O}_7$ synthesized at different temperatures. Vertical lines denote the peaks of the fluorite structure.

By using the Rietveld refinement, an excellent fit was obtained by modelling the data with the fluorite structure and space group, $Fm\bar{3}m$, as shown in figure 6.2. We obtained a goodness-of-fit $\chi^2 = 7.2$ and a weighted R_{wp} -factor = 10. The value of the lattice constant $a_0 = 5.216(2)$ Å is consistent with the reported ones for disordered fluorites [93–95, 106]. We refined the occupations of the ions on the $4a$ and $8c$ Wyckoff positions. The values of the occupations of the Ho and Zr cations are in excellent agreement with half occupancy of the $4a$ site each, excluding the possibility of vacancies on these sites. For the $8c$ site of the O ion, the obtained occupation agrees with the expected value. The $\text{Ho}_2\text{Zr}_2\text{O}_7$ sample is stoichiometric with an experimental error of the occupations smaller than 1%.

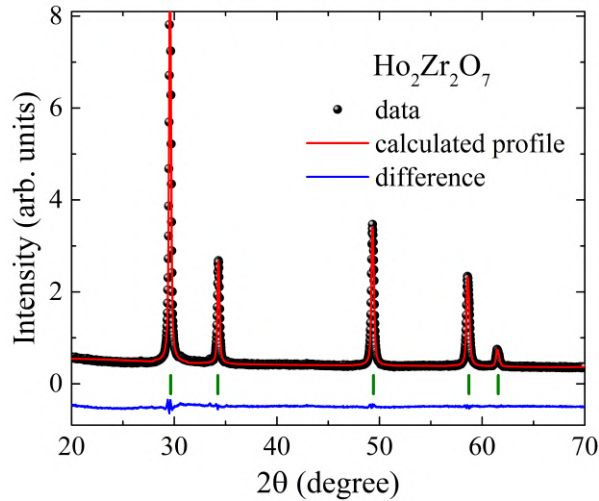


Figure 6.2: X-ray diffraction pattern and calculated profile data for $\text{Ho}_2\text{Zr}_2\text{O}_7$. The difference between the experimental and calculated data is showed in blue. Peak positions of the fluorite structure are marked with small vertical lines.

6.2 DC magnetization

In order to compare the magnetic behaviour of the fluorite $\text{Ho}_2\text{Zr}_2\text{O}_7$ to the spin-ice pyrochlore $\text{Ho}_2\text{Ti}_2\text{O}_7$ followed experiments using a Quantum Design SQUID magnetometer. Results for the inverse of the magnetic susceptibility versus temperature, and the Curie-Weiss fits are shown in figure 6.3(a). Fitting in the linear regime between 10 and 100 K yields an antiferromagnetic Curie-Weiss temperature $\Theta_{\text{CW}} = -2.4$ K for $\text{Ho}_2\text{Zr}_2\text{O}_7$, and a ferromagnetic $\Theta_{\text{CW}} = +0.3$ K for $\text{Ho}_2\text{Ti}_2\text{O}_7$. The effective moments $\mu_{\text{eff}} = 9.2$ and 10.2 μ_B for $\text{Ho}_2\text{Zr}_2\text{O}_7$ and $\text{Ho}_2\text{Ti}_2\text{O}_7$; respectively, compare well to the accepted 10.6 μ_B for free Ho^{3+} ion. For $\text{Ho}_2\text{Zr}_2\text{O}_7$, in the mean-field approximation, the nearest-neighbour exchange interaction is estimated by using $J = 3\Theta_{\text{CW}}/z\mathbf{J}(\mathbf{J} + 1) = 0.02$ K, where $z = 6$ is the number of nearest spin neighbours. For the spin ice $\text{Ho}_2\text{Ti}_2\text{O}_7$, Bramwell *et al.* [45] reported a ferromagnetic $\Theta_{\text{CW}} = +1.9$ K and a effective coupling constant $J = 1.8$ K. Figure 6.3(b) shows the saturation magnetization as a function of the applied field. The saturation moments for both holmium compounds remain closer to 5 μ_B/Ho ion. As reported in [96,110], for the pyrochlores $\text{Ho}_2\text{Ti}_2\text{O}_7$ and $\text{Dy}_2\text{Ti}_2\text{O}_7$ their crystal-field-induced anisotropy reduces the saturation moment to be half the free ion value of 10 μ_B/Ho ion. This same anisotropy could be the case for $\text{Ho}_2\text{Zr}_2\text{O}_7$; however, the moment start to increase for fields higher than 4 T and possibly reaching a different saturation than 5 μ_B/Ho

ion.

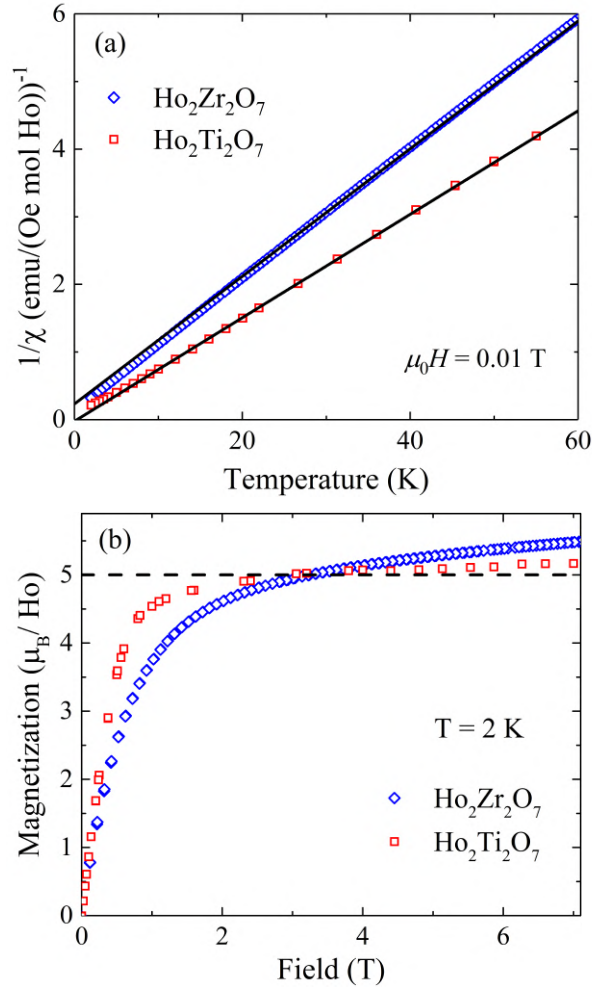


Figure 6.3: (a) Temperature dependence of the inverse susceptibility and Curie–Weiss fits for $\text{Ho}_2\text{Zr}_2\text{O}_7$ and $\text{Ho}_2\text{Ti}_2\text{O}_7$. (b) Saturation magnetization versus the applied magnetic field shows a saturation moment close to $5 \mu_B/\text{Ho}$ ion (dashed line).

6.3 AC magnetic susceptibility

To investigate the dynamic response of $\text{Ho}_2\text{Zr}_2\text{O}_7$, ac susceptibility measurements were performed on an adiabatic demagnetization refrigerator inside a ^4He cryostat down to 50 mK. Figure 6.4 shows the real part of the ac susceptibility, χ'_{ac} , measured at several frequencies and at zero field. The χ'_{ac} values follows a monotonically rising as the temperature is decreased down to $T' \approx 1$ K, where occurs a maximum dependent of the frequency of the measurement. It shares some resemblance in its broad and height features to the maxima of the ac susceptibility curves of $\text{Ho}_2\text{Ti}_2\text{O}_7$, $\text{Dy}_2\text{Zr}_2\text{O}_7$, and $\text{Dy}_2\text{Ti}_2\text{O}_7$ [106, 111, 112]. Similar to what is observed in $\text{Dy}_2\text{Zr}_2\text{O}_7$, the susceptibility of $\text{Ho}_2\text{Zr}_2\text{O}_7$ do not vanish

below 0.5 K revealing an incomplete spin freezing and high spin dynamics again in the disordered fluorites.

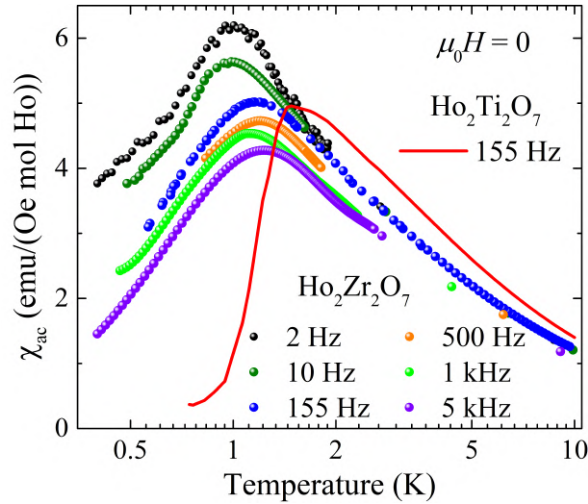


Figure 6.4: Temperature dependence of the real part of the ac susceptibility χ'_{ac} for different frequencies in zero applied field for $\text{Ho}_2\text{Zr}_2\text{O}_7$ and $\text{Ho}_2\text{Ti}_2\text{O}_7$.

Increasing values of the frequency up to 5 kHz causes the maximum close to 1 K shifts toward higher temperatures and becomes broader. The dynamics of $\text{Ho}_2\text{Zr}_2\text{O}_7$ is characterized by fitting the frequency, $f(1/T')$ to an Arrhenius law $f = f_0 \exp(-E_b/k_B T')$, where E_b is the energy barrier. The f and T' data are reported in table 6.1 and we plotted them in figure 6.5. We observed that the Arrhenius law reproduces well the $1/T'$ dependence of the frequency f , and we estimated an energy barrier $E_b = 26$ K, a characteristic frequency $f_0 = 2 \times 10^{11}$ Hz, and a single characteristic relaxation time of $\tau_0 = 1/2\pi f_0 = 8 \times 10^{-13}$ s. Our values are close to the parameters reported in $\text{Ho}_2\text{Ti}_2\text{O}_7$ below 1 K in the spin-ice phase, which are an energy barrier $E_b \approx 28$ K and a relaxation time τ_0 on the order of 2×10^{-14} s [111, 112]. We estimate the frequency shift of the χ'_{ac} maximum per decade frequency $\delta T' = \Delta T' / (T' \Delta \log f)$ which is $\delta T' \approx 0.11$. This parameter is one order of magnitude higher than the reported ones for canonical spin glasses (0.005 – 0.01) [55] indicating a sluggish glass dynamics in $\text{Ho}_2\text{Zr}_2\text{O}_7$.

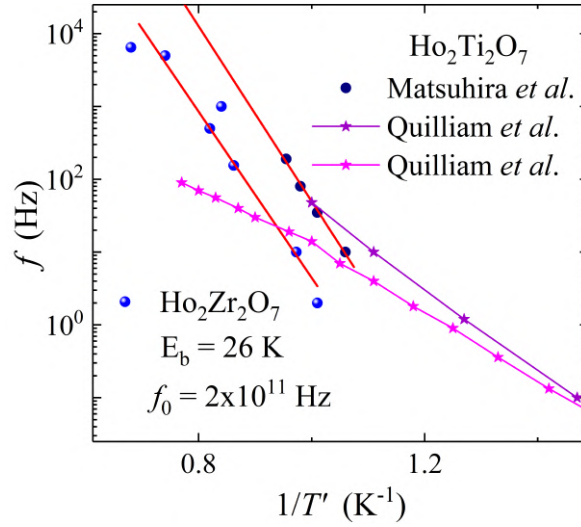


Figure 6.5: Frequency of the measurement (f) versus the inverse of the temperature of the maximum in χ'_{ac} ($1/T'$) with a fit to the Arrhenius law for $\text{Ho}_2\text{Zr}_2\text{O}_7$. Digitalized data of Matsuhira *et al.* [111] and Quilliam *et al.* [112] for $\text{Ho}_2\text{Ti}_2\text{O}_7$ are also displayed.

f (Hz)	T' (K)	$\delta T'$
2^a	0.99^a	0.05^\dagger
10^b	1.028^b	0.11^\ddagger
155^c	1.16^c	0.16^*
500	1.22	–
1000^d	1.19^d	–
5000	1.35	–
6500	1.47	–

Table 6.1: Frequency f , the temperature T' , and the $\delta T'$ values for $\text{Ho}_2\text{Zr}_2\text{O}_7$. \dagger results from the values marked with a and b , \ddagger comes from the values labelled with b and c , and $*$ results from the values marked with c and d .

6.4 Specific heat

The specific-heat data for $\text{Ho}_2\text{Zr}_2\text{O}_7$ was collected using a Quantum Design PPMS calorimeter, operating with a ^3He - ^4He dilution refrigerator insert for the lowest temperatures. Figure 6.6 shows the temperature dependence of the total specific heat, C , down to 150 mK measured at zero field. Experimental data of $\text{Ho}_2\text{Ti}_2\text{O}_7$ taken from Lau *et al.* [30] are also plotted for comparison. The lattice C_p and nuclear C_N contributions are considerable only above 5 K and below approximately 0.5 K, respectively. For $\text{Ho}_2\text{Zr}_2\text{O}_7$, its lattice term C_{p1} was accounted from the measured values of the nonmagnetic $\text{Lu}_2\text{Zr}_2\text{O}_7$, which crystallizes in the fluorite structure. For $\text{Ho}_2\text{Ti}_2\text{O}_7$, its term C_{p2} was obtained from measurements on the pyrochlore $\text{Lu}_2\text{Ti}_2\text{O}_7$. For the two holmium compounds, C_N was estimated as the calculated nuclear specific heat of holmium metal arising from the hyperfine and quadrupolar Hamiltonians of the single isotope of holmium ^{165}Ho ($I = 7/2$) [113,114], as detailed in appendix A. At high and low temperatures, the thermal data of both holmium samples converge to the same temperature dependence. However, between 1 and 10 K there is a noticeable change. The C values of $\text{Ho}_2\text{Zr}_2\text{O}_7$ show no sharp or broad features differing from the shoulder found at about 2 K in the spin ice $\text{Ho}_2\text{Ti}_2\text{O}_7$ [30,45].

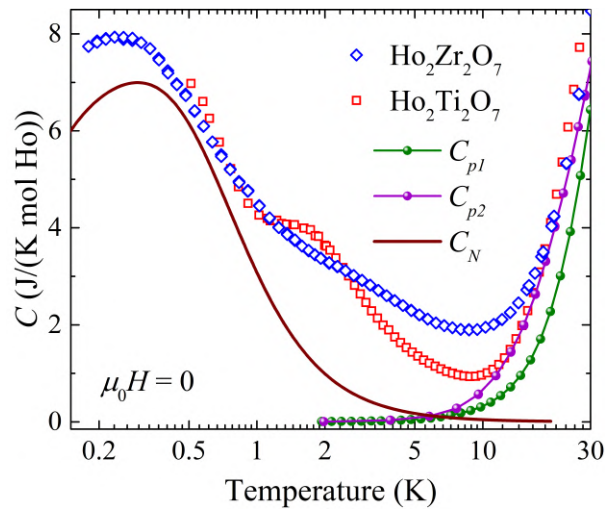


Figure 6.6: Temperature dependence of the total specific heat C of $\text{Ho}_2\text{Zr}_2\text{O}_7$ at zero field. The C data of Lau *et al.* [30] for $\text{Ho}_2\text{Ti}_2\text{O}_7$ are displayed. The specific heat of the isostructural nonmagnetics $\text{Lu}_2\text{Zr}_2\text{O}_7$ (C_{p1}) and $\text{Lu}_2\text{Ti}_2\text{O}_7$ (C_{p2}), and the nuclear specific heat computed as explained in the text are shown.

The electronic magnetic specific heat C_e can be extracted by subtracting the lattice and nuclear contributions to the total specific heat. Figure 6.7(a) shows the C_e values

for both holmium compounds. For $\text{Ho}_2\text{Zr}_2\text{O}_7$, we observed a broad peak at around 3 K. The position, the shape and the width of this peak differs from the typical spin ice shape found in pyrochlores $\text{Ho}_2\text{Ti}_2\text{O}_7$ and $\text{Dy}_2\text{Ti}_2\text{O}_7$, and also is distant from the peak found in our fluorite $\text{Dy}_2\text{Zr}_2\text{O}_7$ (see figure 5.7(a)). We fit the datasets to the two-level Schottky equation (2.17). We found that for $\text{Ho}_2\text{Zr}_2\text{O}_7$ the fit does not reproduce well the data, different from the excellent result obtained on $\text{Ho}_2\text{Ti}_2\text{O}_7$. However, the deduced energy gap values ($\Delta\varepsilon$) from the fit are very close to each other with $\Delta\varepsilon = 6$ and 5 K for $\text{Ho}_2\text{Zr}_2\text{O}_7$ and $\text{Ho}_2\text{Ti}_2\text{O}_7$, respectively. The recovered electronic magnetic entropy $\Delta S_e(T)$ was determined by integrating $C_e(T)/T$ from the lowest measured to the temperature T . Figure 6.7(b) shows the $\Delta S_e(T)$ for $\text{Ho}_2\text{Zr}_2\text{O}_7$ which reach a value of $R \ln 2$ at approximately 15 K as expected for doublet ground states. The ΔS_e values increase rapidly at a high rate above 6 K but this is mainly due to errors introduced by the approximation of the lattice subtraction. In addition, ΔS_e seems not to be fully saturated at 15 K and this suggests the idea of more excited levels in play at this temperature regime. For $\text{Ho}_2\text{Zr}_2\text{O}_7$, our data show once again that there is no residual entropy left as T goes to zero as we reported first for $\text{Dy}_2\text{Zr}_2\text{O}_7$. This result differs totally from the Pauling entropy found in pyrochlore spin ices $\text{Ho}_2\text{Ti}_2\text{O}_7$ and $\text{Dy}_2\text{Ti}_2\text{O}_7$.

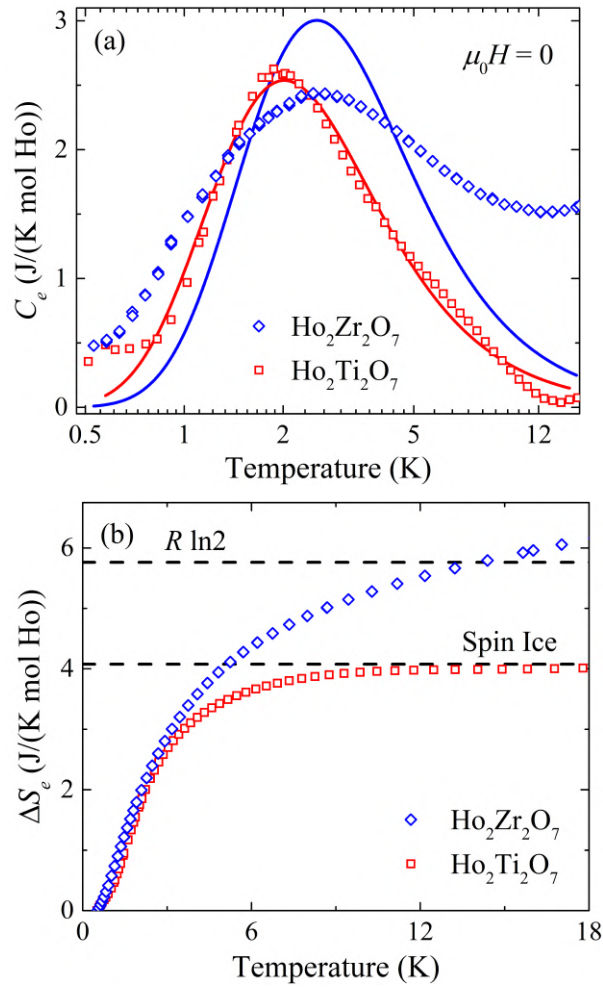


Figure 6.7: (a) The electronic specific heat C_e versus temperature of $\text{Ho}_2\text{Zr}_2\text{O}_7$ at zero field. The C_e values of $\text{Ho}_2\text{Ti}_2\text{O}_7$ were obtained by subtracting C_{p2} and C_N to the dataset of Lau *et al.* [30]. The two-level Schottky fits using equation (2.17) are shown as solid lines. (b) The electronic magnetic entropy ΔS_e versus temperature. The dashed lines denote $R \ln 2$ for a two-level spin system and the presence of residual entropy for spin ices.

In-field specific-heat experiments were performed for $\text{Ho}_2\text{Zr}_2\text{O}_7$, and results are shown in figure 6.8(a). We observe that the application of a magnetic field causes the merging of a peak at about 2.5 K which is absent in zero field. As the intensity of the field is increased further, this single peak shifts to higher temperature and around 1 T the peak becomes visible and much broader in temperature. By using the two-level Schottky equation to fit the in-field C_e , we found a description that lacks of reproducing the broad feature of the peaks, as shown in figure 6.8(b). The obtained gaps $\Delta\varepsilon$ show a linear dependence with the applied field H which follows the Zeeman separation $\Delta\varepsilon = (g\mu_B/k_B)H$ for spin

$S = 1/2$, as seen in 6.8(c). We found a value for the g -factor of 6.8(1) smaller than the factor along the local $\langle 111 \rangle$ axis $g_{\parallel} = 19.6$ reported for $\text{Ho}_2\text{Ti}_2\text{O}_7$ by Bertin *et al.* [23].

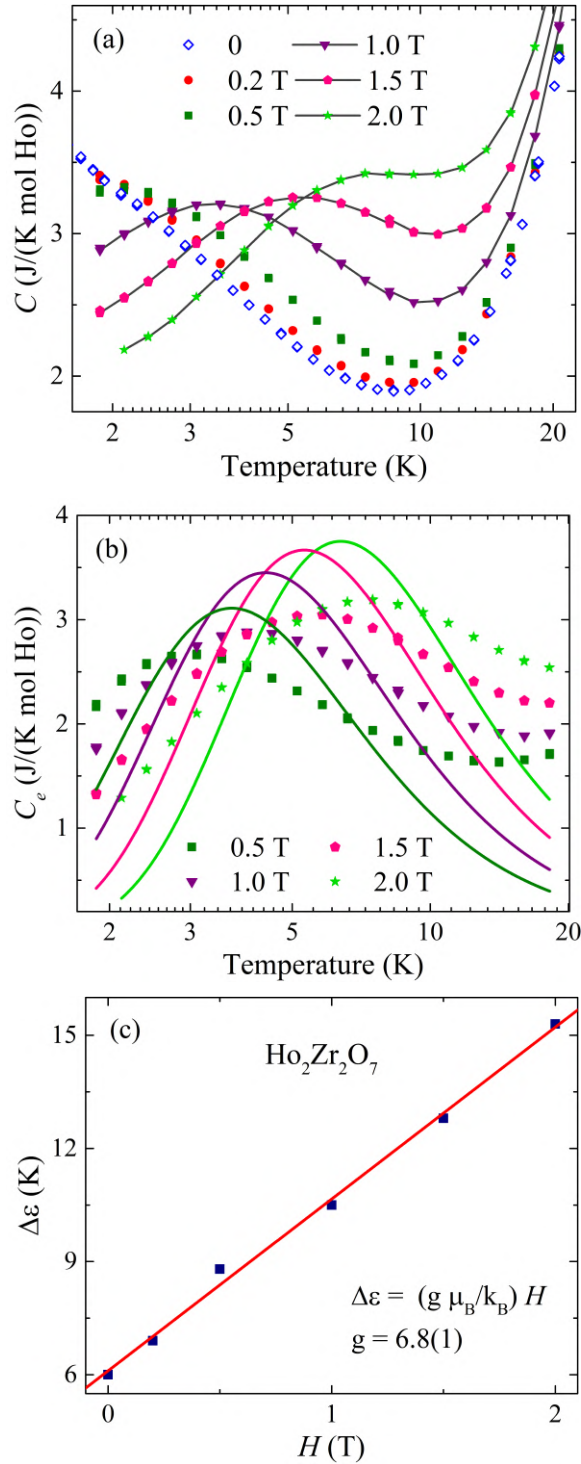


Figure 6.8: (a) The temperature dependence of C for $\text{Ho}_2\text{Zr}_2\text{O}_7$ in different applied magnetic fields. Gray solid lines are guides to the eyes. (b) The C_e curves versus temperature and their respective two-level Schottky fits using equation (2.17), shown as solid lines. (c) The linear dependence of the energy gaps $\Delta\varepsilon$ as a function of the applied field H .

6.5 Discussion

Our results show that the recovered entropy in the disordered fluorite $\text{Ho}_2\text{Zr}_2\text{O}_7$ reach a value of $R \ln 2$ corresponding to ground–state doublet. The application of a field open this doublet with a factor $g = 6.8$ which is much smaller than the $g_{\parallel} = 19.6$ along the Ising axis in $\text{Ho}_2\text{Ti}_2\text{O}_7$ [23]. This allows us to recognize a type of anisotropy in $\text{Ho}_2\text{Zr}_2\text{O}_7$ that diverge from the pure Ising of spin ices. Surprisingly, the g –factor is close to the planar g_{\perp} –factor of $\text{Er}_2\text{Ti}_2\text{O}_7$ (7.7) which present a strong XY anisotropy. These considerations suggest in $\text{Ho}_2\text{Zr}_2\text{O}_7$ a low–temperature ground–state doublet with non Ising anisotropy.

A rough schema of the CEF in $\text{Ho}_2\text{Zr}_2\text{O}_7$ can be thought if we compare it to the one of $\text{Er}_2\text{Ti}_2\text{O}_7$. By looking at the recovered entropy above 15 K, we found values that continue increasing above $R \ln 2$ just as reported in $\text{Er}_2\text{Ti}_2\text{O}_7$ [31] which also possesses a doublet state. The values higher than $R \ln 2$ can be associated to excited CEF levels as reported similarly to $\text{Er}_2\text{Ti}_2\text{O}_7$ with excited levels around 80 K by Dalmas *et al.* [31]. Also, the CEF energy schema of $\text{Er}_2\text{Ti}_2\text{O}_7$ presents energy levels less spaced and of an order of magnitude lower than the 300 K of spin ices $\text{Ho}_2\text{Ti}_2\text{O}_7$ and $\text{Dy}_2\text{Ti}_2\text{O}_7$ [23, 115]. Due to the possible XY anisotropy in $\text{Ho}_2\text{Zr}_2\text{O}_7$, we could suggest a picture of its first excited CEF levels as closer ones to each other and with energy scales lower than spin ices.

Tb₂Zr₂O₇

In this chapter we discuss the structural and thermomagnetic measurements of the terbium zirconate Tb₂Zr₂O₇. Even though there is an extensive disorder on the lattice of Tb₂Zr₂O₇, it still provides valuable insights when compared with the classical spin liquid Tb₂Ti₂O₇. We observe thermodynamic similarities as the dominant antiferromagnetic interactions, the glassy character of its spin dynamics, the presence of fluctuations on the electronic magnetic moment of Tb, and the convergence of the recovered entropy to $R \ln 4$. Our results suggest a form of collective spin-glass-type behaviour in which it is induced a slow spin relaxation.

7.1 Structural analysis

Polycrystalline powder samples of Tb₂Zr₂O₇ were prepared at different temperatures from 600 to 950°C by using the sol-gel method. Figure 7.1 shows the x-ray powder diffraction spectra for the Tb₂Zr₂O₇ samples synthesized at 800°C, 875°C, and 950°C as examples. The increasing of the temperature in the synthesis improves the crystallinity of the samples and their crystal size from 6 to 21 nm, as estimated from the Scherrer equation (3.14). Our experimental study and results above were carried on the Tb₂Zr₂O₇ sample synthesized at 950°C which possesses the sharpest Bragg peaks and larger crystal size.

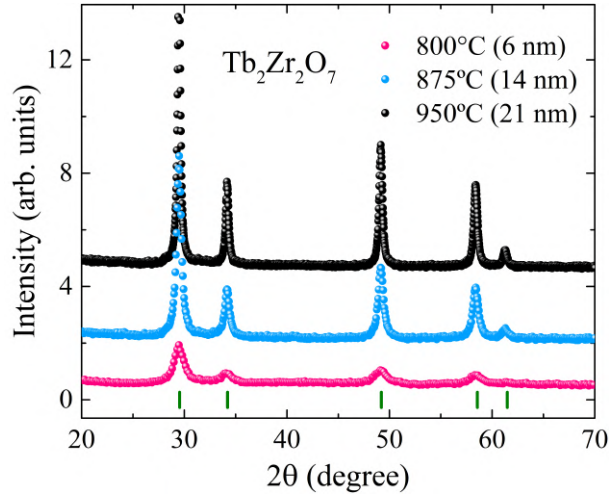


Figure 7.1: X-ray powder diffraction for heat-treated samples of $\text{Tb}_2\text{Zr}_2\text{O}_7$ at different temperatures.

The Rietveld refinement of the x-ray data with the fluorite structure and space group, $Fm\bar{3}m$, resulted in an excellent fit as shown in figure 7.2. The lattice constant $a_0 = 5.232(2)$ Å is consistent with the values of $\text{Ho}_2\text{Zr}_2\text{O}_7$ and $\text{Dy}_2\text{Zr}_2\text{O}_7$ [106]. The defect-fluorite structure has one cation site ($4a$) and one oxygen site ($8c$) that is $7/8$ occupied. The attempt to refine the degree of Tb/Zr occupancies of the $4a$ site results in values of 50% of occupancy for each cation. The oxygen content found excludes the possibility of vacancies on the $8c$ site. From the refinement, our $\text{Tb}_2\text{Zr}_2\text{O}_7$ sample is stoichiometric to within the experimental error of 1%. The different environment surrounding Tb in fluorites causes; specially at low temperatures, that its single-ion magnetic properties are expected to change in $\text{Tb}_2\text{Zr}_2\text{O}_7$ when compared to Tb in $\text{Tb}_2\text{Ti}_2\text{O}_7$, in which the CEF levels are ruled by two non-Kramers doublets [23, 116].

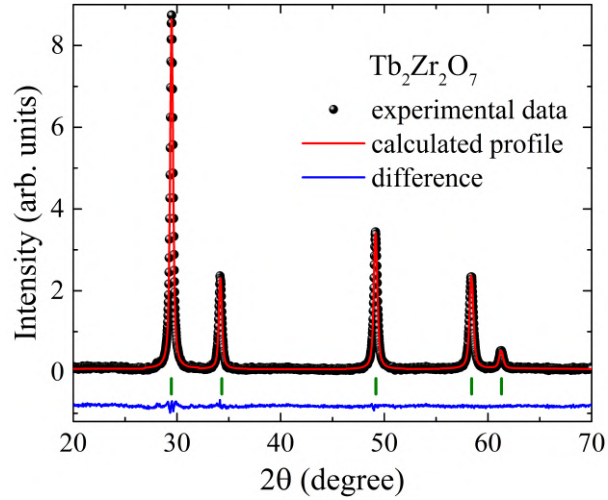


Figure 7.2: X-ray diffraction pattern and calculated profile data for $\text{Tb}_2\text{Zr}_2\text{O}_7$. The difference between the experimental and calculated data is showed in blue. Peak positions of the fluorite structure are marked with small vertical lines.

7.2 DC magnetization

The inverse of the measured magnetic susceptibility versus temperature, and the Curie-Weiss fit of the data for $\text{Tb}_2\text{Zr}_2\text{O}_7$ are shown in figure 7.3(a). The linear fit above 10 K yields negative Curie-Weiss temperatures, $\Theta_{\text{CW}} = -15$ K, close to the reported value of -19 K for $\text{Tb}_2\text{Ti}_2\text{O}_7$ [21], indicating the dominance of antiferromagnetic interactions. The effective magnetic moment $\mu_{\text{eff}} = 9 \mu_B$ is also in agreement to the expected $9.6 \mu_B$ for free Tb^{3+} ion. We observe a slight deviation from the Curie-Weiss law close to 50 K which could be associated to short-range magnetic correlations similar to the ones present up to this temperature in $\text{Tb}_2\text{Ti}_2\text{O}_7$ [5]. Figure 7.3(b) shows the saturation magnetization as a function of the applied field at the temperature $T = 2$ K. The saturation moment for $\text{Tb}_2\text{Zr}_2\text{O}_7$ reaches $5 \mu_B/\text{Tb}$ ion at 7 T, consistent with measurements in $\text{Tb}_2\text{Ti}_2\text{O}_7$ [117], and correspond to the predicted ground state moment for the Tb^{3+} ion [21].

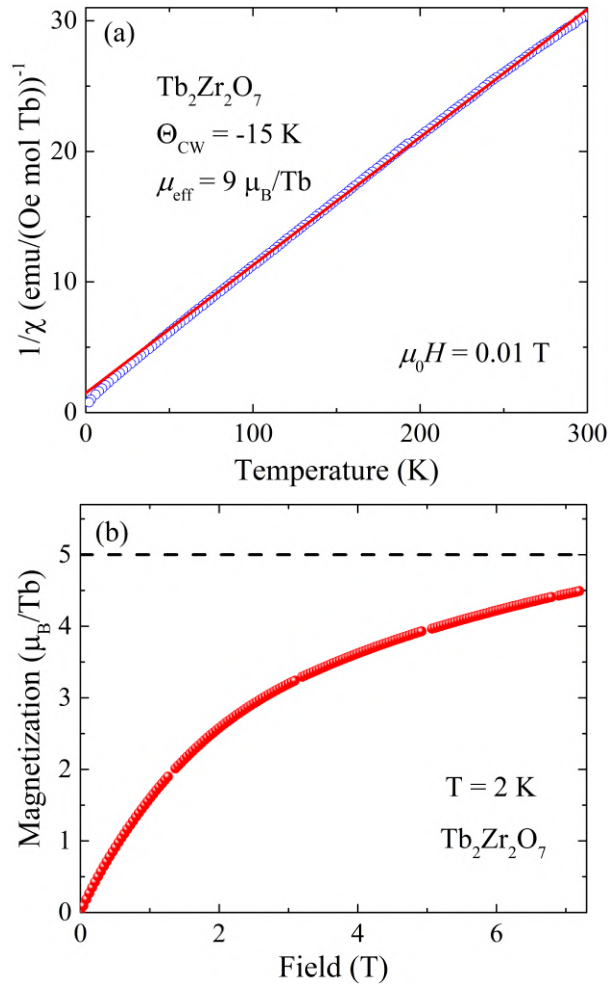


Figure 7.3: (a) Temperature dependence of the inverse susceptibility and Curie–Weiss fit for $\text{Tb}_2\text{Zr}_2\text{O}_7$. (b) Saturation magnetization versus the applied magnetic field for $\text{Tb}_2\text{Zr}_2\text{O}_7$ shows a saturation moment close to $5 \mu_{\text{B}}/\text{Tb}$ ion.

7.3 AC magnetic susceptibility

AC susceptibility experiments were carried out for $\text{Tb}_2\text{Zr}_2\text{O}_7$ on an Physical Property Measurement System of the Quantum Design using its ac susceptometer option down to 2 K. Below 2 K, the ac magnetic susceptibility χ_{ac} was measured on a home-made ac susceptometer using a mutual inductance bridge at the single frequency of 155 Hz and modulation field of 0.5 Oe. Figure 7.4 shows both real χ'_{ac} and imaginary χ''_{ac} parts of the susceptibility versus temperature in zero magnetic field. At 155 Hz, our data reveal a broad maximum at $T' \approx 2.5 \text{ K}$, with values of χ'_{ac} that decrease monotonically but do not zero below 0.7 K suggesting a slowing down of spin dynamics. The maximum occurs at a temperature of one order of magnitude higher than the glassy-like transition at about 0.25

K reported for the pyrochlore $\text{Tb}_2\text{Ti}_2\text{O}_7$ [6, 54]. The maxima in χ'_{ac} and χ''_{ac} coincide on their temperature positions. Both present a non-negligible shift to higher temperatures with increasing frequency which is a recognizable feature of a spin-glass transition [55]. The χ''_{ac} curves display two different regime below and above 2 kHz (curved dashed arrow), and they also present long tails going to zero values of susceptibility at temperatures above 3 K different from the real part of the χ_{ac} curves.

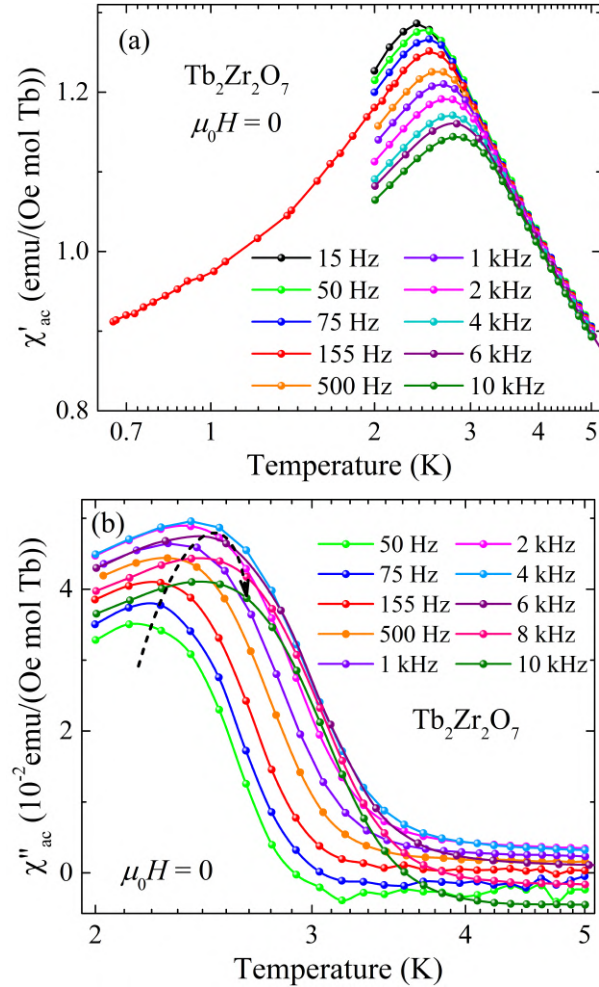


Figure 7.4: (a) Real Part of the ac susceptibility χ'_{ac} as a function of the temperature in zero magnetic field for $\text{Tb}_2\text{Zr}_2\text{O}_7$. (b) Imaginary Part of the ac susceptibility χ''_{ac} as a function of the temperature in zero magnetic field for $\text{Tb}_2\text{Zr}_2\text{O}_7$.

The analysis of the frequency-dependent shift of the χ'_{ac} maximum was attempted as estimated for canonical spin glasses. By using the values of table 7.1, the maximum shift per decade of frequency $\delta T' = \Delta T' / (T' \Delta \log f) = 0.064$ for our fluorite $\text{Tb}_2\text{Zr}_2\text{O}_7$. This value is similar to the $\delta T'$ found in terbium pyrochlores such as $\text{Tb}_2\text{Ti}_2\text{O}_7$ and $\text{Tb}_2\text{Hf}_2\text{O}_7$, with both values around 0.06 [117, 118], and to the ones reported for typical spin glasses

$(\delta T' = 0.005 - 0.01)$ [55].

f (Hz)	T' (K)	$\delta T'$
15 ^a	2.4 ^a	0.062 [†]
75	2.51	–
155 ^b	2.55 ^b	0.063 [‡]
500	2.63	–
1000 ^c	2.68 ^c	0.067 [*]
2000	2.73	–
4000	2.78	–
6000	2.82	–
10000 ^d	2.86 ^d	–

Table 7.1: Frequency f , the temperature T' , and the $\delta T'$ values for $\text{Tb}_2\text{Zr}_2\text{O}_7$. † results from the values marked with a and b , ‡ comes from the values labelled with b and c , * results from the values marked with c and d .

Figure 7.5(a) shows the Arrhenius law $f = f_0 \exp(-E_b/T')$ used to describe a thermally activated process with a single energy barrier E_b . According to Mydosh [55], this frequency dependence of the χ'_{ac} maximum is not followed by canonical spin glasses and fits to the data return unphysical values. We obtained an energy barrier $E_b = 98$ K, a characteristic frequency $f_0 = 10^{19}$ Hz, and a single characteristic relaxation time of $\tau_0 = 1/2\pi f_0 = 2 \times 10^{-20}$ s. Even though the fit reproduces well the data, the obtained frequency value is unphysical favouring the spin-glass behaviour in $\text{Tb}_2\text{Zr}_2\text{O}_7$.

In spin glasses, a first model used to describe the f dependence of the χ'_{ac} cusp is the dynamic scaling law or power-law divergence of the critical slowing down $\tau = \tau_0 ((T' - T_c)/T_c)^{-zv}$, where τ is the relaxation time and T_c is the peak position as $f \rightarrow 0$ which was approximated as 2.2 K. By fitting the data of $\ln \tau$ to this model, as seen in figure 7.5(b). We determined the values of $\tau_0 = 2 \times 10^{-8}$ s and $zv = 5.8$, with the latter one in agreement with spin glasses ($zv = 4 - 12$) [55]. The second model employed is the phenomenological Vogel-Fulcher law $\tau = \tau_0 \exp[-E/(T' - T_0)]$. Results from the fit to the data are shown in figure 7.5(c). We obtained the values $\tau_0 = 1 \times 10^{-10}$ s, $E = 15.8$ K and $T_0 = 1.6$ K. This value of T_0 is smaller than $T' \approx 2.5$ K, different to the expected

$T_0 \approx T'$ for canonical spin glasses [55]. Both models result in excellent fits of the τ values suggesting the presence of a spin-glass state.

Following the same study for the glassy behaviour reported in $\text{Tb}_2\text{Ti}_2\text{O}_7$ [117], the f dependence of T' was analysed by a power law of the Arrhenius relation $\tau = \tau_0 \exp [(-E/T')^\sigma]$. The fit provides an excellent description of the data, as displayed in figure 7.5(d). The fit results in values of $\tau_0 = 1 \times 10^{-10}$ s, $E = 7.8$ K and $\sigma = 2.5$. For $\text{Tb}_2\text{Ti}_2\text{O}_7$, such law yielded $\tau_0 = 1.1 \times 10^{-9}$ s, $E = 0.91$ K and $\sigma = 2$.

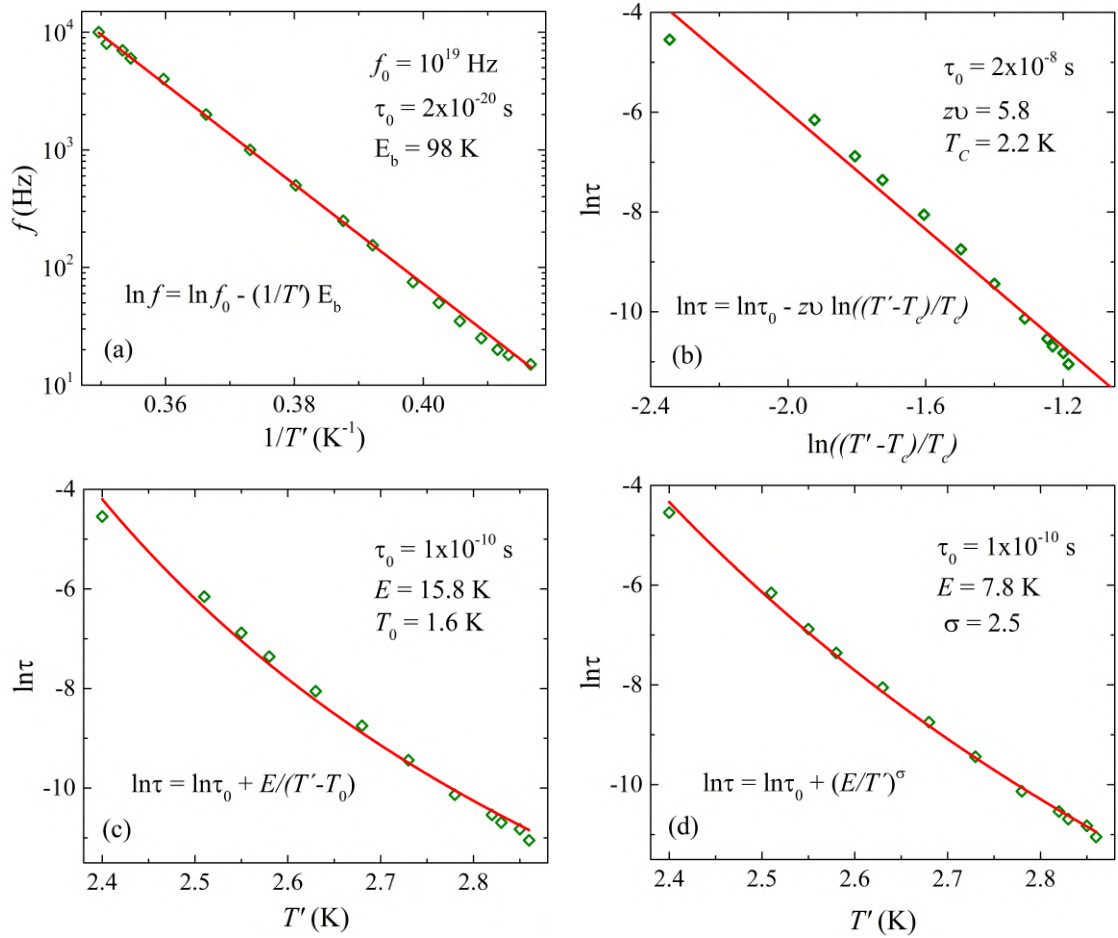


Figure 7.5: (a) Frequency of the measurement (f) versus the inverse of the temperature of the maximum in χ'_{ac} ($1/T'$) with a fit to the Arrhenius law. Logarithmic spin-relaxation time ($\ln \tau$) fitted to the dynamic scaling law (b), to the Vogel-Fulcher law (c) and to the equation $\tau = \tau_0 \exp [(-E/T')^\sigma]$ (d).

In figure 7.6 we show the real part χ'_{ac} of the ac susceptibility at 1 kHz and 10 kHz frequencies in presence of different magnetic fields. We observe a peak at ≈ 25 K in χ'_{ac} for fields $\mu_0 H > 5$ T, which shifts to higher temperatures with increasing field. This in-field peak is due to the saturation of the magnetic moment of Tb^{3+} which causes that the susceptibility associated with spin fluctuations must approach to zero at high temperatures and as we reach 0 K in the presence of a strong enough field. The data appears to exhibit a very slight frequency dependence at the 25 K peak suggesting a unusual slow spin relaxation character similar to $\text{Tb}_2\text{Ti}_2\text{O}_7$ [51]. The in-field data of the imaginary part χ''_{ac} (not shown) is too noisy to be discussed.

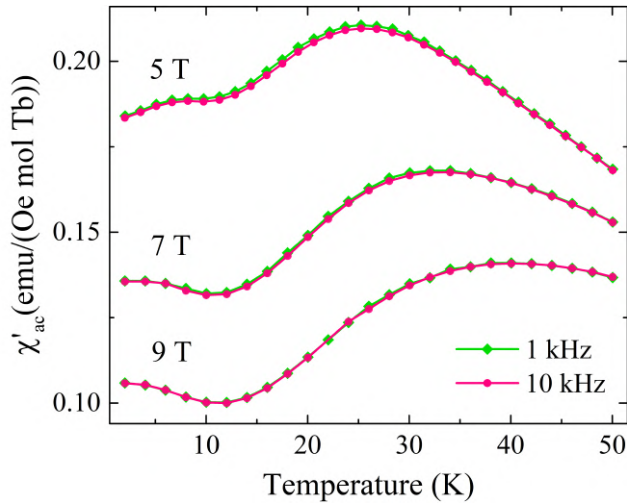


Figure 7.6: The temperature dependence of χ'_{ac} for $\text{Tb}_2\text{Zr}_2\text{O}_7$ at different frequencies in various applied fields.

7.4 Specific heat

Specific heat experiments were performed on the defect-fluorite $\text{Tb}_2\text{Zr}_2\text{O}_7$ using a Quantum Design PPMS calorimeter and its ^3He - ^4He dilution-refrigerator option. Figure 7.7 shows the temperature dependence of the total specific heat, C , measured in zero magnetic field. The data does not display sharp features that would arise from a long-range ordering but exhibit a broad peak centered at about 5 K similar to the one observed in $\text{Tb}_2\text{Ti}_2\text{O}_7$ [21, 54]. There are also two maxima at temperatures around 0.4 and 1 K reported for the pyrochlore [21, 54] that are absent for our fluorite. The upturn of C below 0.5 K is attributed to the nuclear specific heat C_N . It was accounted for by calculating the nuclear specific heat of terbium metal (C_{TbMet}) with its nuclear spin $I = 3/2$ of the

isotope ^{159}Tb , hyperfine constant $a = 0.15$ K and quadrupole coupling constant $P = 0.021$ K [119] (see Appendix A). For avoiding inconsistent results, we use the reduced nuclear specific heat $C_N = f \times C_{\text{TbMet}}$ ($f = 0.6$), as we explained below in the text. The lattice term C_p was approximated by measuring the specific heat of the nonmagnetic fluorite $\text{Lu}_2\text{Zr}_2\text{O}_7$.

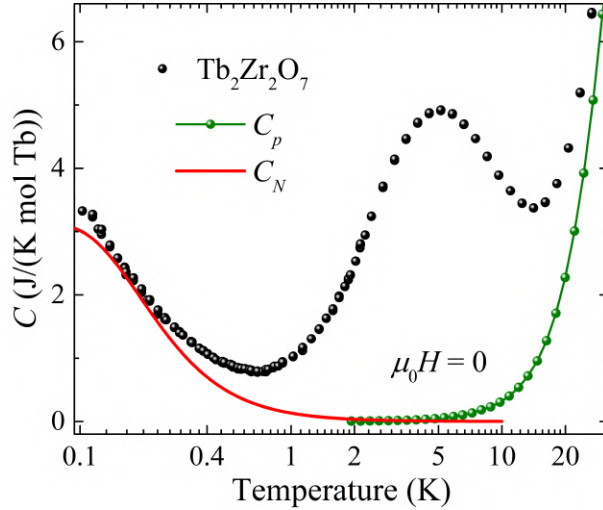


Figure 7.7: Specific heat C as a function of temperature for $\text{Tb}_2\text{Zr}_2\text{O}_7$ in zero field. The specific heat of the isostructural nonmagnetic $\text{Lu}_2\text{Zr}_2\text{O}_7$ (C_p) and the computed nuclear specific heat (C_N) are displayed.

Now we detail our considerations employed in the analysis of the low-temperature region of the data. In figure 7.8 we plotted the computed values for the metallic Tb (C_{TbMet}) and two estimations for the nuclear specific heat (C_N and C_{N1}). Clearly, C_{TbMet} is not suitable for our approximation since it has higher values than our data below 0.5 K and a predicted height maximum of around 5 ($\text{J}/(\text{K mol Tb})$). The nuclear specific heat $C_N = f \times C_{\text{TbMet}}$; where f is a reduction factor, overcome this inconsistency. The value of f is less than one and represents the fraction of Tb spins with full magnetic moment ($\mu_{\text{Tb}} = 10 \mu_B$). This method has been successfully employed in thermal analyses for praseodymium pyrochlores in the literature [16, 120]. The second estimation for the nuclear term (C_{N1}) was done for reduced magnetic moments of $0.55\mu_{\text{Tb}}$ (see Appendix A). This reduction is due to electronic magnetic moments smaller than the saturated value are acting on the nuclear moments reflecting spin fluctuations [121, 122]. We chose C_N since it converges exactly to the C values below 0.2 K and because its predicted peak appears to be below the data. We also show the specific heat of the hydroxide $\text{Tb}(\text{OH})_3$ [123] for

which its nuclear term becomes prevalent below 0.5 K as in our fluorite compound case. However, we did not use it for being larger than the experimental points.

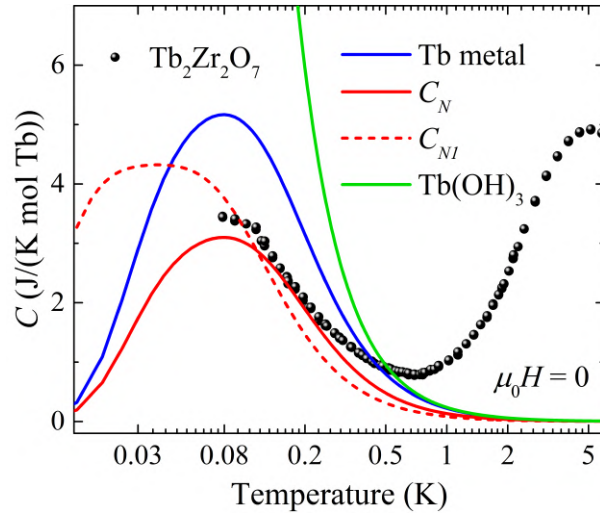


Figure 7.8: Specific heat C versus temperature for $\text{Tb}_2\text{Zr}_2\text{O}_7$ in the low-temperature regime. The estimations for the specific heat C_{TbMet} and nuclear contributions C_N and C_{N1} are displayed. We show for comparison the nuclear term of the compound $\text{Tb}(\text{OH})_3$.

In figure 7.9(a) we plot the electronic specific heat C_e for $\text{Tb}_2\text{Zr}_2\text{O}_7$ obtained from subtracting the lattice and nuclear contributions to the total specific heat. We also display the Schottky fit for a two-level system which approximates reasonably the width and the position of the peak. At zero field, the obtained energy gap $\Delta\varepsilon = 10.3$ K is of the same order of magnitude compared with the gap between the two non-Kramers doublets separated 17 K in $\text{Tb}_2\text{Ti}_2\text{O}_7$ [5, 21, 23]. The recovered electronic magnetic entropy $\Delta S_e(T)$ was determined by integrating $C_e(T)/T$ from the minimum measured to the temperature T . Figure 7.9(b) shows that the value of $\Delta S_e(T)$ at zero field is close to $R \ln 4$ at approximately 18 K, as reported for $\text{Tb}_2\text{Ti}_2\text{O}_7$ and associated to the doublets of the two lowest energy levels [21, 54].

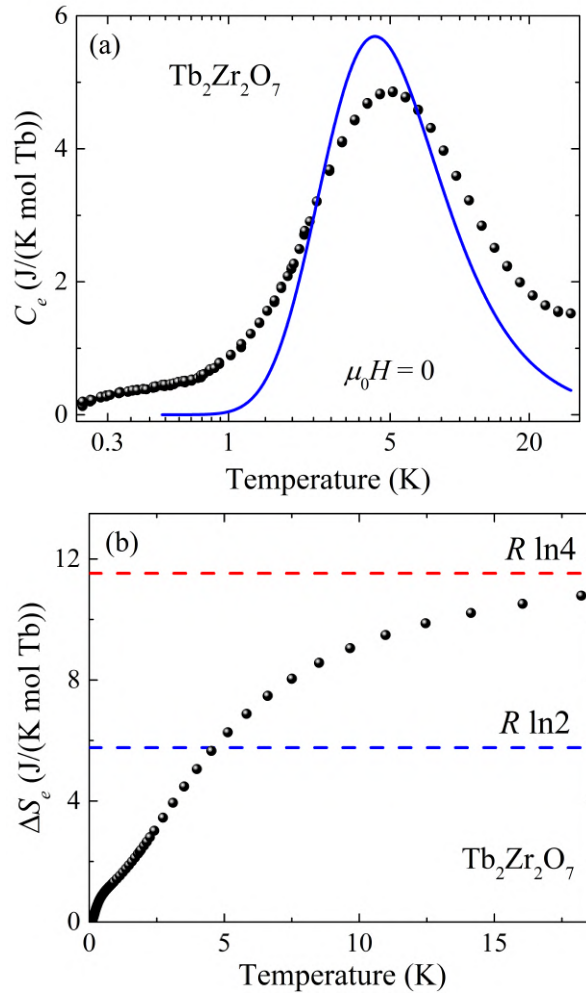


Figure 7.9: (a) The electronic specific heat $C_e(T)$ of $\text{Tb}_2\text{Zr}_2\text{O}_7$ at zero field and the two-level Schottky fit using equation (2.17) (solid line). (b) The electronic magnetic entropy $\Delta S_e(T)$ for $\text{Tb}_2\text{Zr}_2\text{O}_7$. The dashed lines denote the entropy for a two level system ($R \ln 2$) and the entropy reported for $\text{Tb}_2\text{Ti}_2\text{O}_7$ ($R \ln 4$) [21, 54].

In-field specific-heat experiments were performed for $\text{Tb}_2\text{Zr}_2\text{O}_7$, and results are shown in figure 7.10(a). The application of a magnetic field causes the single peak shifts to higher temperatures, and around a 3.5 T field the peak becomes much broader in temperature. Using the two-level Schottky equation to model the in-field C_e data reproduced fairly datasets below and above the maxima, as shown in figure 7.10(b); however, the amplitude of the maxima cannot be reached by this equation. Figure 7.10(c) shows the linear dependence of the energy gap with the applied magnetic field (H). The data was fitted using the expression for the Zeeman separation $\Delta\varepsilon = (g\mu_B/k_B)H$ for an effective spin $S = 1/2$, where the g -factor is a fitting parameter. The obtained $g = 2.3(1)$ is almost a quarter of the factor parallel to the $\langle 111 \rangle$ direction $g_{\parallel} = 9.6$ found in $\text{Tb}_2\text{Ti}_2\text{O}_7$ [23].

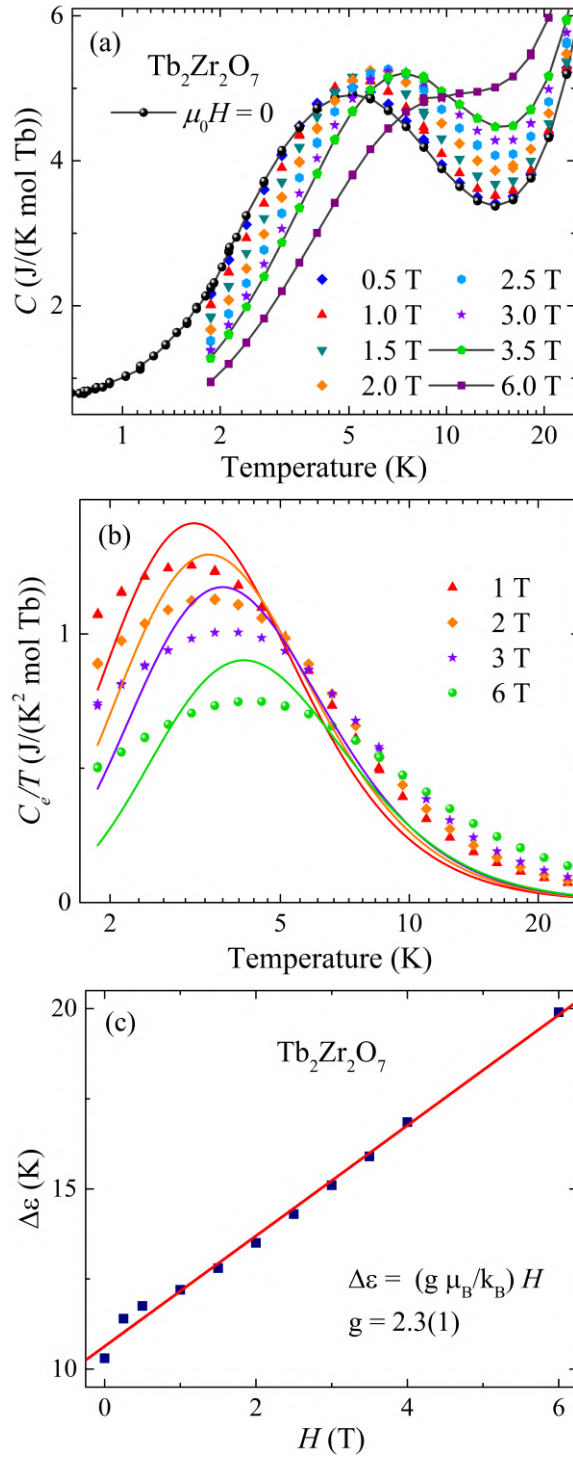


Figure 7.10: (a) The total specific heat $C(T)$ for $\text{Tb}_2\text{Zr}_2\text{O}_7$ in different applied magnetic fields. Gray solid lines are guides to the eyes. (b) The electronic specific heat $C_e(T)$ in fields up to 6 T. Solid lines are the two-level Schottky fits using equation 2.17. (c) Gap values $\Delta\varepsilon$ determined from the Schottky fit as a function of the applied field H .

7.5 Discussion

In the disordered fluorite $\text{Tb}_2\text{Zr}_2\text{O}_7$, we found that the cations of Tb and Zr are well mixed on the $4a$ site each one with a 50 % of occupancy. In this structure, the oxygen ions form a perfect cube around the $4a$ site with an average local coordination of 7. If compared to the pyrochlore $\text{Tb}_2\text{Ti}_2\text{O}_7$, the change in the local environment of the Tb should result in a strong modification to the CEF levels; affecting their local magnetism. Then, we could gain some important insights about the CEF of $\text{Tb}_2\text{Zr}_2\text{O}_7$ if we look at a compound with similar neighbourhood around Tb. For example, for the non-Kramer $\text{Tb}_2\text{Hf}_2\text{O}_7$ is found a phase at the boundary of the pyrochlore/defect-fluorite structures [18, 118]. Its unit cell has been reported as a perfect arrangement of the Tb cations in a pyrochlore lattice together with a considerable number of oxygen Frenkel pair defects [18]. The local defects are described by an empty site ($48f$) and an interstitial oxygen ($8a$). Due to the presence of the Frenkel defect, the neighbour environment of Tb has an oxygen coordination of seven [18]. This occurs for around 50 % of the Tb cations randomly in the lattice [18]. In the fluorite, the Tb/Zr tetrahedra still exist, even though disordered. The oxygen coordination around Tb, the tetrahedral arrangement on the lattices and the disorder for $\text{Tb}_2\text{Zr}_2\text{O}_7$ and $\text{Tb}_2\text{Hf}_2\text{O}_7$ provide a wealth of similarities on their low-temperature properties as we confirm below.

The value of zv lies between 4 and 12 supporting the spin-glass character of $\text{Tb}_2\text{Zr}_2\text{O}_7$. Our results also reveal evidence for a spin freezing below 2.5 K which is support by the real χ'_{ac} and the imaginary χ''_{ac} susceptibilities measured for frequencies between 15 Hz and 10 kHz. The $\delta T' \approx 0.06$ is typical to values of spin glasses. The large number of non-magnetic defects or of disorder in the lattice leads to an spin glass at higher temperature than $\text{Tb}_2\text{Hf}_2\text{O}_7$. Without features of long-range magnetic order in the specific heat of $\text{Tb}_2\text{Zr}_2\text{O}_7$, it could be also a spin-liquid candidate. This an interesting result since the presence of these glassy features together with the intrinsic disorder of the lattice can host localized fractional excitations [124].

By looking at the estimation for the nuclear component C_{N1} could have another interpretation (dashed line of figure 7.8) in which it is modeled as considering a model of reduced moments and associated to quantum spin fluctuations affecting the nuclear spins [121, 122]. This is also revealed by the large values of susceptibility χ'_{ac} at the lowest temperature measured. These previous results suggesting a frozen moment together with

fluctuations characterized the theory proposed for topological spin glasses [124].

The two-level analysis of the maxima in electronic specific heat (figure 7.9(a)) reveals that the first crystal electric field splitting of $\text{Tb}_2\text{Zr}_2\text{O}_7$ is around $\Delta\varepsilon = 10$ K very similar to the energy scale of the broad maxima, and then its origin is the thermal population of CEF levels. The obtained gap is close to the splitting of 17 K in $\text{Tb}_2\text{Ti}_2\text{O}_7$ suggesting similar energy distribution of levels. The broad anomaly around 5 K for $\text{Tb}_2\text{Zr}_2\text{O}_7$ with its reduce amplitude shares some resemblance to the $\text{Tb}_2\text{Ti}_2\text{O}_7$ reported in [21] however this broad feature is exhibited in lower temperatures around 2 K and another in high temperature around 50 K for $\text{Tb}_2\text{Hf}_2\text{O}_7$.

We found that the average factor $g = 2.3$ is close to the values of the g factors reported for XY pyrochlores: $\text{Er}_2\text{Ti}_2\text{O}_7$ ($g_{\parallel} = 1.8$) and $\text{Yb}_2\text{Ti}_2\text{O}_7$ ($g_{\parallel} = 2.04$) [23] known for having a strong planar CEF anisotropy. Our g result for $\text{Tb}_2\text{Zr}_2\text{O}_7$ is much smaller if compared to the factor along the trigonal Ising axis $g_{\parallel} = 9.6$ for $\text{Tb}_2\text{Ti}_2\text{O}_7$. In addition, as reported by Anand *et al.*, fittings to the magnetic diffuse neutron scattering of $\text{Tb}_2\text{Hf}_2\text{O}_7$ rule out Tb^{3+} spins with Ising anisotropy but a quality fit was obtained by considering planar anisotropy [118]. These observations indicate that a potential first model to fit diffuse neutron scattering data in $\text{Tb}_2\text{Zr}_2\text{O}_7$ could be spins with an easy-planar anisotropy with antiferromagnetic correlations. If this correlations extend over many tetrahedra, we could be possible entering to a spin configuration in which phase competitions are present as observed in XY pyrochlores [29]. This picture of the ground state for $\text{Tb}_2\text{Zr}_2\text{O}_7$ is support by the presence of a broad specific heat anomaly together with no magnetic ordering in lower temperatures as reported similarly for XY pyrochlores by Hallas *et al.* [29].

Conclusion

The series of compounds of $\text{Er}_2\text{Ti}_{2-x}\text{Sn}_x\text{O}_7$ for $x = 0 - 2$ were successfully synthesized by using the solid-state reaction method. We have also used low-temperature annealing to prepare disordered fluorites of $\text{Dy}_2\text{Zr}_2\text{O}_7$, $\text{Ho}_2\text{Zr}_2\text{O}_7$ and $\text{Tb}_2\text{Zr}_2\text{O}_7$. The analysis of the structure by x-ray and neutron powder diffraction revealed non-stoichiometries and equal distribution of the rare-earth ions and of Zr on the two interpenetrating sublattices of corner-sharing tetrahedra.

The $\text{Er}_2\text{Ti}_{2-x}\text{Sn}_x\text{O}_7$ series present a change of the XY anisotropy of its magnetic ground state, which starts to develop around the composition $x = 1.5$. For $1.5 < x < 2$, we found decreasing values of the magnetic moments in XY; μ_{xy} , while a increasing of the moment perpendicular to this plane; μ_z consistent with the ground state in $\text{Er}_2\text{Sn}_2\text{O}_7$. In-field experiments show the absence of long-range features around 1.5 T. This result obtained from a specific heat analysis is in agreement with neutron experiment results reported in the literature [13, 14].

In this work it is been shown that the fluorite compounds $\text{Dy}_2\text{Zr}_2\text{O}_7$ and $\text{Ho}_2\text{Zr}_2\text{O}_7$, with its disordered lattice, but similar magnetic moment size, near-neighbour distance and short-magnetic correlations do not develop the spin-ice state. Both are suspect to be spin-liquid candidates in which the presence of a different glassy state is also possible. Different from the classical spin ices, ac susceptibility and specific heat revealed a significant spin dynamics and the absence of residual entropy. Neutron diffraction and specific heat in $\text{Dy}_2\text{Zr}_2\text{O}_7$ confirm the presence of short-range spin-spin correlations below 2 K, and no long-range order down to 40 mK. The correlations found are antiferromagnetic and extend over next-nearest neighbours only with a length around 6.6 Å.

Terbium pyrochlore oxides $\text{Tb}_2\text{Ti}_2\text{O}_7$ and $\text{Tb}_2\text{Hf}_2\text{O}_7$ have both shown spin glass character and no long-range magnetic order down to 100 mK [118]. We have shown in $\text{Tb}_2\text{Zr}_2\text{O}_7$ from its time correlations and parameters obtained from spin-glass models to ac susceptibility a glass transition around 2.5 K. Specific heat revealed no long-range order and the presence of spin fluctuations in the mK scale. In-field specific heat in $\text{Ho}_2\text{Zr}_2\text{O}_7$ and $\text{Tb}_2\text{Zr}_2\text{O}_7$ suggest roughly a planar anisotropy of the magnetic ion different from the strong Ising anisotropy found in $\text{Ho}_2\text{Ti}_2\text{O}_7$ and $\text{Tb}_2\text{Ti}_2\text{O}_7$.

8.1 Future work

Future work concerns to study CEF excitations and the environment of the rare earth in the disordered fluorites by means of inelastic neutron scattering. Experimental studies on the CEF levels of $\text{Ho}_2\text{Zr}_2\text{O}_7$ were performed at ISIS Neutron & Muon Source facilities (Rutherford Appleton Laboratory/Oxfordshire, U.K.) but the analysed data was not on time for this manuscript. Also, to prepare crystal samples of the disordered fluorites and to study them by using high energy x-ray experiments to improve our structural analysis about the local surroundings of the rare-earth ions. To study the relaxation of the magnetization and ac susceptibility observed in spin glasses for $\text{Tb}_2\text{Zr}_2\text{O}_7$.

Bibliography

- [1] C. Lacroix, P. Mendels, and F. Mila. Introduction to frustrated magnetism. Springer Series in Solid–State Sciences, Heidelberg (2011).
- [2] J. S. Gardner *et al.* Reviews of Modern Physics **82**, 53 (2010).
- [3] P. Schiffer and A. P. Ramirez. Comments on Condensed Matter Physics **18**, 21 (1996).
- [4] A. Kluber *et al.* Proceedings of the National Academy of Sciences of the United States of America, **115**, 9234 (2018).
- [5] J. S. Gardner *et al.* Physical Review Letters **82**, 1012 (1999).
- [6] J. S. Gardner *et al.* Physical Review B **68**, 180401(R) (2003).
- [7] A. P. Ramirez *et al.* Nature **399**, 333 (1999).
- [8] B. C. den Hertog and M. J. P. Gingras. Physical Review Letters **84**, 3430 (2000).
- [9] L. Savary *et al.* Physical Review Letters **109**, 167201 (2012).
- [10] J. D. M. Champion *et al.* *Physical Review B* **64**, 140407 (2001).
- [11] J. R. Stewart *et al.* *Journal of Physics: Condensed Matter* **16**, L321 (2004).
- [12] J. A. M. Paddison *et al.* arXiv:1506.05045. 1 (2015).
- [13] M. Shirai *et al.* Physical Review B **96**, 180411(R) (2017).
- [14] S. Petit *et al.* Physical Review Letters **119**, 187202 (2017).
- [15] S. E. Palmer and J. T. Chalker. Physical Review B **62**, 14488 (2000).

- [16] K. Kimura *et al.* Nature Communications **4**, 1934 (2013).
- [17] S. Petit *et al.* Nature Physics **12**, 746 (2016).
- [18] R. Sibille *et al.* Nature Communications **8**, 892 (2017).
- [19] V. K. Anand *et al.* Physical Review B **94**, 144415 (2016).
- [20] A. Poole *et al.* Journal of Physics: Condensed Matter **19**, 452201 (2007).
- [21] M. J. P. Gingras *et al.* Physical Review B **62**, 6496 (2000).
- [22] S. Blundell. Magnetism in condensed matter. Oxford University Press, New York (2001).
- [23] A. Bertin *et al.* Journal of Physics: Condensed Matter **24**, 256003 (2012).
- [24] N. W. Ashcroft and N. D. Mermin. Solid state physics. Holt, Rinehart and Winston, New York (1976).
- [25] O. V. Lounasmaa, A. J. Freeman and R. B. Frankel. Nuclear specific heats in metals and alloys. Hyperfine Interactions. New York and London, Academic Press, 467 (1967).
- [26] E. S. R. Gopal. Specific heats at low temperatures. The International Cryogenics Monograph Series. Springer US, first edition (1966).
- [27] S. Petit *et al.* European Physical Journal Web of Conferences **83**, 03012 (2015).
- [28] J. E. Greedan. Journal of Alloys and Compounds **408–412**, 444 (2006).
- [29] A. M. Hallas *et al.* Annual Review of Condensed Matter Physics, 1–21 (2017).
- [30] G. C. Lau *et al.* Nature physics **2**, 249 (2006).
- [31] P. Dalmas de Réotier *et al.* Physical Review B **86**, 104424 (2012).
- [32] J. Gaudet *et al.* Physical Review B **94**, 060407(R) (2016).
- [33] E. C. Andrade *et al.* Physical Review Letters **120**, 097204 (2018).
- [34] D. J. Flood. Journal of Applied Physics **45**, 4041 (1974).

- [35] L. Pauling. *Journal of the American Chemical Society* **57**, 2680 (1935).
- [36] S. T. Bramwell *et al.* *Journal of Physics: Condensed Matter* **10**, 215 (1998).
- [37] L. D. C. Jaubert and P. C. W. Holdsworth. *Journal of Physics: Condensed Matter* **23**, 164222 (2011).
- [38] K. Matsuhira *et al.* *Journal of Physics: Condensed Matter* **13**, L737 (2001).
- [39] J. Snyder *et al.* *Nature* **413**, 48 (2001).
- [40] L. Balents. *Nature* **464**, 199 (2010).
- [41] P.W. Anderson. *Materials Research Bulletin* **8**, 153 (1973).
- [42] J. S. Gardner *et al.* *Physical Review B* **64**, 224416 (2001).
- [43] T. Fennell *et al.* *Physical Review B* **70**, 134408 (2004).
- [44] M. J. Harris *et al.* *Physical Review Letters* **79**, 2554 (1997).
- [45] S. T. Bramwell *et al.* *Physical Review Letters* **87**, 047205 (2001).
- [46] H. R. Molavian *et al.* *Physical Review Letters* **98**, 157204 (2007).
- [47] T. Fennell *et al.* *Physical Review Letters* **112**, 017203 (2014).
- [48] I. Mirebeau *et al.* *Nature* **420**, 54 (2002).
- [49] J. P. C. Ruff *et al.* *Physical Review B* **82**, 100401(R) (2010).
- [50] G. Luo *et al.* *Physics Letters A* **291**, 306 (2001).
- [51] B. G. Ueland *et al.* *Physical Review Letters* **96**, 027216 (2006).
- [52] H. Takatsu *et al.* *Journal of Physics: Condensed Matter* **24**, 052201 (2012).
- [53] A. Yaouanc *et al.* *Physical Review B* **84**, 184403 (2011).
- [54] N. Hamaguchi *et al.* *Physical Review B* **69**, 132413 (2004).
- [55] J. A. Mydosh. *Spin Glasses: An experimental Introduction*. Taylor & Francis, London (1993).

- [56] J. S. Gardner *et al.* Physical Review Letters **83**, 211 (1999).
- [57] P. Bonville *et al.* Journal of Physics: Condensed Matter **15**, 7777 (2003).
- [58] P. M. Sarte *et al.* Journal of Physics: Condensed Matter **23**, 382201 (2011).
- [59] G. Balakrishnan *et al.* Journal of Physics: Condensed Matter **10**, L723 (1998).
- [60] Z. S. Chen *et al.* Bulletin of Materials Science **34**, **3**, 429 (2011).
- [61] A. Garbout *et al.* Journal of Alloys and Compounds **469**, 229 (2009).
- [62] A. Garbout *et al.* Journal of Alloys and Compounds **425**, 88 (2006).
- [63] J. G. A. Ramón, M. Sc. dissertation, Universidade de São Paulo, Brazil, 2015.
- [64] S. A. Speakman. Training to Become an Independent User of the X-Ray SEF at the Center for Materials Science and Engineering at MIT. Massachusetts Institute of Technology.
- [65] R. Guinebretière. X-ray diffraction by polycrystalline materials. ISTE Publishing Company, London (2007).
- [66] G. L. Squires. Introduction to the theory of thermal neutron scattering. Cambridge University Press, Cambridge (2012)
- [67] R. Stewart. Neutron Scattering: Neutron interactions and sources. ISIS Neutron Training Course, Rutherford Appleton Laboratory (2018).
- [68] K. Liss *et al.* Physica B **385–386**, 1010 (2006).
- [69] A. J. Studer *et al.* Physica B **385–386**, 1013 (2006).
- [70] A. N. Radhakrishnan *et al.* Dalton Transactions **40**, 3839 (2011).
- [71] H. M. Rietveld. Journal of Applied Crystallography **2**, 65 (1969).
- [72] J. Rodríguez–Carvajal. Physica B **192**, 55 (1993).
- [73] AC Magnetic Susceptibility Measurement Kit, Operating Manual and Technical Information. Cambridge Cryogenics (2017).

- [74] mK Magnetic Refrigerator, System Information. Cambridge Cryogenics (2017).
- [75] L. M. B. Santos. Manual of the home-made ac susceptometer at LESBT. Physics Institute, Universidade de São Paulo (2018).
- [76] M. Nikolo. American Journal of Physics **63**, **57**, 57 (1995).
- [77] Magnetic Property Measurement System, SQUID VSM User's Manual. Quantum Design, 17th edition, San Diego (2009).
- [78] J. Bardeen *et al.* Physical Review **108**, 1175 (1957).
- [79] B. D. Josephson. Physics Letters **1**, 251 (1962).
- [80] M. Tinkham. Introduction to superconductivity. McGraw-Hill, Inc., 2nd edition (1996).
- [81] Physical Property Measurement System, Heat Capacity Option User's Manual. Quantum Design, 17th edition, San Diego (2010).
- [82] F. Pobell. Matter and Methods at Low Temperatures. Springer-Verlag, Berlin (2007).
- [83] Physical Property Measurement System, Dilution Refrigerator User's Manual. Quantum Design, 6th edition, San Diego (2013).
- [84] Physical Property Measurement System, AC Measurement System Option User's Manual. Quantum Design, 4th edition, San Diego (2003).
- [85] R. K. Harris *et al.* Pure and Applied Chemistry **73**, 1795 (2001).
- [86] Da-qian Liao *et al.* Physical Review B **83**, 064403 (2011).
- [87] Y. Chapuis *et al.* Physical Review B **82**, 100402 (2010).
- [88] V. Hardy *et al.* Physical Review B **68**, 014424 (2003).
- [89] D. H. Ryan *et al.* Physical Review B **68** 014413 (2003).
- [90] M. Shirai. Experimental investigations of frustrated antiferromagnets. Ph.D. thesis. University College London (2007).
- [91] S. S. Sosin *et al.* Physical Review B **82**, 094428 (2010).

- [92] J. P. C. Ruff *et al.* Physical Review Letters **101**, 147205 (2008).
- [93] M. C. Hatnean *et al.* Crystals **6**, 79 (2016).
- [94] R. Clements *et al.* Journal of Solid State Chemistry **184**, 2108 (2011).
- [95] E. Reynolds *et al.* Inorganic Chemistry **52**, 8409 (2013).
- [96] H. Fukazawa *et al.* Physical Review B **65**, 054410 (2002).
- [97] J. Snyder *et al.* Physical Review B **69**, 064414 (2004).
- [98] G. Ehlers *et al.* Journal of Physics: Condensed Matter **15**, L9 (2003).
- [99] L. D. C. Jaubert and P. C. W. Holdsworth. Nature Physics **5**, 258 (2009).
- [100] A. C. Anderson *et al.* Physical Review **183**, **2**, 546 (1969).
- [101] D. Pomaranski *et al.* Nature Physics **9**, 353 (2013).
- [102] J. G. Rau and M. J. P. Gingras. Physical Review B **92**, 144417 (2015).
- [103] L. Pauling. Journal of the American Chemical Society **57**, 2680 (1935).
- [104] S. T. Bramwell *et al.* Nature (London) **461**, 956 (2009).
- [105] G. Ehlers *et al.* Physical Review B **81**, 224405 (2010).
- [106] J. G. A. Ramon *et al.* Physical Review B **99**, 214442 (2019).
- [107] S. Gao *et al.* Physical Review Letters **120**, 137201 (2018).
- [108] G. C. Lau *et al.* Physical Review B **72**, 054411 (2005).
- [109] M. A. Subramanian *et al.* Progress in Solid State Chemistry **15**, 55 (1983).
- [110] S. T. Bramwell *et al.* Journal of Physics: Condensed Matter **12**, 483 (2000).
- [111] K. Matsuhira *et al.* Journal of Physics: Condensed Matter **12**, L649 (2000).
- [112] J. A. Quilliam *et al.* Physical Review B **83**, 094424 (2011).
- [113] O. V. Lounasmaa. Physical Review **128**, **3**, 1136 (1962).
- [114] B. Bleaney. Journal of Applied Physics **34**, **4**, 1024 (1963).

- [115] J. D. M. Champion *et al.* Physical Review B **68**, 020401(R) (2003).
- [116] A. J. Princep *et al.* Physical Review B **91**, 224430 (2015).
- [117] E. Lhotel *et al.* Physical Review B **86**, 020410(R) (2012).
- [118] V. K. Anand *et al.* Physical Review B **97**, 094402 (2018).
- [119] O. V. Lounasmaa and P. R. Roach. Physical Review **128**, **2**, 622 (1962).
- [120] Y. Tokiwa *et al.* Nature Materials **13**, 356 (2014).
- [121] P. Bonville. Journal of Physics: Conference Series **217**, 012119 (2010).
- [122] E. Bertin *et al.* The European Physical Journal B **27**, 347 (2002).
- [123] C. A. Catanese *et al.* Physical Review B **8**, 4223 (1973).
- [124] A. Sen and R. Moessner. Physical Review Letters **114**, 247207 (2015).

Nuclear specific heat

The hyperfine Hamiltonian has two contributions arising from different interactions. The first one is due to the coupling between nuclear magnetic moments and the effective electronic magnetic field (Zeeman term). The second one results from the electric field gradient $\nabla V(\mathbf{r})$ originated by the electrostatic potential $V(\mathbf{r})$ at the nucleus that interact with the quadrupole moment of the nucleus. The nuclear Hamiltonian is given by

$$\mathcal{H} = -\hbar\gamma \mathbf{I} \cdot \mathbf{B} + P \left[\mathbf{I}_z^2 - \frac{1}{3}I(I+1) \right], \quad (\text{A.1})$$

where \hbar is the Planck constant, γ is the gyromagnetic ratio of the isotope of a rare-earth R^{3+} , \mathbf{I} is the nuclear spin operator, \mathbf{B} is the effective magnetic field due to the R^{3+} magnetic moments, and P depends of the quadrupole moment Q of the rare-earth element.

In Chapter 2 we use the Hamiltonian (A.1) for computing the nuclear energy levels since the planar anisotropy nature of the Er^{3+} . Follow the programs employed to fit the low-temperature specific heat of the $\text{Er}_2\text{Ti}_{2-x}\text{Sn}_x\text{O}_7$ series to the sum of the nuclear and electronic contributions:

```

import math
import matplotlib.pyplot as plt
import numpy
def Nuclear_SpecificHeat(Bhyp,BhypZ,RT,r):
    global T0,TF,h
    Ip = numpy.matrix([[0, math.sqrt(7),0,0,0,0,0,0],
                       [0, 0,math.sqrt(12),0,0,0,0,0],
                       [0, 0,0,math.sqrt(15),0,0,0,0],
                       [0,0,0,0,4,0,0,0],
                       [0,0,0,0,0,math.sqrt(15),0,0],
                       [0,0,0,0,0,0,math.sqrt(12),0],
                       [0,0,0,0,0,0,0,math.sqrt(7)],
                       [0,0,0,0,0,0,0,0]])
    In = Ip.getT()
    S = 7/2          #Nuclear spin
    n = int(2*S+1) #Nuclear spin degeneracy
    Ix = (Ip + In)/2
    Iy = (Ip - In)/(2*1j)
    Iz = numpy.zeros((n, n))
    for k in range(0,n):
        for i in range(0,n):
            if i==k:
                Iz[i,k] = (7-2*i)/2
            else:
                Iz[i,k] = 0
    p1 = 0.00163 #K
    k1 = 0.00856 #K
    c1 = Bhyp*5.894*10**(-5) #K
    c2 = BhypZ*5.894*10**(-5) #K
    Id = numpy.matrix(numpy.identity(n))
    H = p1*Iz**2 - c1*(Ix+Iy)-c2*Iz-k1*Id
    H_EV1 = numpy.linalg.eigvals(H) #Nuclear energy levels

def Z_T1(H_EV1, T):
    global Aux
    Z = 0
    Aux = numpy.zeros(n)
    for i in range(0,n):
        Aux[i] = H_EV1[i].real
    for i in range(0,n):
        Z = Z + math.exp(-1*(Aux[i])/T) #Partition function for a single temperature
    return Z
T = T0 = RT[0]
TF = RT[1]
h = (TF - T0)/r
ZT1 = numpy.zeros((r+1, 2)) #Initial matrix of partition function
LogZT1 = numpy.zeros((r+1, 2))#Initial matrix of Log of partition function
for i in range (0,r+1):
    ZT1[i,0] = T
    ZT1[i,1] = Z_T1(H_EV1, T)
    LogZT1[i,0] = T
    LogZT1[i,1] = math.log(ZT1[i,1])
    T = T + h
T = T0
UT1 = numpy.zeros((r, 2)) #Initial matrix of nuclear energy of the system
for i in range (0,r):
    UT1[i,0] = T
    UT1[i,1] = (T**2)*(LogZT1[i+1,1]-LogZT1[i,1])/h
    T = T + h
T = T0
Cn = numpy.zeros((r-1, 2))#Initial matrix of specific Heat
for i in range (0,r-1):
    Cn[i,0] = T
    Cn[i,1] = (UT1[i+1,1]-UT1[i,1])/h
    T = T + h
print("Nuclear energy levels (K):", Aux)
return Cn

```

Figure A.1: Program implemented in Python for the account of the nuclear specific heat of the $\text{Er}_2\text{Ti}_{2-x}\text{Sn}_x\text{O}_7$ series.

```

def Electronic_SpecificHeat(vsw,gap,RT,r):
    lc = 10.0727 #Lattice constant of the unit cell- Angstrom
    A = 1534.5*(lc**3/vsw**3) #Factor that multiplies T**3 of the magnon contribution gap = 0
    T = T0 = RT[0]
    TF = RT[1]
    h = (TF - T0)/r
    def Int(Temperature):
        a = 0 #lower bound of integral
        b = 250 #upper bound - 'infinite'
        rl = 10000 #2000
        hl = (b - a)/rl
        I = 0
        x = a
        for i in range (0,rl):
            f1 = (x**2)*(x**2 + (gap/Temperature)**2)/(math.sinh(math.sqrt(x**2 + (gap/Temperature)**2)/2))**2
            x = x + hl
            f2 = (x**2)*(x**2 + (gap/Temperature)**2)/(math.sinh(math.sqrt(x**2 + (gap/Temperature)**2)/2))**2
            I = I + hl*(f1+f2)/2
        return I*15/(16*math.pi**4)
    Csw = numpy.zeros((r-1, 2))#Initial matrix of magnon specific Heat least the final point of temperature
    for i in range (0,r-1):
        Csw[i,0] = T
        Csw[i,1] = A*Int(Csw[i,0])*(T**3) #Magnon gap = 0 and nuclear specific heat
        T = T + h
    return Csw

```

Figure A.2: Program implemented in Python for the account of the electronic specific heat of the $\text{Er}_2\text{Ti}_{2-x}\text{Sn}_x\text{O}_7$ series.

The Hamiltonian in case of axial symmetry as in the cases of metallic rare-earth elements is

$$\mathcal{H} = aI_z + P \left[I_z^2 - \frac{1}{3}I(I+1) \right], \quad (\text{A.2})$$

where $I_z = -I, -I+1, \dots, I-1, I$ are the values of the projections of the nuclear spin I , a is the magnetic hyperfine constant and P is the electric quadrupole coupling constant. In Chapter 5 and 6, we use the Hamiltonian (A.2) since we approximate the nuclear specific heat in $\text{Dy}_2\text{Zr}_2\text{O}_7$ and $\text{Ho}_2\text{Zr}_2\text{O}_7$ as the nuclear specific heat of metallic Dy and Ho, respectively. In Chapter 7, we account spin electronic fluctuations in the nuclear computed specific heat C_N of $\text{Tb}_2\text{Zr}_2\text{O}_7$ by multiplying by a factor f . This factor is introduced in the Zeeman contribution as $f \times aI_z$. The program employed is detailed in figure A.3.


```

(*****NUCLEAR SPECIFIC HEAT in metallic Tb*****)
k = 1.38065 * 10-23; (*JK-1*) (*Boltzman constant*)
Nv = 6.022 * 1023; (*mol-1*) (*Avogadro constant*)
R = 8.314; (*JK-1*mol-1 units*) (*Gas constant*)
S = 3/2; (*Nuclear Spin I of Tb*)
A = 0.6 * 0.15 (*Hyperfine constant = 0.15 in K units*) (*f=0.6 is the Reduction factor*)
P = 0.021 (*Quadrupole constant in K units*)

H[i_] := A * i + P * (i2 - S * (S + 1) / 3) (*Nuclear Hamiltonian*);

z[T_] := Sum[e-(A*i+P*(i2-S*(S+1)/3))/T, {i, -S, S}] (*Partition Function*);

w[T_] := Nv * (1/z[T]) * (Sum[(A * i + P * (i2 - S * (S + 1) / 3)) * e-(A*i+P*(i2-S*(S+1)/3))/T, {i, -S, S}]) (*Energy of the System of Nv nuclei of Tb*)

c[T_] := k * D[w[T], T]; (*Total Nuclear Specific Heat*(J/(K.mol Tb))**)

Plot[Evaluate[c[T]], {T, 0.015, 10}, PlotRange -> {{0, 2.5}, {0, 6}}, PlotStyle -> {Green}, PlotTheme -> "Scientific"]

```

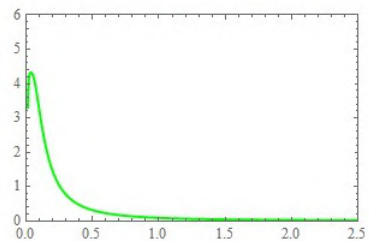


Figure A.3: Program implemented in Wolfram Mathematica 12.0 for the account of the nuclear specific heat of the disordered fluorites. As an example is shown the nuclear specific heat of metallic Tb used in the analysis of $\text{Tb}_2\text{Zr}_2\text{O}_7$.